

Cite this: *Phys. Chem. Chem. Phys.*, 2011, **13**, 9083–9118

[www.rsc.org/pccp](http://www.rsc.org/pccp)

## PERSPECTIVE

# Characterization of nanostructured hybrid and organic solar cells by impedance spectroscopy<sup>†</sup>

Francisco Fabregat-Santiago, Germà Garcia-Belmonte, Iván Mora-Seró and Juan Bisquert\*

Received 23rd October 2010, Accepted 2nd March 2011

DOI: 10.1039/c0cp02249g

We review the application of impedance spectroscopy in dye-sensitized solar cells, quantum dot-sensitized solar cells and organic bulk heterojunction solar cells. We emphasize the interpretation of the impedance parameters for determining the internal features of the device, concerning the carrier distribution, materials properties such as the density of states and/or doping of the semiconductors, and the match of energy levels for photoinduced charge generation and separation. Another central task is the determination of recombination mechanisms from the measured resistances, and the factors governing the device performance by combined analysis of resistances as a function of voltage and current–voltage curves.

## 1. Introduction

With the increasing demands for clean energy, solar cells have become a foremost device for energy production. The use of solar cells to convert sunlight energy to electricity is becoming rapidly extended but the cost of the existing technologies is far too high to compete on a large scale with the traditional carbon

Photovoltaic and Optoelectronic Devices Group,  
Departament de Física, Universitat Jaume I, 12071 Castelló, Spain.  
E-mail: bisquert@fca.uji.es  
† Electronic supplementary information (ESI) available. See DOI:  
10.1039/c0cp02249g

dioxide-producing energy sources. Therefore, the research to improve the efficiency of existing solar cells and to develop new cost-effective technologies has become a major focus of scientific and industrial activities. Dye-sensitized solar cells (DSCs)<sup>1–3</sup> and organic bulk heterojunction (BHJ)<sup>4,5</sup> solar cells have evolved to viable devices, with efficiencies above 12% and 8%, respectively, and increasing stability on outdoor conditions.<sup>6–8</sup> Nanostructured solar cells based on inorganic absorber materials with a quantum confinement regime, usually termed quantum dot sensitized solar cells (QDSCs), have also experienced a notable progress.<sup>9–14</sup> Since DSC and BHJ devices of sufficient quality are now widely available, techniques that



**Francisco Fabregat-Santiago**  
*(Bsc in Physics 1995, PhD in 2001) is Associate Professor in the Department of Physics at the University Jaume I in Spain and an active member of the Photovoltaic and Optoelectronic Devices Group. He is an expert in electro-optical characterization of devices and particularly known by his works in the use of impedance spectroscopy to study the electrical properties of devices and films including ZnO and TiO<sub>2</sub> nanostructured films, dye sensitized solar cells, electrochromic materials and liquid and solid state hole conductors.*



**Germà Garcia-Belmonte**

*Germà Garcia-Belmonte received his PhD degree at Universidad Nacional de Educación a Distancia, in 1996. He worked from 1988 at CIEMAT, Madrid, on experimental as well as theoretical research in the area of digital processing of nuclear signal. He joined the Universitat Jaume I, Castelló, in 1992 and currently works as Professor of Applied Physics (2010) at the Department of Physics (Photovoltaic and Optoelectronic Devices Group). Recently he follows researches in various topics within the field of Organic Electronics and photovoltaics as electronic mechanisms in organic light-emitting diodes, organic photovoltaics, and plastic and thin-film solar cells. Device physics using impedance spectroscopy (including modeling and measuring) is his main subject.*

determine the device properties, to assist the improvement of the performance based on rational design of materials and control of interfaces, are required. Impedance Spectroscopy (IS) consists in the frequency analysis of ac behaviour and is widely applied in a broad class of material systems and devices, including inorganic, organic and biological systems. IS has been applied very widely to investigate the properties of a variety of kinds of DSCs,<sup>15–22</sup> most recently with high performance dyes,<sup>23,24</sup> modified electrolytes,<sup>25</sup> solid hole conductors,<sup>26,27</sup> plastic or metal substrates,<sup>28,29</sup> and with Co and outer-sphere redox couples.<sup>30,31</sup> IS has been shown to be useful for the determination of diffusion lengths.<sup>32–34</sup> Recently IS has been also applied in QDSCs<sup>35–37</sup> and organic BHJ solar cells.<sup>38–42</sup> In this work we summarize the application of IS for the characterization of these photovoltaic systems, emphasizing the generality of the models and methods as well as the differences and particularities.

We first provide in Section 2 an overview of the basic properties of solar cells, what factors determine in general the performance of the device under sunlight, and in Section 3 we derive the models and methods that allow for a combined analysis of the steady state performance (current–voltage curves) and the internal mechanisms of the device by impedance spectroscopy. The methods take the general approach that has been successfully applied in DSC. From the general diffusion–recombination model<sup>15,21</sup> we focus on the determination of internal device features such as the disorder in the density of states (DOS) of the semiconductors, and the impact of recombination on the open-circuit voltage. Thereafter in Section 4 we review the main experimental features of IS measurements of DSC, and in Section 5 we discuss a broad variety of IS results for different configurations of DSC, emphasizing the interpretation of materials and device properties. Section 6 describes the recent advances in the understanding of QDSC by IS. Section 7 provides an overview of our current understanding of the device properties of organic BHJ solar cells, based on the general features of capacitance as a function of voltage that have been established in a variety of cases.



Iván Mora-Seró

*Iván Mora-Seró received his PhD at Universitat de València (Spain) on the crystal growth of semiconductors II–VI with narrow gap. He joined the Photovoltaic and Optoelectronic Devices Group at Universitat Jaume I (Spain) in 2002. Since then he has specialized in research on the characterization of the injection, transport, and recombination in sensitized electrodes using as absorbing materials both dye and especially semiconductor quantum dots.*

## 2. Solar cell characterization and the physical limits to the performance

There are strong connections between many features of the IS measurements of several kinds of solar cells, including DSC, BHJ and inorganic Si<sup>43</sup> and CdTe solar cells.<sup>44</sup> Therefore it is convenient to start at a very general standpoint, Fig. 1, from which to elaborate both the current–voltage curve, Fig. 2(a), and the IS parameters. The simple model of Fig. 1(b) contains the basic elements of the photovoltaic conversion process. The key point of the efficient solar-cell energy conversion is the combination of carrier generation by the light absorption and charge separation.<sup>45</sup> In the absorber material of Fig. 1(a)

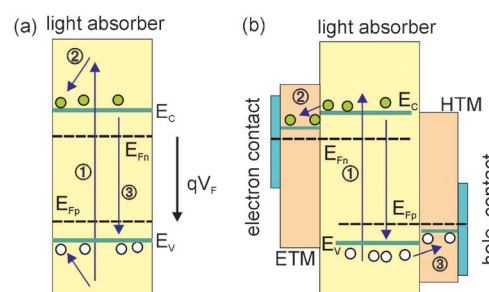


**Fig. 1** (a) Absorption of light in a semiconductor (1) produces electrons and hole carriers that rapidly relax (2) to the lowest lying energy levels of the conduction band ( $E_C$ ) and highest levels of the valence band ( $E_V$ ). The excess photogenerated carriers produce a splitting of the Fermi levels of electrons ( $E_{Fn}$ ) and holes ( $E_{Fp}$ ) that is marked as a “Fermi level voltage”  $V_F$ . Electrons decay to valence band levels by recombination with holes (3). (b) Scheme of a solar cell, formed by the absorber material supplemented by two selective contacts. These are formed by an electron transport material (ETM) that is transparent to electrons and rejects holes, and by a hole transport material (HTM) that accepts and transports the holes with no impedance, and blocks the electrons. Such arrangements allow the Fermi level in the metal contacts to equilibrate with the separate Fermi levels of electrons and holes, producing an external voltage, and to extract the carriers giving a photocurrent in the external circuit.



Juan Bisquert

*Juan Bisquert is professor of Applied Physics at Universitat Jaume I de Castelló and leads the Photovoltaic and Optoelectronic Devices Group ([www.elp.uji.es](http://www.elp.uji.es)) at the Physics Department. Recent research activity is focused on nanoscale devices for production of clean energies, in particular dye-sensitized solar cells, organic solar cells and quantum-dot sensitized solar cells. Bisquert is a specialist in theoretical modelling and interpretation of impedance spectroscopy techniques that have shown to be very useful to understand fundamental electronic phenomena and device properties in dye-sensitized solar cells, organic solar cells, nanowire structures, organic LEDs, and solid-state photovoltaic devices.*

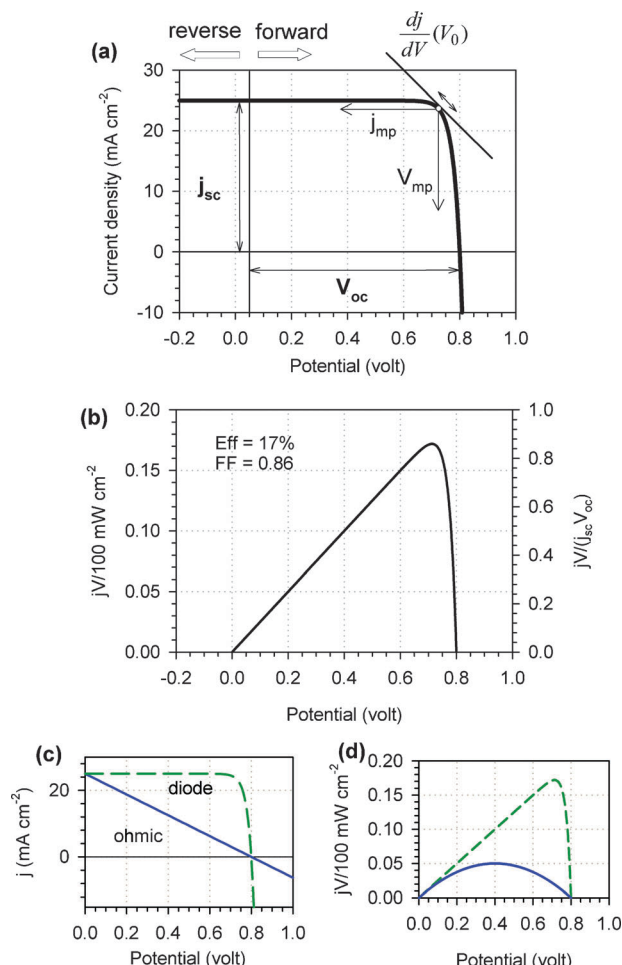


**Fig. 2** Theoretical calculation of the current–voltage curve (a) and power output (b) of a solar cell with  $j_{sc} = 25 \text{ mA cm}^{-2}$ ,  $V_{oc} = 0.8 \text{ V}$ , and diode factor  $m = 1$ . In (b) the left vertical axis is normalized to the incident power of 1 sun and gives the conversion efficiency, and the right axis normalization gives the fill factor. Comparison of the current–voltage curve (c) and power output (d) for two solar cells with the same  $j_{sc}$  and  $V_{oc}$ , but with different FF characteristics. The diode curve has FF 0.86 and conversion efficiency of 17% while the straight curve (“ohmic solar cell”) has an efficiency of less than 5%.

electrons are promoted from the valence band to the conduction band by light excitation. The solar cell is completed with selective contacts to electrons and holes, Fig. 1(b), which consist of n- and p-type materials, respectively, both in contact with the light absorber.

The characteristic spectrum of sunlight irradiating the Earth's surface is given by the ASTM Standard G159 and named Air Mass 1.5 (AM1.5). The so-called AM1.5G, the overall reference for solar-cell characterization (<http://rredc.nrel.gov/solar/spectra/>), shown in Fig. 3, cumulates an integrated power density of  $\phi_{E,\text{tot}}^{\text{AM1.5G}} = 1000 \text{ W m}^{-2}$  ( $100 \text{ mW cm}^{-2}$ ), and an integrated photon flux of  $\phi_{\text{ph},\text{tot}}^{\text{AM1.5G}} = 4.31 \times 10^{21} \text{ s}^{-1} \text{ m}^{-2}$  distributed over a large range of wavelengths (280–4000 nm). The photon flux emitted by a blackbody (BB) at temperature  $T$  is

$$\phi_{\text{ph}}^{\text{bb}}(E) = \frac{2\pi}{h^3 c^2} \frac{E^2}{e^{E/k_B T} - 1} \quad (1)$$

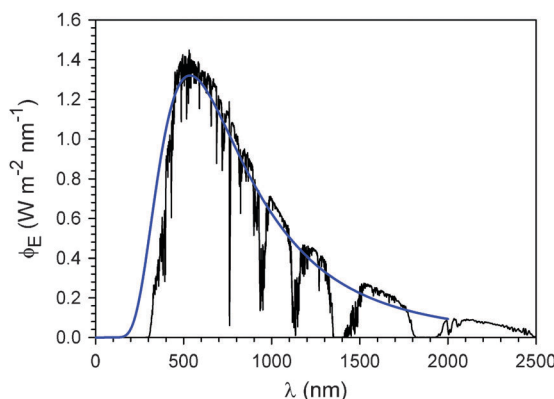


**Fig. 3** Air Mass 1.5 Global (AM1.5G) solar spectrum (energy as a function of wavelength) and the spectrum of a blackbody at temperature 5800 K with a dilution factor  $1.56 \times 10^{-5}$  (blue line).

Here  $E = h\nu$  is the photon energy,  $h$  is Planck's constant,  $c$  is the speed of light and  $k_B$  is Boltzmann's constant, and  $\phi_{\text{ph}}^{\text{bb}}$  is given in units  $\text{m}^{-2} \text{ s}^{-1} \text{ eV}^{-1}$ . The energy flux has the expression

$$\phi_E^{\text{bb}}(E) = E \phi_{\text{ph}}^{\text{bb}}(E) \quad (2)$$

The solar AM1.5G spectrum is approximately similar to a blackbody spectrum at temperature  $T = 5800 \text{ K}$  shown in Fig. 3 (a dilution factor  $F_S$  is included in eqn (1) to match the total power of the photon distribution). We use such a BB spectrum for a qualitative discussion of current generation in solar cells.

The generated electron–hole pairs produce an electrical current density,  $j$ , and voltage,  $V$ , and we have the electrical power output

$$P_{\text{el}} = jV \quad (3)$$

The power conversion efficiency (PCE) of the solar cell is given by the expression

$$\eta = \frac{jV}{\phi_{E,\text{tot}}} \quad (4)$$

According to eqn (4) an analysis of the efficiency requires to consider the current density of the solar cell as a function of voltage. This is the  $jV$  characteristic and is shown in Fig. 2. This characteristic determines the main aspects of the production of electrical power with a solar cell. We consider in turn the main features of  $jV$  characteristics.

## 2.1 The photocurrent

The first aspect is the photocurrent, which is basically the extraction of the photogenerated electrons and holes, and is quantified by the short-circuit current of the solar cell,  $j_{sc}$ . The primary limitations to the photocurrent are given by the absorption properties of the absorber. The absorber material can be an organic or inorganic semiconductor, or a dye molecule, and in general it is characterized by the absorptance  $a(E)$ . It is useful to assume as a reference case a semiconductor that absorbs all photons of energy larger than the semiconductor bandgap ( $a(E) = 1$  for  $E \geq E_g$ ), as indicated in Fig. 4. Once the photon is absorbed (process 1 in Fig. 1(a)), there is a rapid relaxation of the exciton, or separated electron

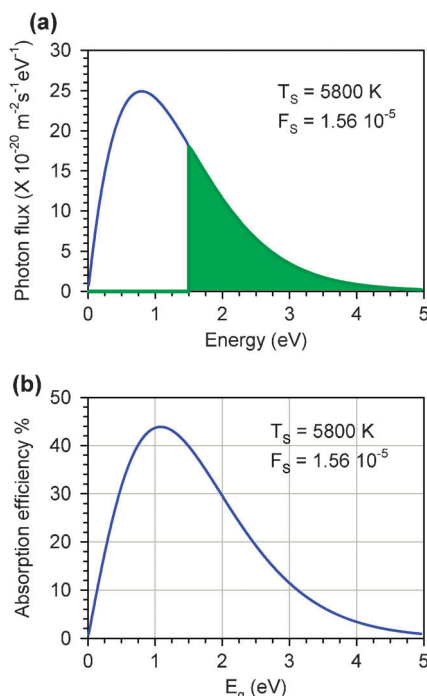


**Fig. 4** (a) Photon flux emitted by a blackbody at temperature 5800 K with a dilution factor  $F_s = 1.56 \times 10^{-5}$  (blue line). The shaded area indicates the photons absorbed by a semiconductor of bandgap  $E_g = 1.5 \text{ eV}$  and absorptance  $a = 1$ . (b) The “absorption efficiency” is a count of the photons absorbed above the bandgap energy  $E_g$ , each photon contributing an energy  $E_g$ . This energy is divided by the total energy flux of the BB radiation.

and hole carriers, to the lowest energy configuration which is  $E_g$  in this example (process 2 in Fig. 1(a)). Meanwhile, the photons with energy lower than  $E_g$  are not absorbed. Therefore, after the fast thermalization of photogenerated carriers in the absorber, the energy available is  $E_g$  for each photon absorbed. The loss of unabsorbed photons and reduction of energy of the absorbed ones are the main factors governing the efficiency of sunlight energy conversion into electricity with an absorbing material. The conversion efficiency of the absorber, from photons to thermalized electrons and holes, can be written as

$$\frac{E_g}{\phi_{E,\text{tot}}} \int_{E_g}^{\infty} \phi_{\text{ph}}(E) dE \quad (5)$$

This conversion efficiency, where no recombination is considered, is plotted in Fig. 4(b), which shows that more than 50% of the energy of BB radiation at  $T_S$  is lost even in the most favourable condition, which is an absorber of  $E_g = 1.1 \text{ eV}$ .<sup>46</sup> This value is almost the same as that of silicon (1.12 eV). We remark that eqn (5) is an efficiency of production of energy of carriers, not of electrical power, which is described below (and given in Fig. 5(b)).

The maximal current that can be obtained as a function of the bandgap of the absorber is given by

$$j_{\text{sc}}^{\max} = q \int_{E_g}^{\infty} \phi_{\text{ph}}(E) dE \quad (6)$$

where  $q$  is the positive elementary charge. The maximal current is shown in Fig. 5(a), both for the AM1.5G spectrum

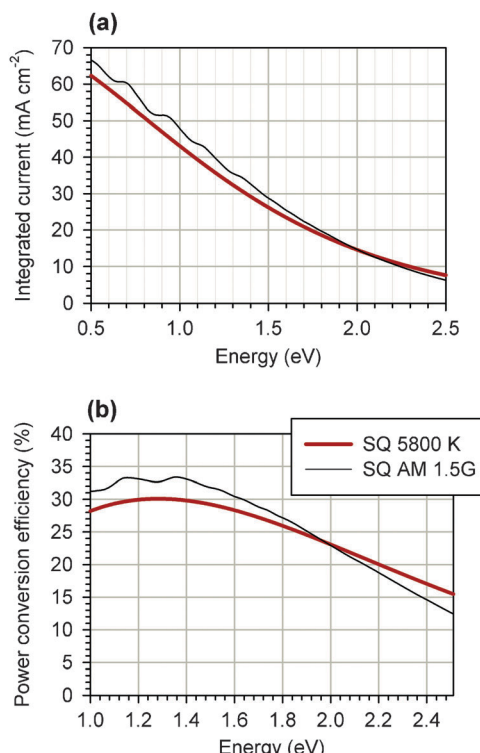


**Fig. 5** (a) Integrated current as a function of the bandgap energy of the absorber, for incident blackbody radiation at temperature  $T_S = 5800 \text{ K}$ , with total energy flux  $J_{E,\text{tot}} = 1000 \text{ W m}^{-2}$ . (b) The maximal photovoltaic efficiency of the absorber, assuming FF = 0.83. The thin lines are the current and Shockley–Queisser efficiency for actual AM1.5G solar irradiance.

and for the blackbody spectrum at  $T = 5800 \text{ K}$ . Note that the conversion efficiency of eqn (5) corresponds to

$$\frac{E_g j_{\text{sc}}^{\max}}{q \phi_{E,\text{tot}}} \quad (7)$$

Organic absorbers do not absorb equally at all wavelengths. For example chlorophyll *a* has very strong light absorption around 430 and 660 nm but relatively weak absorption bands in the visible region between these wavelengths. In practice the optical absorption properties of organic absorber material can depend on specific conditions and combination of materials of the solar cell. The photocurrent in a DSC is also affected by factors, such as the transparency and reflectance of the transparent electrode material, electron and hole transport layers, *etc.*,<sup>47</sup> and in general the optical properties of the device may be complex.<sup>48,49</sup> In this sense, it is very important to check that measured photocurrents have reasonable values, and are never above the value that is obtained by integrating the absorptance  $a(E)$  and AM1.5G spectrum.<sup>50</sup> A useful approach to make sure about the measured photocurrent is to measure the short-circuit current under monochromatic light as a function of the wavelength, divided by the theoretical current associated with the incident photon flux:

$$\eta_{\text{IPCE}}(\lambda) = \frac{j_{\text{sc}}(\lambda)}{q \phi_{\text{ph}}(\lambda) \Delta \lambda} \quad (8)$$

This magnitude is termed the external quantum efficiency (EQE) or incident-photon to current conversion efficiency

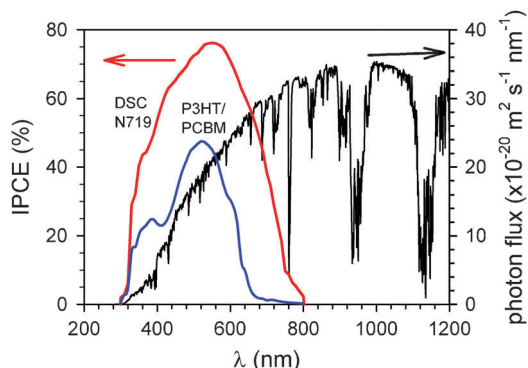


**Fig. 6** Air Mass 1.5 Global (AM1.5G) solar spectrum (photon flux as a function of wavelength) and the measured IPCE of a DSC with N719 dye and a BHJ solar cell formed by P3HT/PCBM.

(IPCE). Having determined the IPCE, the short-circuit photocurrent under a given light source should correspond to the value

$$j_{sc} = q \int_{\lambda_{min}}^{\lambda_{max}} \eta_{IPCE} \phi_{ph}^{\text{source}}(\lambda) d\lambda \quad (9)$$

where  $\lambda_{min}$  and  $\lambda_{max}$  are the wavelengths where the IPCE vanishes. An example of the measured IPCE of a DSC is shown in Fig. 6, in combination with the photon flux of the AM1.5G spectrum. The integration of eqn (9) gives in this case  $13 \text{ mA cm}^{-2}$ , in good agreement with the measured photocurrent. Currents up to  $19 \text{ mA cm}^{-2}$  can be obtained with N719 dye in a DSC. The current obtained with N749 (black) dye under standard conditions is close to  $22 \text{ mA cm}^{-2}$ .<sup>2</sup> For the P3HT:PCBM BHJ solar cell, we show the IPCE of a solar cell with  $7 \text{ mA cm}^{-2}$  photocurrent. High performance cells of this type give about  $11 \text{ mA cm}^{-2}$ .<sup>4</sup>

## 2.2 The photovoltage

The second important aspect is the maximal voltage produced by the solar cell, the open-circuit voltage  $V_{oc}$ . The excitation by light produces excess electrons and holes in the carrier bands, which causes the separation of the Fermi levels, of the two states in the absorber.<sup>51</sup> As shown in Fig. 1(a) we can define a Fermi level (or internal) voltage  $V_F$  as the difference of electrochemical potential of electrons ( $E_{Fn}$ ) and holes ( $E_{Fp}$ ) in the materials

$$V_F = (E_{Fn} - E_{Fp})/q \quad (10)$$

As mentioned above such an internal voltage is converted to an actual, useful voltage by selective contacts that transfer only one kind of carrier with minimal loss of free energy. The selective contacts have the function of taking the carriers, from a state of non-equilibrium Fermi level in the absorber to a material (normally a metal) in which the carrier is at the equilibrium Fermi level.<sup>52</sup> With ideal, reversible selective contacts, the quasi-Fermi level (which we hereafter denote simply as the Fermi level) is continuous at the interfaces between both n- and p-type materials and the absorber, as shown in Fig. 1(b).

It must be remarked that the picture in Fig. 1(b) is rather idealized. It gives a good measure of the fundamental

limitations of solar cells according to the Shockley–Queisser (SQ) model<sup>46</sup> which is entirely based on the properties of the absorber, but in practice the mechanisms of selectivity are varied and the electron and hole transport materials play important additional roles. For example, in crystalline silicon solar cells electrons and holes are selectively directed by strong fields in extremely localized regions at the edges of a thick absorber.<sup>43</sup> Electrons and holes are therefore separated, accumulated and transported in the absorber medium itself.

In contrast to this, the DSC is formed by 3 distinct materials. Energy levels for the material components of dye-sensitized solar cells and quantum dot-sensitized solar cells are shown in Fig. 7. Fig. 7(a) shows the energy levels of standard absorber dyes, the nanostructured  $\text{TiO}_2$  is the electron transport material, and a redox carrier<sup>53,54</sup> is the hole transport material. Fig. 7(b) is the energy picture for a set of inorganic quantum sized absorbers. In the DSC the photoexcited electrons are preferentially injected to  $\text{TiO}_2$  and the hole is thus transferred to the redox carrier, while the opposite pathway is kinetically and energetically forbidden for each carrier. The picture of Fig. 1(b) holds, because the available voltage is related to the separation of chemical potential of electrons and holes *in the dye*.<sup>55</sup> However, the dye contribution is small in terms of the volume of the materials and the residence time of the photo-excited carriers. Therefore, carrier accumulation occurs in the  $\text{TiO}_2$  nanostructure and in the redox carrier. This is directly probed by the chemical capacitance as described later and is furthermore very relevant for the recombination mechanism. In consequence the photovoltage is produced by the difference of the Fermi level of electrons in  $\text{TiO}_2$  and the redox level of the ionic carriers.

Returning to the benchmark SQ model, the fundamental limitation to the photovoltage is recombination. When the cell is at an open circuit, and irradiated at 1 sun, the photo-excitation is counteracted by recombination of electrons and holes and the corresponding split of the Fermi levels gives the open-circuit voltage,  $V_{oc}$ . Minimal recombination, which provides maximal possible  $V_{oc}$ , is determined by reciprocity of light emission with respect to light absorption, *i.e.* recombination is entirely associated with luminescence. It is therefore possible to elaborate a connection between maximal solar cell PCE and electroluminescence.<sup>56</sup> In a single semiconductor solar cell this model works well,<sup>57</sup> and in addition the Fermi levels cannot reach the band edges at 1 sun. In fact the SQ model is based on the assumption that minority carrier concentration does not exceed the majority carrier level.<sup>58</sup>

In the three materials DSC, and similarly in the organic BHJ, which is a two-material solar cell (although with an additional barrier layer for improved selectivity of contacts), the situation is different. Charge separation from the absorber requires a downhill driving force, and therefore, for the energetically favorable electron transfer, the lowest unoccupied molecular orbital (LUMO) level (or more correctly, the electron affinity) of the absorber material has to be about 0.3 eV higher than that of the conduction band (CB) of the electron transporter, *i.e.*  $\text{TiO}_2$  in a DSC, see Fig. 7(a), or the LUMO level of the fullerene in a BHJ.<sup>59</sup> In principle it is thus possible that  $E_{Fn}$  raises up to the CB edge, where a very large density of states (and effectively infinite chemical capacitance) prevents

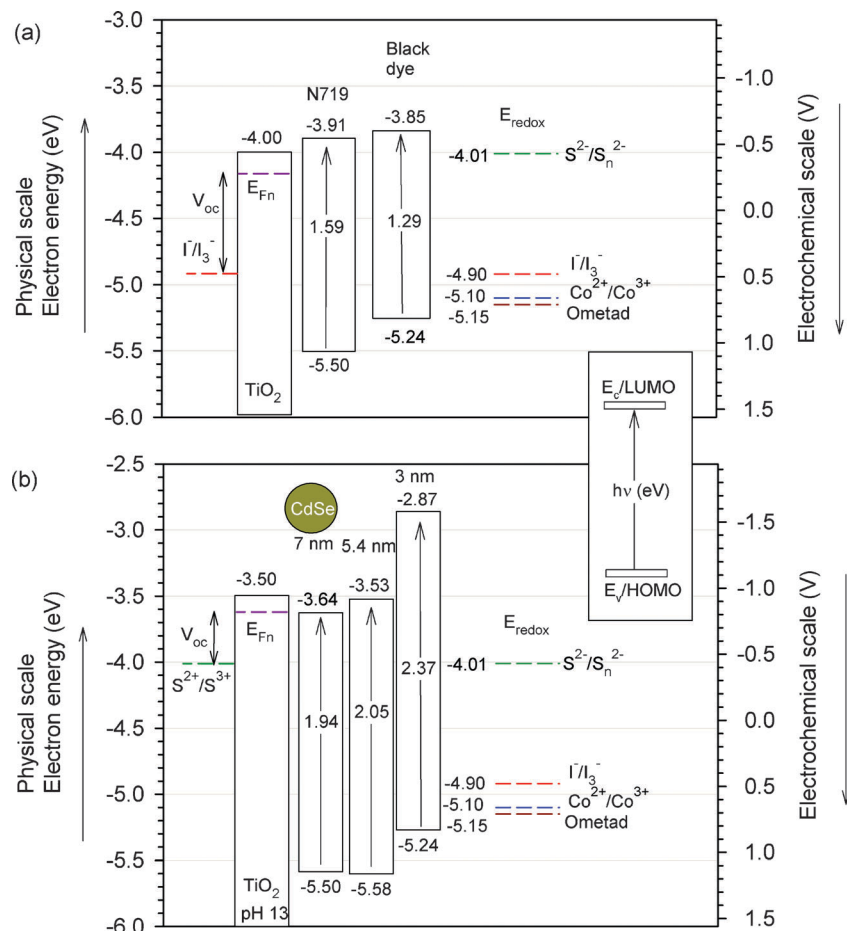


**Fig. 7** Schematic energy diagrams of the material components of dye solar cells. Standard energy levels are given in the energy scale, while the origin of the electrochemical scale is taken at -4.4 eV.  $E_{Fn}$  is the Fermi levels of electrons,  $E_{Fp}$  is the Fermi level of holes, and the difference relates to  $V_{oc}$  as indicated. Energy levels of  $TiO_2$  and dyes are dependent on the solution components, and dye levels may also depend on criteria for the onset of absorption. Energy levels of QDs from ref. 177.

the Fermi level from further raise. On the hole transporter side, a driving force for the regeneration of the oxidized dye is required as well. This is up to 500 mV with the best carrier, an  $I_3^-/I^-$  redox couple in organic solvent. The combination of the two energy steps for charge separation produces a limitation of the  $V_{oc}$  below recombination in the absorber. One can therefore modulate the DSC components to move up the CB of  $TiO_2$  to increase  $V_{oc}$ , but this has a price in the photocurrent, as it appears that less states in the  $TiO_2$  surface are able to accept electrons from the excited state of the dye.<sup>60</sup>

In addition, the  $V_{oc}$  is determined by the number of electrons stored in  $TiO_2$ , and this is in turn set by recombination of the thermalized electrons in the electron transport nanostructure. Such electrons transfer mainly to holes in the redox carrier, and this is another salient difference in the SQ approach. It means that recombination is disconnected from generation. In fact the luminescence of the DSC is a very small quantity. Nonetheless it is possible to reconstruct the IPCE from the electroluminescence by reciprocity.<sup>61</sup> Furthermore, in some metal-free dyes with long organic chains the recombination seems to take place *via* the dye molecule to a large extent.<sup>60</sup> However, there is still a general question as how much  $E_{Fn}$  approaches  $E_c$  in  $TiO_2$ , and our recent observations<sup>62</sup> indicate

that this is still controlled by recombination, not by the Fermi level entering the conduction band.

### 2.3 The fill factor (FF)

The third crucial aspect of the solar cell performance is the shape of the  $jV$  curve, which determines at which voltage we extract the electrons as electric current. As observed in Fig. 2, here is a tradeoff between current and voltage. At low voltage, extraction is easy, and the current is determined by the quantum yield (conversion of photons to electron carriers) of the absorber, as explained before. On the other hand, a high voltage produces a current that is opposed to the photocurrent, and eventually the power decreases. In general if we extract the electrons at high useful energy (voltage), there is a price in the lowering of the number we can extract. In between the extreme cases of low power lies the maximum power point, at which voltage  $V_{mp}$  the solar cell should be operated for electricity production. The electrical power provided by the solar cell at the maximum power point is

$$P_{el} = j_{sc} \times FF \times V_{oc} \quad (11)$$

If the fill factor is high the drop in current at high voltage is delayed, and we can extract the electrons at high voltage while

the current is still close to  $j_{sc}$ . For a good diode characteristic the power  $P$  increases linearly at low voltage, Fig. 2(b), and decreases abruptly at  $V > V_{mp}$ .

Combining eqn (4) and (11) the PCE can be obtained. Maximal efficiency for a solar cell that consists of a single bandgap absorber with ideal diode characteristic (see below eqn (24) and (26)) is given by the SQ limit and shown in Fig. 5(b).<sup>46</sup> In real, AM1.5G, conditions  $E_g = 1.35$  eV is the optimal, very close to the gap of GaAs (1.42 eV).<sup>63,64</sup>

As an example, a low quality solar cell with ohmic characteristic, which is straight instead of diode-like, is shown in Fig. 2(c) and (d). In this case, the photocurrent at maximum power is:  $j_{mp} = j_{sc}/2$ ,  $V_{mp} = V_{oc}/2$ , FF = 0.25, and the efficiency is very low. The comparison of two extreme cases in Fig. 2(c) shows that the shape of the  $jV$  curve has a major impact on the conversion efficiency.

### 3. Models and methods

It is clear that the experimental characterization of a solar cell involves a slow scan of the bias voltage from the short-circuit condition to the open-circuit condition (at least), at one or more fixed illumination level. The standard illumination condition is 1 sun (AM 1.5 G), but sometimes it is useful to apply 1/3 sun, for example, that represents the average outdoor operation conditions. By these means we obtain the main characteristics of the solar cell: the photocurrent, photovoltage, and fill factor.

However, the characterization by  $jV$  curves provides limited resources for the analysis of the mechanisms governing the performance. A thorough analysis requires discriminating several factors concerning series resistance, recombination parameters, carrier energetics, etc. These factors are not usually available simply by the analysis of  $jV$  curve data, notably because  $jV$  curves are “elastic” with respect to models and can be equally described by many different frameworks. A systematic analysis is possible however, by a combined analysis of current–voltage data and impedance data. The measurement of IS at each point allows us to separate resistances and capacitances providing detailed information about the electronic process at that point. Separation of different components of the resistance using IS, and their distinct analysis as a function of voltage, is a very valuable tool to determine the properties of the solar cell. Resistance generally describes electron transfer or transport events, whereas capacitances relate to electronic carrier accumulation and distribution in the device. Models, explained in the following section, allow us to determine the IS parameter and to plot them correctly in a voltage scale, so that a great deal of information about the operation of the solar cell is obtained. A recent overview of these methods has been presented recently<sup>65</sup> and additional tools of interpretation are provided here. A simultaneous description of the  $jV$  curve, recombination resistance, and capacitance as a function of the voltage in the solar cell provides a sound foundation for interpretation of the solar cells mechanisms.

#### 3.1 The diode model

We consider first the simple model shown in Fig. 1 and further elaborated in Fig. 8. The carrier transport limitations are neglected in a first approximation, and the Fermi levels are

homogeneous. Considering a possible internal potential drop  $V_s$  at series resistance  $R_s$ , the voltage measured at outer contacts, i.e., the applied voltage, is given by

$$V_{app} = V_F + V_s = V_F - jR_s \quad (12)$$

More generally, if the Fermi levels are not homogeneous, the output voltage of the active layer consists in the difference of Fermi levels at the contacts. For a layer of thickness  $L$ , with the electron-extraction contact at  $x = 0$

$$V_F = [E_{Fn}(x = 0) - E_{Fp}(x = L)]/q \quad (13)$$

Let us assume that  $E_{Fp}$  remains stationary under illumination, at the equilibrium Fermi level in the semiconductor  $E_{F0}$  (this means that hole carriers are much more abundant initially than electron carriers). In a DSC  $E_{F0} = E_{redox}$ , the redox level in the electrolyte. Therefore we focus on the concentration of electrons in the conduction band at energy  $E_c$  with effective density of states  $N_c$ , which is

$$n_c = N_c e^{(E_{Fn} - E_c)/k_B T} \quad (14)$$

where  $k_B$  is Boltzmann's constant and  $T$  is the temperature. We call  $n_c$  the free electrons, since the electron carriers may also be located in trap states in the bandgap. The density of free electrons can also be expressed as

$$n_c = n_0 e^{(E_{Fn} - E_{F0})/k_B T} \quad (15)$$

in terms of the dark equilibrium concentration  $n_0 = N_c e^{-(E_c - E_{F0})/k_B T}$ .

Without much loss of generality we consider that the n-material is nanostructured TiO<sub>2</sub>, and the p-material is a redox electrolyte, as in the characteristic configuration of a DSC.

Eqn (13) and (15) give the relationship of free electron density with the voltage

$$n_c = n_0 e^{qV_F/k_B T} \quad (16)$$

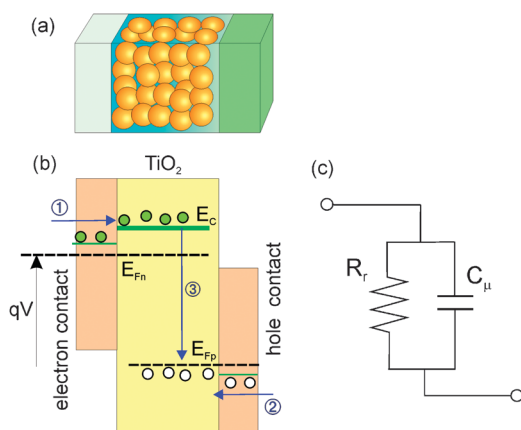


**Fig. 8** (a) Scheme of a DSC device. (b) Basic energy diagram indicating voltage injection of electrons (1) and holes (2) and recombination (3) processes in a DSC. Also shown are the transport energy levels and Fermi levels of electrons and holes, and the potential associated with separation of Fermi levels. Note that the electron injection contact is blocking for holes, and vice versa. (c) The basic equivalent circuit for an electrical perturbation.

In the absence of illumination this system is a diode where voltage injection of electrons and holes causes recombination current, as shown in Fig. 8(b). In addition to eqn (16) the ideal diode requires full selective boundary conditions for both kinds of carriers that are detailed below in eqn (59) and (60).

If the absorbed photon flux is  $\phi_{\text{abs}} \left( = \int_{\lambda_{\min}}^{\lambda_{\max}} \eta_{\text{IPCE}} \phi_{\text{ph}}^{\text{source}}(\lambda) d\lambda \right)$ , the carrier generation by incident light occurs at a rate  $G = \phi_{\text{abs}}/L$  per unit volume,  $L$  being the thickness of the absorber layer. The concentration of electrons is governed by the conservation equation

$$\frac{dn}{dt} = G - U_n + U_{n0} \quad (17)$$

where  $U_n$  is the recombination rate, and  $U_{n0}$  is a term that provides equilibrium at  $G = 0$ . We assume the following empirical model of recombination,

$$U_n = k_{\text{rec}} n_c^\beta \quad (18)$$

where  $k_{\text{rec}}$  is a constant with units  $\text{cm}^{-3(1-\beta)} \text{s}^{-1}$  and  $0 < \beta \leq 1$ . We call this model  $\beta$ -recombination<sup>32</sup> to imply that  $\beta$  is a constant.

We now apply eqn (17) and (18) to obtain the current density  $j$  withdrawn from the solar cell at steady state. By integration over the active film thickness<sup>65</sup> we obtain

$$j = q\phi_{\text{abs}} - qk_r L n_c^\beta + qk_r L n_0^\beta \quad (19)$$

which may be rewritten in the form of the diode equation

$$j = j_{\text{sc}} - j_0 (e^{q\beta V_F/k_B T} - 1) \quad (20)$$

with  $j_{\text{sc}} = q\phi_{\text{abs}}$  the short-circuit photocurrent, and  $m = 1/\beta$  the diode quality factor. The constant  $j_0$  determines the diode dark current and is defined as follows

$$j_0 = j_{0k} e^{-\beta E_c/k_B T} \quad (21)$$

where  $j_{0k}$  determines the recombination rate, independently of the conduction band position

$$j_{0k} = qk_r L N_c^\beta e^{\beta E_{F0}/k_B T} \quad (22)$$

so that finally

$$j = j_{\text{sc}} - j_{0k} e^{-\beta E_c/k_B T (e^{q\beta V_F/k_B T} - 1)} \quad (23)$$

Eqn (23) follows directly from the specific assumption of eqn (18). However, it should be emphasized that eqn (18) simply represents the empirically observed properties of recombination in a DSC with respect to the voltage.<sup>32</sup> The full form of the recombination current arising from charge transfer via a distribution of surface states is given in ref. 21 and 66. This model coincides with eqn (18) for the voltage dependence but has a large number of parameters (see below eqn (45) and (46)). Eqn (21) simplifies the treatment of empirical data by separation in the conventional ‘‘dark current’’ parameter ( $j_0$ ) of two effects that frequently have an important influence on the behaviour of DSC:  $E_c$ , that tracks possible changes of the position of the conduction band of the n-semiconductor, and  $j_{0k}$ , that represents changes in the charge transfer rate, e.g. by blocking the  $\text{TiO}_2$  surface. As a result in eqn (23) we have introduced a model based on the set of parameters,  $j_{\text{sc}}$ ,  $E_c$ ,  $j_{0k}$ , and  $\beta$ , that determine

the  $jV$  characteristic, according to the diode model described above. Later on it is explained that these parameters can be actually retrieved by combined analysis of  $jV$  curves and impedance data, although  $E_c$  can usually be given only in a comparative basis.

At the open circuit the carrier concentration is determined by the kinetic balance between photogeneration and recombination. From eqn (23) at  $j = 0$  we obtain the open-circuit voltage

$$V_{\text{oc}} = \frac{k_B T}{q\beta} \ln \left( \frac{j_{\text{sc}}}{j_0} + 1 \right) \approx \frac{k_B T}{q\beta} \ln \frac{j_{\text{sc}}}{j_0} = \frac{E_c}{q} + \frac{k_B T}{q\beta} \ln \frac{j_{\text{sc}}}{j_{0k}} \quad (24)$$

Eqn (24) stresses the effect of the four parameters defined in the model,  $j_{\text{sc}}$ ,  $E_c$ ,  $j_{0k}$ , and  $\beta$ , in the final  $V_{\text{oc}}$ . The voltage of maximum power  $V_{\text{mp}}$  is obtained by the solution of the equation  $dP_{\text{el}}/dV = 0$ , which can be expressed as

$$\left( 1 + \beta \frac{qV_{\text{mp}}}{k_B T} \right) e^{\beta qV_{\text{mp}}/k_B T} - e^{\beta qV_{\text{oc}}/k_B T} = 0 \quad (25)$$

The fill factor takes the form

$$\text{FF} = \frac{j(V_{\text{mp}}) V_{\text{mp}}}{j_{\text{sc}} V_{\text{oc}}} = \frac{V_{\text{mp}}}{V_{\text{oc}}} \left( \frac{e^{\beta qV_{\text{oc}}/k_B T} - e^{\beta qV_{\text{mp}}/k_B T}}{e^{\beta qV_{\text{oc}}/k_B T} - 1} \right) \quad (26)$$

Note that FF is again a function of the four parameters of the model and it can be expressed as only a function of  $V_{\text{oc}}$  and  $\beta$ . The fill factor is also well described by the analytically closed expression<sup>67</sup>

$$\text{FF}(V_{\text{oc}}) = \frac{V_{\text{r}} - \ln(V_{\text{r}} + 0.72)}{V_{\text{r}} + 1} \quad (27)$$

where the reduced voltage is  $V_{\text{r}} = \beta qV_{\text{oc}}/(k_B T)$ .

The lines in Fig. 9 give the FF as a function of  $V_{\text{oc}}$  for different values of  $m = 1/\beta$ , following eqn (27) where it is considered the ideal case in which the series resistance is zero. The FF of DSC and BHJ are given in Fig. 9, in comparison with record cells of several inorganic technologies.

As a first approximation we will discuss the effect on the solar cell performance of the variation of one of the four parameters while the others remain unchanged. The most straightforward cases are the variation of  $j_{\text{sc}}$  and  $E_c$ . Both the increase of  $j_{\text{sc}}$  or  $E_c$ , keeping the other three parameters

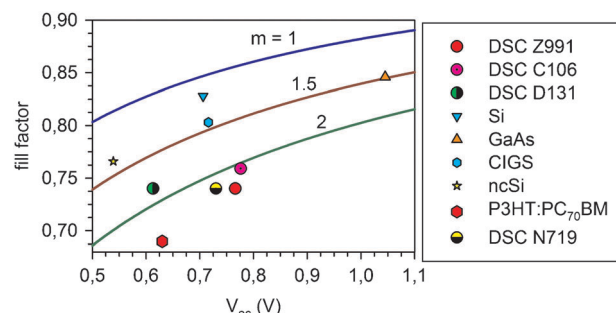


**Fig. 9** The fill factor of a Shockley diode as a function of the open-circuit voltage, according to the value of the ideality factor,  $m$ . The points are values corresponding to characteristics of DSC with dyes Z991 ( $\eta = 12.2\%$ ),<sup>173</sup> C106 ( $\eta = 11.3\%$ ),<sup>104</sup> D131 ( $\eta = 5.1\%$ ),<sup>174</sup> and N719 ( $\eta = 7.7\%$ ); the record cells in several inorganic technologies,<sup>175</sup> and an organic bulk heterojunction.<sup>176</sup> Series resistance effects are removed only for DSC N719.

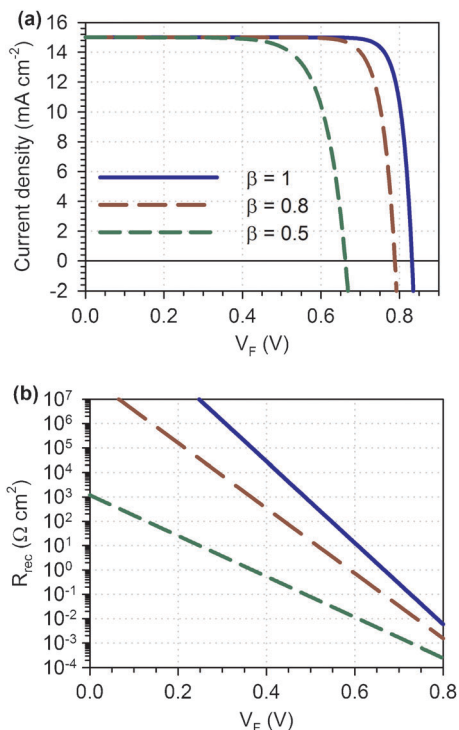


**Fig. 10** Theoretical calculation (diode model) of the current–voltage curve (a) and recombination resistance (b) of several solar cells differing only in the recombination exponent  $\beta$ , see the parameters used in the calculation in Table 1.

constant, produce an enhancement of cell performance as this increment produces an increase of  $V_{\text{oc}}$ , see eqn (24). Fig. 10(a) shows the influence of the  $\beta$  parameter on the shape of current–voltage curves (keeping the other three parameters constant), and the corresponding efficiencies are given in Table 1. Note in Table 1 that the change of  $\beta$  alone changes drastically the dark current  $j_0$ . Finally, comparing samples B and C in Fig. 11, the effect of the variation of  $j_{0k}$  is highlighted. A decrease of  $j_{0k}$  produces an increase of performance. Note that the parameter  $j_{0k}$  is the most difficult one to analyze as it is dependent on the recombination rate  $k_{\text{rec}}$  and  $\beta$ , see eqn (22). Obviously, the analyzed cases are not the most general ones and variations of more than one parameter at the same time can be expected. But in any case, the analysis in terms of the four parameters of the diode model will help to optimize the solar cell performance.

Fig. 11(a) illustrates that changes of internal parameters of the DSC, indicated in Table 2, produce modifications of the performance. If the conduction band level is lowered, the Fermi level of electrons in  $\text{TiO}_2$  can raise less and the

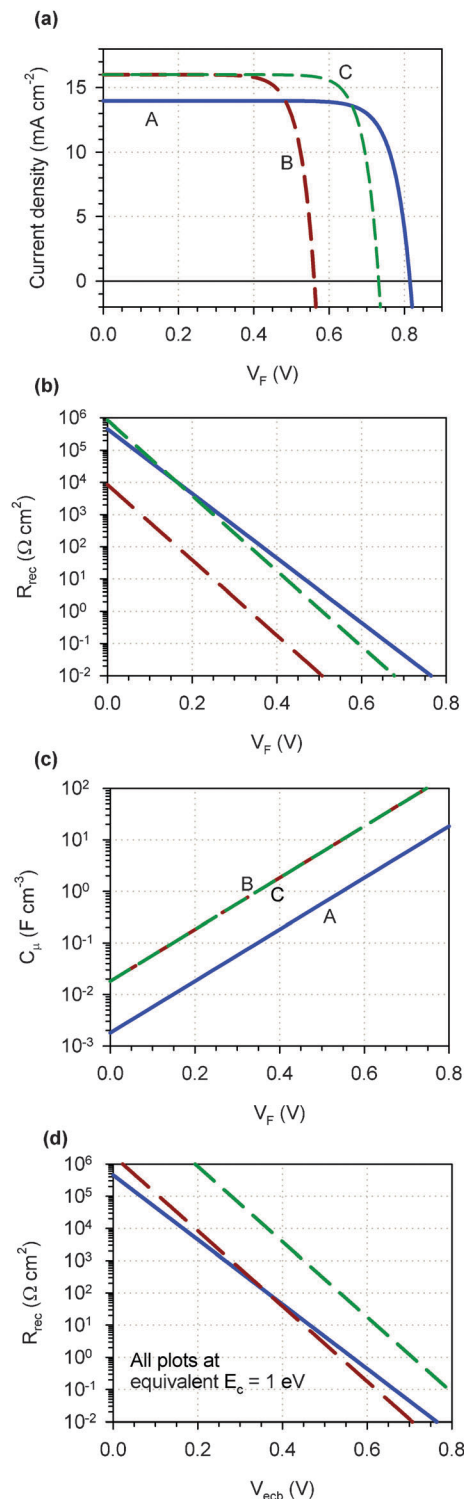


**Fig. 11** Theoretical calculation (diode model) of the current–voltage curve (a) and recombination resistance (b), see the parameters used in the calculation in Table 2. (c) Calculated capacitance using the expression  $C_\mu = qN_L/k_B T_0 \exp[(E_{Fn} - E_c)/k_B T_0]$ , with parameters  $N_L = 10^{20} \text{ cm}^{-3}$ ,  $T_0 = 1000 \text{ K}$ . (d) The resistances plot at the same equivalent position of the edge of the conduction band, taking A as a reference.

photovoltage decreases. However, at the same time the charge injection from the dye becomes facilitated and the photocurrent,

**Table 1** Simulation parameters for current–voltage curves in Fig. 10

| $\beta$                    | 1.0                    | 0.80                   | 0.50                  |
|----------------------------|------------------------|------------------------|-----------------------|
| $E_c - E_{F0}/\text{eV}$   | 1.0                    | 1.0                    | 1.0                   |
| $j_{sc}/\text{mA cm}^{-2}$ | 15.0                   | 15.0                   | 15.0                  |
| $j_{0k}/\text{mA cm}^{-2}$ | $10^4$                 | $10^4$                 | $10^4$                |
| $j_0/\text{mA cm}^{-2}$    | $1.98 \times 10^{-13}$ | $4.33 \times 10^{-10}$ | $4.45 \times 10^{-5}$ |
| $V_{\text{oc}}/\text{V}$   | 0.83                   | 0.79                   | 0.66                  |
| FF                         | 0.86                   | 0.83                   | 0.74                  |
| $\eta$                     | 10.7                   | 9.8                    | 7.3                   |

**Table 2** Simulation parameters for current–voltage curves in Fig. 11

|                         | A                     | B                     | C                     |
|-------------------------|-----------------------|-----------------------|-----------------------|
| $\beta$                 | 0.60                  | 0.70                  | 0.70                  |
| $E_c - E_{F0}$ /eV      | 1.00                  | 0.80                  | 0.80                  |
| $j_{sc}$ /mA cm $^{-2}$ | 14.0                  | 16.0                  | 16.0                  |
| $j_{0k}$ /mA cm $^{-2}$ | 1000                  | 10 000                | 100                   |
| $j_0$ /mA cm $^{-2}$    | $9.50 \times 10^{-8}$ | $4.42 \times 10^{-6}$ | $4.42 \times 10^{-8}$ |
| $V_{oc}$ /V             | 0.82                  | 0.56                  | 0.7319                |
| FF                      | 0.80                  | 0.76                  | 0.80                  |
| $\eta$                  | 9.12                  | 6.88                  | 9.43                  |

$j_{sc}$ , increases, see curves A and C in Fig. 11(a). Together with the modification of the conduction band, it is important to consider the recombination rate, since this determines the number of electrons that can effectively be accumulated. Thus lowering the conduction band (from A to B) decreases the efficiency if a simultaneous increase of recombination rate ( $j_{0k}$ ) occurs. But the modification of the conduction band (A to C) increases the performance if  $j_{0k}$  decreases. In addition, changes of the conduction band may also produce changes of the  $\beta$ -parameter,<sup>68</sup> which has an important influence on the FF, as discussed in Fig. 9.

We should emphasize that these representations are intended to show the effects of recombination in the  $jV$  curve and the effect of series resistance is not included (*i.e.*, we use the potential related to the separation of Fermi levels,  $V_F$ ). Of course the effect of series resistance is very important, especially for large area cells, and this is further discussed below.

Finally we remark two important points about the analysis of experimental data.

First, we have explained in detail that the model of eqn (23) attempts to distinguish the critical factors governing recombination, as represented by parameters that describe the energetic and kinetic components ( $E_c$ ,  $j_{0k}$ , and  $\beta$ ), which are separated from the variable electron density. An important aspect of graphical analysis is therefore to plot measured parameters as a function of Fermi level (the internal voltage  $V_F$ ), and in addition, to provide the appropriate shift of energetics, as outlined in Fig. 11.

Second, it should be recognized that the model developed in eqn (23) is restricted for application at a forward bias, *i.e.* at a voltage larger than zero voltage (Fig. 2(a)). Obviously the model provides the result  $j = j_0$  at reverse in the dark, but in practice, the current in these conditions in DSC and probably also in BHJ is related to the behaviour of contacts and not to the mechanism of bulk recombination which is represented in eqn (23). In the remaining part of this review we often describe the *capacitance* at a reverse bias, but not the current, which is often not related to recombination in the operation conditions of the solar cell.

### 3.2 The fundamental ac equivalent circuit

In the previous section we have presented the basic model describing steady state performance of a solar cell. Let us summarize the derivation of the ac impedance behaviour corresponding to this model.<sup>65</sup> In IS the solar cell is set at a certain steady state of illumination,  $\bar{G}$ , and applied voltage,  $\bar{V}$ , with the corresponding current  $\bar{j}$  given in eqn (20). A small

amplitude, harmonic time-dependent perturbation of voltage is applied, so that  $V = \bar{V} + \hat{\phi}_n(t)$ , with the associated change of current,  $j = \bar{j} + \hat{j}(t)$ . The time-dependent behaviour of the solar cell is described by eqn (17). The carrier density dependence on time takes the form

$$n(t) = \bar{n} + \hat{n}(t) \quad (28)$$

The variation of voltage applied in the solar cell produces a variation of the electron Fermi level, which changes as

$$E_{Fn}(t) = \bar{E}_{Fn} + q\hat{\phi}_n(t) \quad (29)$$

Expanding to first order eqn (14) we obtain

$$n(t) = \bar{n} + \frac{\partial n}{\partial E_{Fn}} q\hat{\phi}_n \quad (30)$$

The derivative in eqn (30) consists of a *chemical capacitance*<sup>69,70</sup> that is defined (per unit volume) as

$$c_\mu = q^2 \frac{\partial n}{\partial E_{Fn}} \quad (31)$$

The macroscopic capacitance of the film is given by

$$C_\mu = v_{eff} c_\mu = v_{eff} q^2 \frac{\partial n}{\partial E_{Fn}} \quad (32)$$

where  $v_{eff}$  is the effective volume of the film

$$v_{eff} = LA(1 - p) \quad (33)$$

Here  $A$  and  $L$  are the cell area and thickness, respectively, and  $p$  is the porosity. For the free electrons in the conduction band level, defined by eqn (14), we have

$$c_\mu^{cb} = q^2 \frac{\partial n_c}{\partial E_{Fn}} = \frac{q^2 n_c}{k_B T} = \frac{N_c q^2}{k_B T} \exp[-(E_c - E_{Fn})/k_B T] \quad (34)$$

If there are abundant trap states that produce a density of localized electrons  $n_L$ , the chemical capacitance per unit volume is associated to the DOS in the bandgap,  $g(E)$ <sup>69,71</sup>

$$c_\mu^{\text{trap}}(E) = q^2 \frac{\partial n_L}{\partial E_{Fn}} = qg(E_{Fn}) \quad (35)$$

In nanostructured metal-oxides the DOS is usually given by

$$g(E_{Fn}) = \frac{\alpha q N_L}{k_B T} \exp[\alpha(E_{Fn} - E_c)/k_B T], \quad (36)$$

being  $N_L$  the total number of states below the conduction band and  $\alpha$  a parameter that describes their distribution.

Next we expand the recombination term in eqn (6) and we obtain

$$U_n(t) = \bar{U}_n + \left( \frac{\partial \bar{U}_n}{\partial n} \right) \hat{n} \quad (37)$$

Let us introduce the macroscopic recombination resistance<sup>16,21</sup>

$$R_{rec} = \frac{1}{qA} \left( \frac{\partial j_{rec}}{\partial E_{Fn}} \right)^{-1} = \frac{1}{A} \left( \frac{\partial j_{rec}}{\partial V_F} \right)^{-1} \quad (38)$$

where  $j_{rec}$  is the recombination current,  $j_{rec} = qL(1 - p)U_n$ , and we apply the relationship  $qdV_F = dE_{Fn}$  that follows

from eqn (13). The specific recombination resistance per unit volume  $r_{\text{rec}}$  can be written as

$$r_{\text{rec}} = \frac{1}{q^2} \left( \frac{\partial U_n}{\partial E_{Fn}} \right)^{-1} = \frac{1}{c_{\mu}^{\text{cb}}} \left( \frac{\partial U_n}{\partial n} \right)^{-1} = v_{\text{eff}} R_{\text{rec}} \quad (39)$$

Therefore we find that the second term on the right of eqn (37) relates to the recombination resistance  $r_{\text{rec}}$ . Taking into account the definition of the free electron lifetime<sup>72</sup>

$$\tau_0 = \left( \frac{\partial U_n}{\partial n_c} \right)^{-1} \quad (40)$$

we obtain the relationship

$$r_{\text{rec}} c_{\mu}^{\text{cb}} = \tau_0 \quad (41)$$

This brief discussion illustrates the derivation of chemical capacitance and recombination resistance from fundamental considerations. Applying a small perturbation in eqn (17), it can be shown<sup>65</sup> that the equivalent circuit representing the impedance  $Z = \hat{\rho}_n/\hat{j}$  of the solar cell is given by the parallel combination of  $c_{\mu}$  and  $r_{\text{rec}}$ , as indicated in Fig. 8(c). In terms of IS the resistance  $R_{\text{rec}}$  records recombination in the solar cell, while  $C_{\mu}$  relates to the carrier accumulation and splitting of the Fermi levels.

### 3.3 The recombination resistance

In general the resistance measured in IS is a derivative of the current–voltage curve, see Fig. 2(a) and eqn (38). With the spectral resolution of the different components commented later, it is possible to obtain the recombination resistance as a function of the voltage. For the recombination model of eqn (18) we obtain from eqn (39)

$$r_{\text{rec}} = \frac{k_B T}{q \beta j_0} e^{-q \beta V_F / k_B T} \quad (42)$$

The recombination resistance, therefore produces a rather direct view of the recombination process. This can be appreciated in the simulations of Fig. 10(b) and 11(b). First we note that the derivative procedure, intrinsic to the measurement of small perturbation resistance, removes the photocurrent, so that  $R_{\text{rec}}$  shows directly the exponential variation of the recombination rate, depending on  $E_c$ ,  $j_{0k}$ , and  $\beta$ . And secondly, small changes in the recombination mechanism become visible in the measurement, *e.g.* a change in the slope due to the modification of the parameter  $\beta$ , see Fig. 10(b).

The simulation of Fig. 10 shows a situation that is often found in practice, as commented above. Changes of the materials combination of a DSC produce sometimes large changes, and sometimes subtle modifications, but even the latter may provide a significant improvement of about 1% efficiency, and it is important to determine the origin of the gain.

Let us discuss the frequently observed modifications using the four parameters of the model  $j_{sc}$ ,  $E_c$ ,  $j_{0k}$ , and  $\beta$ . The most characteristic variation that occurs in experiments is a change of the conduction band of titania,  $E_c$ , with respect to the redox electrolyte. This change can be read from the chemical capacitance, which describes the density of states of  $\text{TiO}_2$  as indicated in Fig. 12, and is consequently shifted along the

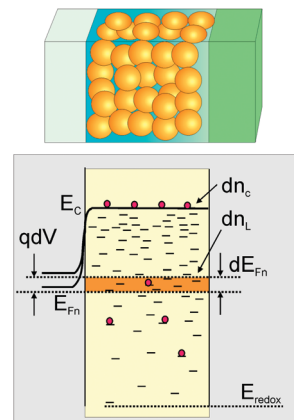


**Fig. 12** Electron energy diagram illustrating the behavior of a nanostructured  $\text{TiO}_2$  electrode (shown in the top scheme) when a variation  $dV$  of the electrochemical potential of electrons  $E_{Fn}$  (Fermi level) is applied, assuming that the conduction band energy ( $E_c$ ) remains stationary with respect to the redox level,  $E_{\text{redox}}$ . Changes of occupancy both of conduction band,  $dn_c$ , and trapped electrons in localized levels,  $dn_L$  (shaded region of the bandgap), are indicated. This drawing shows that the chemical capacitance is a measure of the density of states in the bandgap, when  $dn_L \gg dn_c$ .

voltage scale.<sup>16,71</sup> An upwards displacement of the  $\text{TiO}_2$  conduction band produces a shift to higher  $V_F$ , as can be seen from the comparison between the chemical capacitance of samples B and C and  $C_{\mu}$  for sample A, see Fig. 11(c). A change of the conduction band may be caused by the change of the dye, or the coabsorbents, or other factors. The modification of the surface may induce additional changes of both the rate constant for recombination,  $j_{0k}$ , and the parameter  $\beta$ . As commented previously, comparison of curves A and C in Fig. 11(a) illustrates the fact that a lowering of  $E_c$  produces a decrease in  $V_{oc}$  but a gain in  $j_{sc}$ . Comparing curves B and C the critical factor for the larger efficiency of curve C is that for similar  $\beta$ , recombination has been slowed down in C as observed in parameter  $j_{0k}$ , see Table 2. Such a type of change is rather difficult to determine from the current–voltage curve. In the recombination resistance shown in Fig. 11(b) we see that  $R_{\text{rec}}$  is similar for curves A and C, and since  $E_c$  is lower for curve C, it means that  $j_{0k}$  must also be lower for C. This fact is difficult to unveil from the representation plotted in Fig. 11(b), as the combination of two effects are considered at the same time  $E_c$  position and cell recombination, represented by  $j_{0k}$ .

An important tool to correctly evaluate the recombination rate is therefore to plot the recombination resistances of different devices at the same equivalent value of the position of the conduction band. Therefore we define a suitable potential,

$$V_{\text{ecb}} = V_F - \Delta E_c / q \quad (43)$$

where “ecb” stands for “common equivalent conduction band” and

$$\Delta E_c = E_c - E_{c,\text{ref}} \quad (44)$$

is the shift of the conduction band with respect to a reference sample. We introduce eqn (43) and (44) in eqn (42), and

we, obtain the following expression for the recombination resistance:

$$r_{\text{rec}} = \frac{k_{\text{B}}T}{q\beta j_{0k}} e^{-\beta(qV_{\text{ccb}} + E_{\text{c,ref}})/k_{\text{B}}T} \quad (45)$$

Therefore, when plotted with respect to  $V_{\text{ccb}}$ , differences in the recombination resistance correspond exactly to the variation of the reciprocal of the kinetic parameter  $j_{0k}$ , removing the influence of the conduction band position. The analysis is more complicated if the samples present different values of the DOS parameter  $\alpha$  or recombination exponent  $\beta$ .

Using the shift evaluated from the capacitance, we replot the recombination resistances in the  $V_{\text{ccb}}$  scale in Fig. 11(d), taking A as reference and displacing the voltage scale by  $\Delta V = +0.2$  V for B and C, see Table 2. Now we see clearly that the recombination flux is much less in the cell C than in both A and B, observing a higher recombination resistance for cell C. We also observe that the recombination flux is similar in A and B. Although  $j_{0k}$  is higher in B, the higher rate of charge transfer is compensated by a higher  $\beta$  than in A. In this way the analysis of the recombination resistance provides detailed information on the causes of performance of DSC. This approach has been applied to DSC with different types of molecular<sup>60,62</sup> and quantum dot sensitizers,<sup>36,73</sup> and has been implemented in specific software for data treatment ([www.istest.eu](http://www.istest.eu)).

Charge recombination in the DSC is the recombination of the electrons from the  $\text{TiO}_2$  surface to the acceptor species in the electrolyte. A number of papers have formulated the theories for charge transfer from a distribution of surface states defined by a temperature parameter,  $T_0$ .<sup>21,66,68,72,74</sup> It was shown that the recombination resistance is described by the expression<sup>21</sup>

$$r_{\text{rec}} = r'_0 \exp \left[ \frac{1}{k_{\text{B}}T} \left( \beta(E_{\text{Fn}} - E_{\text{F0}}) - \frac{(E_{\text{Fn}} - E_{\text{F0}})^2}{4\lambda} \right) \right] \quad (46)$$

with the prefactor

$$r'_0 = \frac{T_0 \sqrt{\pi \lambda k_{\text{B}} T}}{q^2 L k_0 c_{\text{ox}} N_s T} \exp \left[ \frac{E_C - E_{\text{redox}}}{k_{\text{B}} T_0} + \frac{\lambda}{4k_{\text{B}} T} \right] \quad (47)$$

Here  $\lambda$  is the reorganization energy of the redox couple, and

$$\beta = \frac{1}{2} + \frac{T}{T_0} \quad (48)$$

We observe that eqn (46) is more general than (45), but eqn (45) is obtained in the voltage range  $qV_F \ll \lambda$ , and in this range  $\beta$ -recombination model holds.<sup>32,72</sup> Furthermore, eqn (45) produces a detailed view of the empirical parameter  $j_{0k}$  introduced above in terms of a microscopic model. In addition, eqn (46) provides an interpretation of the parameter  $\beta$  in terms of the distribution of surface states.

### 3.4 Depletion capacitances

Apart from the chemical capacitance, which is associated to the displacement of the Fermi level in the bandgap, in many solar cells a Schottky barrier exists at the contact of the semiconductor with a metal, or at the semiconductor/electrolyte interface. The barrier produces a variable capacitance that is

dielectric in origin. When the cell is reverse biased the space-charge region in the barrier increases and the capacitance decreases. And vice versa, a forward bias reduces the extent of the barrier and the capacitance becomes larger. The thickness of the depletion layer relates to the voltage across the layer as<sup>75</sup>

$$w = w_0 V_{\text{sc}}^{1/2} \quad (49)$$

where

$$w_0 = \left( \frac{2\epsilon_r \epsilon_0}{qN} \right)^{1/2} \quad (50)$$

$$N = \frac{N_A N_D}{N_A + N_D} \quad (51)$$

$\epsilon_0$  being the permittivity of free space,  $\epsilon_r$  the permittivity of the material, and  $N_A$  and  $N_D$  the doping concentration of p and n regions respectively. For p-type material  $N \approx N_A$ . The depletion capacitance is given by

$$C_{\text{sc}} = \frac{A\epsilon_r \epsilon_0}{w} = \frac{A\epsilon_r \epsilon_0}{w_0 V_{\text{sc}}^{1/2}} \quad (52)$$

If  $V_{\text{app}}$  is the applied voltage, then  $V_{\text{sc}} = V_{\text{app}} - V_{\text{bi}}$ , where  $V_{\text{bi}}$  is the built-in potential between the two materials in contact (corresponding to the flat-band potential  $V_{\text{fb}}$ ). It follows from eqn (49) and (52) that  $C_{\text{sc}}^{-2}$  depends linearly on  $V_{\text{sc}}$  (the Mott–Schottky relationship):

$$C_{\text{sc}}^{-2} = \frac{2}{A^2 q \epsilon_r \epsilon_0 N_A} (V_{\text{bi}} - V_{\text{app}}) \quad (53)$$

In Fig. 13 we show the combination of two capacitances as is found in many cases.<sup>38,43</sup> At a reverse bias, the overall capacitance is dominated by the dielectric barrier capacitance

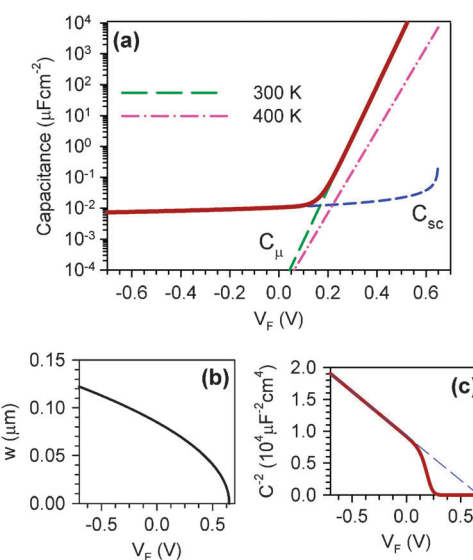


**Fig. 13** Theoretical calculation of (a) capacitances in a silicon solar cell: chemical capacitance  $C_{\mu}$  (calculated at two different temperatures, as indicated), capacitance in the depletion layer  $C_{\text{sc}}$ , and total capacitance (thick line). (b) Width of the space charge region. (c) Mott–Schottky plot. Parameters used in the simulation:  $L = 300 \mu\text{m}$ ,  $T = 300 \text{ K}$ ,  $V_{\text{bi}} = 0.65 \text{ V}$ ,  $\epsilon_r = 1$ ,  $N_A = 10^{16} \text{ cm}^{-3}$ ,  $n_0 = 10^8 \text{ cm}^{-3}$ .

of eqn (52) at one contact, while the chemical capacitance becomes very large as the forward bias increases and finally governs the cell capacitance.

In many situations we find an additional constant capacitance at the surface of the semiconductor that takes a part of the voltage (and causes a displacement of the edge of semiconductor band, or electron affinity). The physical origin of the capacitance may be a thin dielectric layer, or the double layer capacitance at the semiconductor/electrolyte interface. It is usual to simplify the treatment of the double layer capacitance in terms of a constant Helmholtz capacitance,  $C_H$  (although this is strictly correct only for a concentrated electrolyte so that the potential drop in the diffuse layer can be neglected). The presence of such a constant capacitance due to either a dielectric layer or the Helmholtz capacitance produces a displacement of the Mott–Schottky (MS) plot. For example, for p-type material in contact with an electrolyte, one obtains the relationship<sup>76,77</sup>

$$C^{-2} = \frac{2}{A^2 q \epsilon \epsilon_0 N_D} (V_{fb} - V_{app}) + \frac{1}{C_H^2} \quad (54)$$

An additional effect must be considered for cylindrical semiconductors of small size, such as nanowires and nanotubes, since the depletion layer obtains a circular form,<sup>78,79</sup> see Fig. 14. This effect is more prominent if the doping density is very low, in which case the depletion region penetrates towards the center of the wires. Solving the Poisson equation, the potential difference across the semiconductor space-charge region can be calculated as

$$V_{sc} = \frac{qN_D}{2\epsilon} \left[ \frac{1}{2} (x^2 + R^2) + x \ln \left( \frac{R}{x} \right) \right] \quad (55)$$

The capacitance may be found using  $C = dQ/dV_{sc}$ , with  $Q = qN_D\pi(R^2 - x^2)Ld_{nw}$ ,  $d_{nw}$  being the density of nanowires per flat surface unit,  $R$  the radius of the wire, and  $x$  the flat potential region, see Fig. 14. Thus we obtain<sup>79</sup>

$$C = \frac{2\pi\epsilon L d_{nw}}{\ln(R/x)} \quad (56)$$

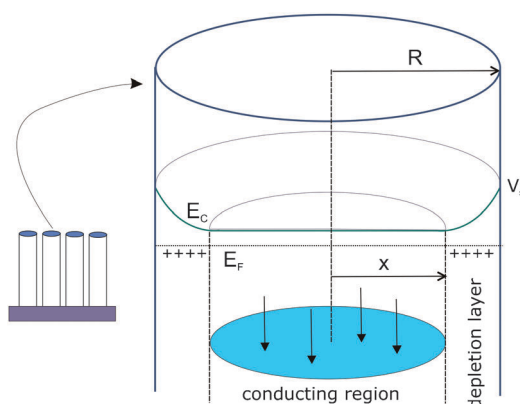


**Fig. 14** Schematic energy diagram of a nanowire indicating the depletion layer at the surface and the quasineutral (conducting) region of radius  $x$  in the center.  $V_s$  is the potential at the surface,  $E_C$  is the lower edge of the conduction band, and  $E_F$  is the Fermi level.

### 3.5 Carrier generation, collection and distribution in the diffusion–recombination model

We have described above the derivation of the  $jV$  curve in a simple diode model based on homogeneous photogeneration and fast transport. This is useful to illustrate the basic meaning of the parameters derived in IS, and for a first approximation to the connection between impedance parameters and shape of the  $jV$  curve. A more complete analysis requires detailed consideration of the photoexcitation along the active thickness, efficiency of injection and regeneration, and the distribution of both the electron and hole carriers. It has been established that the characteristics of nanocrystalline photoelectrochemical cells are well described by a model considering generation, diffusion and recombination of electrons along the nanostructured metal oxide.<sup>80,81</sup> Detailed description of these methods has been provided recently in papers by Barnes,<sup>82,83</sup> Halme,<sup>84</sup> Gagliardi<sup>85</sup> and their coworkers. We briefly summarize these methods here.

To describe in a general situation the current–voltage relationship, and the small signal amplitude transference functions, it is necessary to solve a diffusion–recombination model for electrons of the type

$$\frac{\partial n_c(x)}{\partial t} = G(x) - \frac{\partial J_n(x)}{\partial x} - (U_n(x) - U_{n0}) - \frac{\partial n_L(x)}{\partial t} \quad (57)$$

here  $J_n$  is the electron flux that is given by Fick's diffusion law with diffusion coefficient  $D_0$

$$J_n(x) = -D_0 \frac{\partial n_c(x)}{\partial x} \quad (58)$$

These equations consider both the free electron density  $n_c$  that can be transported by diffusion, eqn (58), and localized (trapped) electrons  $n_L$ ,<sup>86,87</sup> see ref. 88 for an extension that considers multiple trapping electron transport. Taking the contact of the active layer with the collecting substrate at  $x = 0$ , the boundary conditions are

$$n_c(0) = n_{0e} e^{qV_F/k_B T} \quad (59)$$

$$j = -qJ_n(0); J_n(L) = 0 \quad (60)$$

The generation term  $G(x)$  is the position-dependent volume photogeneration rate, which is typically given by an exponential term for Beer–Lambert light absorption that is proportional to the incident photon flux but depends on a number of factors. Thus for illumination from the substrate/electrode (SE) interface

$$G_{SE}(x) = \eta_{sep}(1 - S_{SE})\alpha_d e^{-(\alpha_d + \alpha_h)\phi_0} \quad (61)$$

and for light incident from the electrolyte/electrode (EE) side

$$G_{SE}(x) = \eta_{sep}(1 - S_{CE})T_h \alpha_d e^{-(\alpha_d + \alpha_h)(L-x)\phi_0} \quad (62)$$

Here  $\phi_0$  is the incident photon flux,  $\eta_{sep}$  is an efficiency of charge separation,  $\alpha_d$  and  $\alpha_h$  are the absorption coefficients of the dye molecule and redox carrier in the porous matrix, respectively,  $S$  is the incident light loss at the indicated contact, for example, the reflection loss at interfaces, and  $T_h$  is the transmittance of the bulk of the hole conducting medium.

The recombination term  $U_n$  has been already discussed above. As an example we write the  $\beta$ -recombination model as

$$U_n(x) = k_{\text{rec}} c_h n_c(x)^\beta \quad (63)$$

We have included the concentration of the hole carrier,  $c_h$ , in the recombination term of the transport equation. A hole or redox carrier can be subjected to transport limitations and additional equations on  $c_h$  are then needed to complete the model.

In steady state, time-dependent terms in eqn (57) play no role and the resulting equation is

$$0 = G(x) - \frac{\partial J_n(x)}{\partial x} - (U_n(x) - U_{n0}) \quad (64)$$

By combining with eqn (58) we obtain the equation

$$D_0 \frac{\partial^2 n_c(x)}{\partial x^2} - (U_n(x) - U_{n0}) + G(x) = 0 \quad (65)$$

Fig. 15(a) shows the profile of electron concentrations in dark and light for illumination from the substrate side at voltages close to  $V_{oc}$ , by steady-state solution of this model with  $c_h$  constant and  $\beta = 1$ . In this example the diffusion length is half the thickness of the sample and other examples (for shorter and longer diffusion length) are shown in ESI.† Fig. 15(b) shows the corresponding distribution of the Fermi level of electrons. Solving the electron distribution, the current and voltage in the external circuit are obtained from eqn (59) and (60). The  $jV$  curve determined in this example is shown in Fig. 15(c).

The ac impedance model requires solving the linearized equations

$$i\omega \hat{n}_c(x) = -\frac{\partial \hat{J}_n(x)}{\partial x} - \frac{\hat{n}_c(x)}{\tau_0(x)} - i\omega \hat{n}_L(x) \quad (66)$$

$$\hat{J}_n = -D_0 \frac{\partial \hat{n}_c}{\partial x} \quad (67)$$

Note that the free carrier lifetime  $\tau_0$  depends on the position as indicated in eqn (40).<sup>32,72</sup> The term of the trapped electrons in eqn (57) and (66) may require additional kinetic equations to describe the processes of trapping and release.<sup>87,89</sup> However if such processes are fast, the traps remain in equilibrium with free electrons at all times and  $n_L$  is simply a function of the free electrons Fermi level (this is termed as the quasistatic approximation).<sup>86</sup> If we define an equivalent local ac current density as

$$\hat{j}_n(x) = -q \hat{J}_n(x) \quad (68)$$

we can write eqn (66) and (67) as

$$i\omega (c_\mu^{\text{cb}} + c_\mu^{\text{trap}}) \hat{\phi}_n + r_{\text{rec}}^{-1} \hat{\phi}_n - \frac{\partial \hat{j}_n}{\partial x} = 0 \quad (69)$$

$$\hat{j}_n = r_{\text{tr}}^{-1} \frac{\partial \hat{\phi}_n}{\partial x} \quad (70)$$

Here  $r_{\text{tr}}$  is a transport resistance defined as

$$r_{\text{tr}} = \frac{1}{D_0 c_\mu^{\text{cb}}} \quad (71)$$

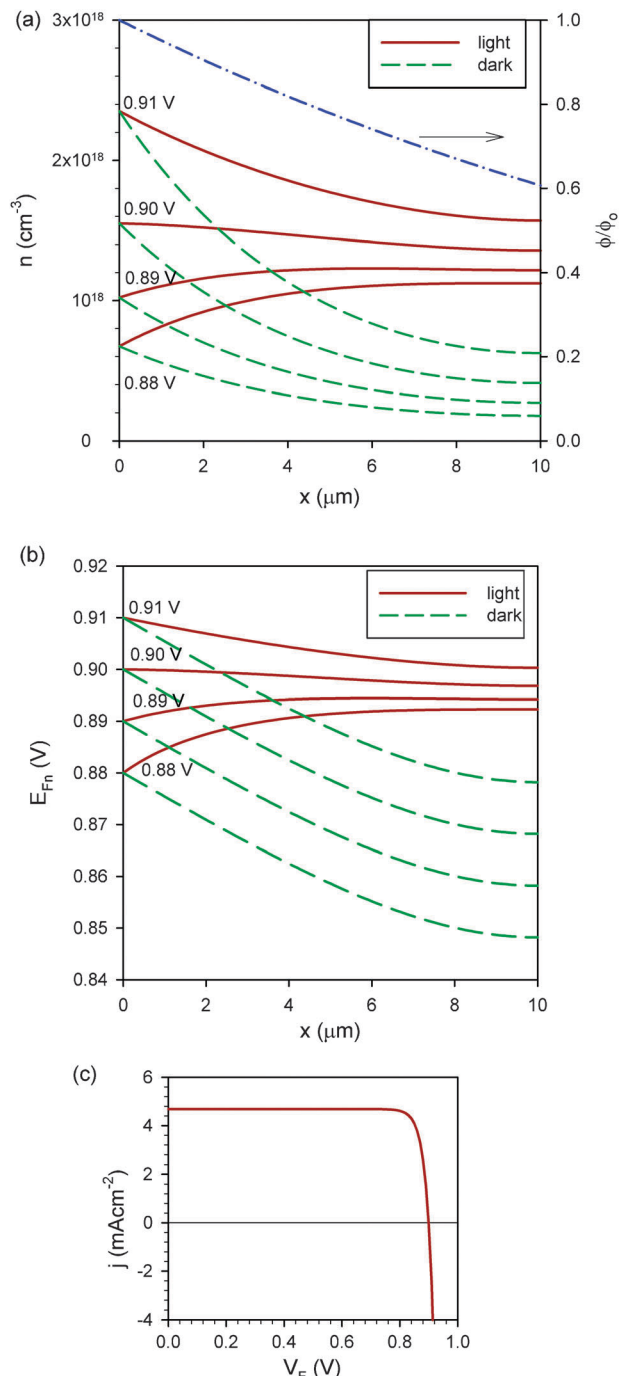


**Fig. 15** (a) Carrier distribution by diffusion–recombination of electrons and photogeneration profile in a nanostructured film with  $L = 10 \mu\text{m}$ , in dark and under incident photon flux  $\phi_0 = 1.45 \times 10^{17} \text{ cm}^{-2} \text{ s}^{-1}$ , at the indicated voltages at the contact. Parameters: absorption coefficient  $\alpha_{\text{abs}} = 500 \text{ cm}^{-1}$ , diffusion coefficient  $D_0 = 10^{-5} \text{ cm}^2 \text{ s}^{-1}$ , diffusion length  $L_n = 0.5L$ ,  $T = 300 \text{ K}$ ,  $E_{F0} = 0 \text{ eV}$ ,  $E_c = 1 \text{ eV}$ ,  $N_c = 10^{20} \text{ cm}^{-3}$ . (b) The Fermi level of electrons and (c) current density–voltage for the same model system.

The quantity in the denominator of eqn (71) corresponds to the electron conductivity<sup>88</sup>

$$\sigma_n = D_0 c_\mu^{\text{cb}} = \frac{q^2 n_c D_0}{k_B T} \quad (72)$$

Applying Kirchhoff rules, it can be shown that eqn (69) and (70) lead to a distributed equivalent circuit which can be represented as a transmission line.<sup>15,90,91</sup> The impedance model can be therefore formulated in terms of the specific elements  $c_\mu^{\text{cb}}$ ,  $c_\mu^{\text{trap}}$ ,  $r_{\text{rec}}$  and  $r_{\text{tr}}$ . In addition to the circuit  $c_\mu - r_{\text{rec}}$ , associated to the chemical capacitance in parallel with recombination resistance, shown in Fig. 8(c), the diffusion process introduces another component in the equivalent circuit, which is the transport resistance, see Fig. 16.

All these elements are a function of the free electron density (or Fermi level  $E_{\text{Fn}}$ ), and it follows that in a situation as in Fig. 15(a) the elements in the transmission line are a function of the position. The solution to the ac problem requires to solve first eqn (63) and then to calculate the impedance by summation of the equivalent circuit elements. Note that differences between dark and light are expected, a problem that has been recently treated with other methods by Barnes *et al.*<sup>92</sup> However the difference of carrier density between dark and light is small if the diffusion length is long, see ESI.†

The presence of the trap capacitance in eqn (69) has important consequences, as it affects the measured kinetic parameters. If we introduce the trapping factor<sup>86</sup>

$$\delta_L = \left(1 + \frac{\partial n_L}{\partial n_c}\right) \approx \frac{\partial n_L}{\partial n_c} = \frac{c_\mu^{\text{trap}}}{c_\mu^{\text{cb}}} \quad (73)$$

the measured diffusion coefficient and lifetime are<sup>72</sup>

$$D_n = D_0 / \delta_L \quad (74)$$

$$\tau_n = \delta_L \tau_0 \quad (75)$$

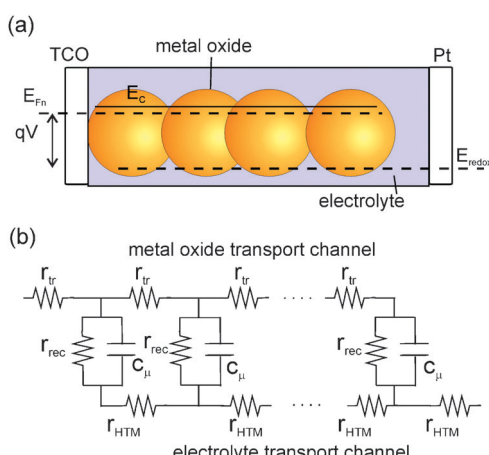


**Fig. 16** (a) Electron energy diagram of a nanostructured metal oxide electrode in contact with a redox electrolyte (or hole conducting medium), illustrating the electrochemical potential of electrons  $E_{\text{Fn}}$  (Fermi level) when a voltage  $V$  is applied to the substrate, and assuming that conduction band energy ( $E_c$ ) remains stationary with respect to the redox level,  $E_{\text{redox}}$ . (b) The equivalent circuit (transmission line model) for a small periodic ac perturbation that contains the resistance for electron transport along the metal oxide nanoparticles,  $r_{\text{tr}}$ ; the resistance in the hole transport medium (hole or ion conduction)  $r_{\text{HTM}}$ ; the recombination resistance at the metal oxide/electrolyte interface,  $r_{\text{rec}}$ ; and the chemical capacitance for charge accumulation in the metal oxide particles,  $c_\mu$ .

### 3.6 Diffusion–recombination impedance model for homogeneous carrier distribution

The derivation of the impedance of the diffusion–recombination model<sup>15</sup> and application in DSC<sup>16,21</sup> has been reviewed in a book chapter.<sup>65</sup> The impedance model described here is the solution of small ac perturbation for homogeneous conditions of carrier distribution,<sup>15</sup> and for situations in which the carriers are not homogeneous, a numerical solution is required, as mentioned before.<sup>90</sup> The impedance in the homogeneous model has the expression

$$Z(\omega) = \left( \frac{R_{\text{tr}} R_{\text{rec}}}{1 + i\omega/\omega_{\text{rec}}} \right)^{1/2} \coth[(R_{\text{tr}}/R_{\text{rec}})^{1/2}(1+i\omega/\omega_{\text{rec}})^{1/2}] \quad (76)$$

and can be described by a transmission line model as shown in Fig. 16(b).<sup>15,93</sup> In eqn (76)  $R_{\text{tr}}$  is the total transport resistance in the transport channel (while  $r_{\text{HTM}} = 0$ , transport resistance of the hole conductor material, in the other channel), and  $R_{\text{rec}}$  is the recombination resistance across the surface of the nanoporous solid. The transmission line indicated in Fig. 16(b) is more general than eqn (76) as it includes the transport in two channels.<sup>27,93</sup> Furthermore in eqn (76)  $\omega_{\text{rec}}$  is the radian frequency of the charge transfer process,  $\omega_{\text{rec}} = (R_{\text{rec}} C_\mu)^{-1}$ , related to electron lifetime<sup>94</sup> by  $\tau_n = \omega_{\text{rec}}^{-1}$ , as indicated in eqn (41).

We denote  $C_{\text{tot}}$  as the total capacitance in the solid phase and the solid–electrolyte interface.  $C_{\text{tot}}$  has several possible contributions:<sup>69</sup>

- (1) The chemical capacitance of the semiconductor,  $C_\mu$ .
- (2) The depletion capacitance of the semiconductor surface,  $C_{\text{sc}}$ .
- (3) The Helmholtz capacitance of the surface,  $C_{\text{H}}$ .

The total film capacitance in a DSC has an additional contribution from the exposed surface of the substrate of the nanostructured metal-oxide, as discussed later.

The transit time of carriers across the thickness of the active layer is obtained as

$$\tau_d^n = \frac{1}{\omega_d^n} = R_{\text{tr}} C_{\text{tot}} \quad (77)$$

If  $C_{\text{tot}}$  is a chemical capacitance,  $C_\mu$ , then the chemical diffusion coefficient<sup>95</sup> can be calculated by means of eqn (77) with the relation<sup>15,88</sup>

$$D_n = \frac{L^2}{\tau_d^n} = \frac{L^2}{R_{\text{tr}} C_\mu} \quad (78)$$

Characteristic impedance spectra of eqn (76) are shown in Fig. 17. The case, in which the recombination rate is low with respect to the electron transport rate, is given by the condition  $R_{\text{rec}} > R_{\text{tr}}$ <sup>93</sup> or equivalently, transport characteristic time is shorter than recombination time, *i.e.*  $\tau_d^n \ll \tau_n$ . For frequencies higher than  $\omega_d^n$  eqn (76) reduces to:

$$Z = \left( \frac{R_{\text{tr}}}{C_{\text{tot}}} \right)^{1/2} (i\omega)^{-1/2} \quad (79)$$

Eqn (79) is often termed the “Warburg” impedance, appearing as a 1-slope line in the complex impedance plot shown

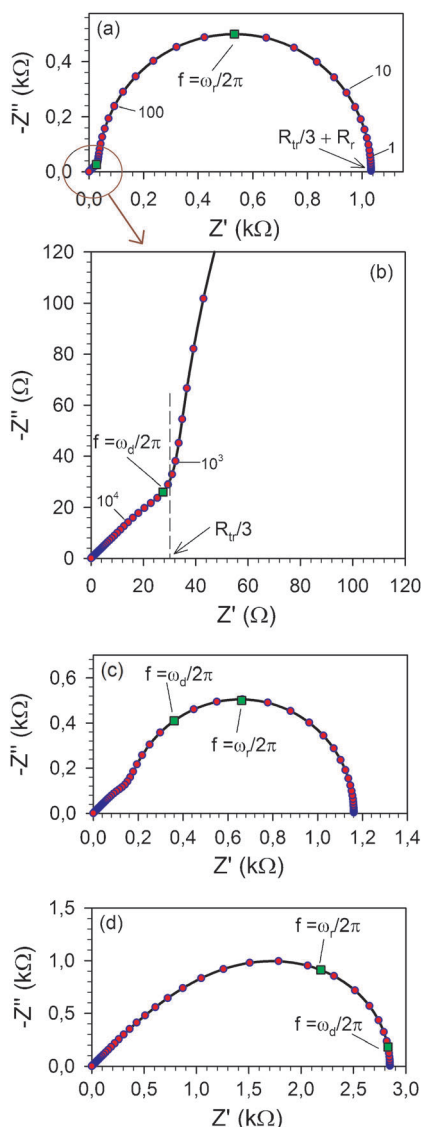


**Fig. 17** Simulation of the diffusion–recombination impedance with reflecting boundary condition at the back contact and  $L_n = 3.1L$ . Parameters  $R_{tr} = 10^2 \Omega \text{ cm}^{-2}$ ,  $R_{rec} = 10^3 \Omega \text{ cm}^{-2}$ ,  $C_\mu = 5 \times 10^{-6} \text{ F cm}^{-2}$ . Shown are the characteristic frequency of the low frequency arc (square point), related to the angular frequency  $\omega_r = \tau_n^{-1} = 1/R_{rec}C_\mu$ , where  $\tau_n$  is the carrier lifetime; the low frequency resistance; and the characteristic frequency of the turnover from Warburg behaviour to low frequency recombination arc (square point), related to the angular frequency  $\omega_{tr} = D_n/L^2 = 1/R_{tr}C_\mu$ , where  $D_n$  is the minority carrier diffusion coefficient.

in the left of Fig. 17(b). It should be emphasized that, in contrast to semi-infinite diffusion, in the transmission line model the  $45^\circ$  characteristic appears only in the high frequency part of the impedance spectrum. As the frequency decreases ( $\omega < \omega_d$ ) the charge-transfer resistance gives rise to a semi-circle at low frequency, consisting of the parallel combination of  $R_{rec}$  and  $C_{tot}$  as shown in Fig. 17(a). The total low frequency resistance for the active layer inferred from eqn (76) is

$$R_{AL} = \frac{1}{3}R_{tr} + R_{rec} \quad (R_{rec} \gg R_{tr}) \quad (80)$$

However, when the recombination flux is large we have the situation  $R_{rec} < R_{tr}$ , and a different spectrum is obtained, see Fig. 17(d). From eqn (76) we obtain the Gerischer impedance,

$$Z = \left( \frac{R_{tr}R_{rec}}{1+i\omega/\omega_{rec}} \right)^{1/2} \quad (81)$$

In the Gerischer impedance  $R_{tr}$  and  $R_{rec}$  cannot be distinguished by inspection, and the active layer resistance is

$$R_{AL} = (R_{tr}R_{rec})^{1/2} \quad (R_{tr} \gg R_{rec}) \quad (82)$$

The collection efficiency of the solar cell is closely related to the shape of the impedance spectra. We note the expression<sup>15,32</sup>

$$L_n = L \sqrt{\frac{R_{rec}}{R_{tr}}} \quad (83)$$

that relates the diffusion length to the recombination and transport resistances.<sup>34</sup> Therefore, the spectrum in Fig. 17(a) indicates the solar cell in which the diffusion length is many times larger than the thickness of the layer, hence with a high collection efficiency, while the observation of the Gerischer impedance indicates strong recombination and low collection efficiency.

The effect of diffusion of the redox species in the electrolyte is described by<sup>96,97</sup>

$$Z_d = R_d \frac{\tanh[(j\omega/\omega_d^p)^{1/2}]}{(j\omega/\omega_d^p)^{1/2}} \quad (84)$$

where  $R_d$  is the diffusion resistance of ions (holes) in the electrolyte and  $\omega_d^p$  the characteristic frequency of diffusion, related to the diffusion coefficient of the ions through  $D_p = l^2\omega_d^p$ , with  $l$  being the effective diffusion length ( $l = L/2$ ).

### 3.7 Reconstruction of current–voltage curves from the resistances

We have explained above the derivation of the recombination resistance from the diode characteristic in the  $\beta$ -recombination model. This model is very useful as a first approximation to IS measurements of DSC and is obeyed in many cases. However, the recombination resistance may show more complex features, such as a curvature<sup>98</sup> and even peaks and valleys.<sup>99–101</sup> In addition, the steady state performance of DSCs is also influenced by other resistive contributions associated to contacts, transport, etc. Therefore, in general it is important to determine a procedure whereby the  $jV$  curve is obtained from the measured resistances (as a function of voltage), so that each factor determining the performance of the solar cell can be separately treated.

We describe the method to obtain the  $jV$  curve of a DSC from the IS data.<sup>97</sup> First we consider the total resistance obtained from impedance  $R_{dc}$ . Note that in a real device  $R_{dc}$  has two contributions: one arising from the active layer,  $R_{AL}$ , that corresponds to the transmission line (eqn (80) and (82) depending on the impedance pattern), and the other one arising from the other elements connected to the active layer (contacts, electrolyte, counterelectrode) that introduces a series resistance  $R_{series}$ . Then,

$$R_{dc} = R_{series} + R_{rec} + \frac{1}{3}R_{tr} \quad (R_{rec} \gg R_{tr}) \quad (85)$$

$$R_{dc} = R_{series} + (R_{tr}R_{rec})^{1/2} \quad (R_{tr} \gg R_{rec}) \quad (86)$$

depending on the relation between  $R_{\text{tr}}$  and  $R_{\text{rec}}$ , as it has been explained in the previous section.

$R_{\text{rec}}$  accounts for the overall recombination resistance associated with the charge losses in the cell.  $R_{\text{rec}}$  has two main contributions in parallel, the charge transfer resistance from the back layer (see below),  $R_{\text{BL}}$ , and from the  $\text{TiO}_2$  nanoparticles surface,  $R_{\text{rec,np}}$ .

$$R_{\text{rec}} = R_{\text{BL}} || R_{\text{rec,np}} \quad (87)$$

$R_{\text{series}}$  accounts for the series resistance that is related to the sum of all the resistances that produce a loss in the electrochemical potential of the cell outside the active layer, which are

$$R_{\text{series}} = R_S + R_{\text{CE}} + R_d \quad (88)$$

Here  $R_S$  is the series resistance due to contributions from wires, collecting electrodes and contacts,  $R_{\text{CE}}$  is the charge transfer resistance at the counterelectrode, and  $R_d$  is the diffusion resistance in the electrolyte. As indicated in Fig. 2(a), the reciprocal of  $R_{\text{dc}}$  is defined as the slope of the  $jV$  curve, thus (see also eqn (24))

$$R_{\text{dc}}^{-1} = \frac{1}{A} \frac{\text{d}j}{\text{d}V} \quad (89)$$

Rearranging this equation and with an integration over the voltage, we obtain the current crossing the cell as a function of the voltage

$$j = j_{\text{sc}} - A \int_0^{V_{\text{app}}} \frac{\text{d}V}{R_{\text{dc}}} \quad (90)$$

The analysis of the resistance values obtained from the impedance is a key step to understand the origin of the limitations in the performance of the DSC. Once the injection determines the maximum current attainable, recombination resistance determines the open circuit voltage and maximum attainable efficiency, while the series resistance will reduce this maximum by decreasing the fill factor.

In a simplified approach as that adopted in eqn (12), the transport resistance term  $R_{\text{tr}}/3$  that appears in eqn (85) can also be included in  $R_{\text{series}}$  to account for the reduction of useful voltage.

#### 4. General features of the IS of dye-sensitized solar cells

Dye-sensitized solar cells (DSCs) based on mesoporous titania and liquid electrolytes are a promising device for solar energy harvesting.<sup>102</sup> Upon illumination, the sensitizer is excited by absorption of a photon and injects an electron into the conduction band of the semiconductor. Electron transport through the titanium oxide framework can be described with a trapping/detrapping model, where an electron moves *via* conduction band transport states from trap to trap until its collection at the transparent conducting oxide (TCO).<sup>86</sup> The electrolyte or solid hole conductor transports the hole remaining in the oxidized dye to the cathode. At present there are many efforts to improve the performance,<sup>1</sup> e.g., by design of ordered semiconductor architectures,<sup>103</sup> new Ru-based dyes with a wider absorption range<sup>104</sup> and metal-free dyes.<sup>105–107</sup>

There are also across the world several initiatives for large scale production of DSC. The progress in these areas depends upon the availability of accurate tools that may describe the processes controlling the behavior of the device. IS is particularly well suited for the study of charge accumulation, transport and recombination under the different operating conditions of DSC, as well as to make a general assessment of device electrical properties.

In this section we will describe the characteristic impedance spectra obtained under different measurement conditions of illumination or applied voltage and the models used to study them. The typical behavior of the resistances and capacitances that describe the IS will be explained and related with the theoretical models introduced above. Finally it will be analyzed the influence of these parameters on the performance of the DSC.

#### 4.1 Impedance spectra of DSC

Fig. 18 shows examples of the most characteristic patterns of the impedance spectra that are usually found for the DSC and the equivalent circuits required to fit them. In all the cases, experimental data are plotted as dots while the fits to the model are plotted as lines. Parameters from the fits are included in Table S1 of ESI.†

In Fig. 18(a), the IS spectrum is plotted at an intermediate voltage (0.4 V) and in Fig. 18(b) at an open circuit (here at 0.65 V), for a DSC with an ionic liquid as an electrolyte under 50 mW cm<sup>-2</sup> power illumination.

In the case of 0.4 V, the high frequency limit of the spectrum shows the Warburg impedance (see the inset), followed by a recombination arc, in the middle frequency region, which is the typical transmission line pattern characterized by  $R_{\text{tr}}$ ,  $R_{\text{rec}}$  and  $C_{\mu}$  as described above and shown in Fig. 17(a).

The low frequency feature observed in the impedance spectrum of Fig. 18(a) is due to diffusion in the electrolyte as described by eqn (84). At this voltage the characteristic shape of the diffusion impedance (for diffusion in electrolyte) may not be observed due to the overlap with the recombination arc.

Fig. 18(c) shows the IS spectrum obtained for a low performance DSC under 100 mW cm<sup>-2</sup> illumination. The plot follows the trend of Fig. 17(d) indicating that the low efficiency (2%) of the cell is caused by high recombination ( $R_{\text{tr}} > R_{\text{rec}}$ ). As mentioned above, the observation of a spectrum with the shape of Fig. 17(d) and 18(c) will indicate strong recombination and consequently, according to eqn (83), diffusion lengths smaller than the active film thickness. On the contrary, the shapes of Fig. 17(a) and 18(a) indicate that the film is able to extract efficiently the charge injected from the dye as  $L_n > L$ .

Fig. 18(d) represents the complete transmission line model that may be used to fit the impedance of Fig. 18(a) and (c).<sup>16,21,97</sup> The model includes the effect of the counter electrode/electrolyte interface, described by the parallel combination of the charge-transfer resistance,  $R_{\text{Pt}}$ , and the interfacial Helmholtz capacitance,  $C_{\text{Pt}}$ . We have used the suffix Pt to stress the fact that platinum coated counterelectrode is the most employed for DSCs. The model also contains  $R_{\text{BL}}$  and  $C_{\text{BL}}$  elements for the recombination through the substrate uncovered by the colloids of  $\text{TiO}_2$  (or back layer).

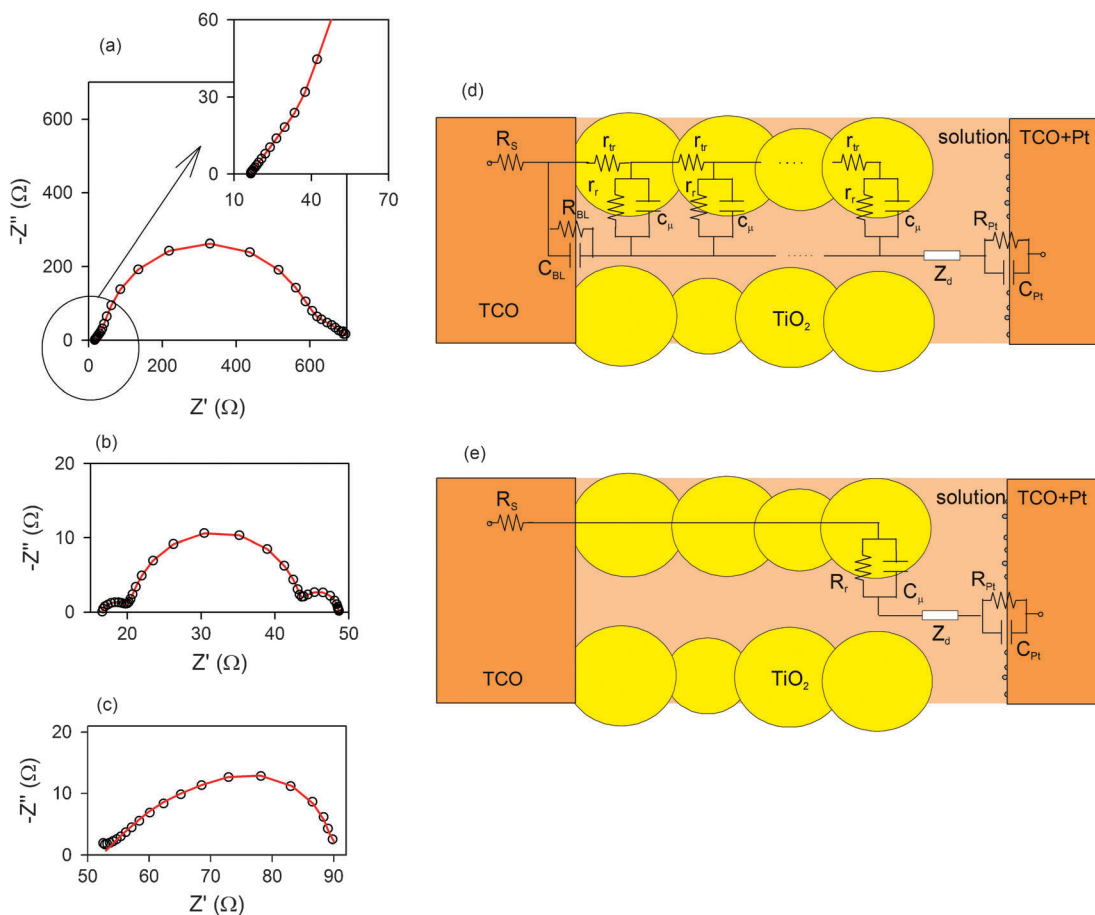


**Fig. 18** Experimental impedance spectra of a DSC with an ionic liquid based electrolyte under  $50 \text{ mW cm}^{-2}$  illumination at (a)  $0.40 \text{ V}$  and at (b) open circuit conditions,  $0.65 \text{ V}$ . (c) The Gerischer impedance spectra appearing in a defective cell, with presenting lower values of recombination resistance than transport resistance. Data are taken at  $0.45 \text{ V}$  under  $100 \text{ mW cm}^{-2}$  illumination. (d) The complete equivalent circuit model to fit experimental data of (a) and (c). (e) Simplified equivalent circuit model that is valid for the spectra measured at high voltage as in (b). In (a) to (c) experimental data are represented by dots and fits to models (c) and (d) are represented by lines.

At high voltages, and in particular at the open circuit voltage, the impedance spectrum usually shows the pattern indicated in Fig. 18(b). The high frequency arc is due to the counter-electrode charge transfer resistance and the associated  $C_{\text{Pt}}$ . The second arc is due to the recombination resistance at the  $\text{TiO}_2$ /electrolyte interface and the chemical capacitance of the  $\text{TiO}_2$ . The low frequency arc is due to the impedance of diffusion in the electrolyte. The width of each of these arcs corresponds to  $R_{\text{Pt}}$ ,  $R_{\text{rec}}$  and  $R_d$ , respectively, while the initial displacement of the arcs from the origin corresponds to the contribution from the FTO resistance  $R_s$ .

At these voltages the effect of the back layer is negligible. The Fermi level of electrons approaches the conduction band of  $\text{TiO}_2$  and a very high concentration of electrons is present in the semiconductor. As a consequence, the resistance of  $\text{TiO}_2$  becomes negligible,  $R_{\text{tr}} \approx 0$ , which reduces the complexity of the impedance spectrum. The equivalent circuit of Fig. 18(d) can then be simplified as shown in Fig. 18(e), with the transmission line reduced to a simple  $R-C$  parallel combination, which is the model shown in Fig. 8(c).

It has to be noted that the term  $Z_d$  includes the diffusion of the electrolyte both in a porous matrix and in the bulk of the electrolyte layer between the  $\text{TiO}_2$  film and the counterelectrode.

As for most electrolytes,  $\omega_d^{\text{P}} \ll \omega_{\text{rec}}$ , it is possible to decouple the IS response of diffusion both from the semiconductor and the counterelectrode responses, avoiding the use of Randles like equivalent circuits<sup>84</sup> or more complex transmission lines,<sup>27,93</sup> as the one proposed in Fig. 16(b). In good electrolytes,  $R_d$  may reach small enough values so that the third arc becomes negligible.

#### 4.2 The recombination resistance

The behavior of the overall recombination resistance  $R_{\text{rec}}$  usually follows the trends shown in Fig. 19(a). At low voltages, charge transfer from the back layer dominates. The back layer may have different responses depending on the treatments received: precoating with sputtered layers of dense  $\text{TiO}_2$ ,  $\text{TiCl}_4$  treatments, polymeric coatings after film formation, etc.<sup>108,109</sup> The slope of  $R_{\text{BL}}$ , generally small, is a function of both the presence of coatings and electrolyte composition. At higher voltages the dominant mechanism of charge recombination in the DSC is the recombination of the electrons from the  $\text{TiO}_2$  large surface to the electrolyte. In the case presented here, the recombination follows the linear trend as described by eqn (42),<sup>21,32,72</sup> with characteristic parameters  $\beta = 0.47$  and  $j_0 = 3.8 \times 10^{-5} \text{ mA cm}^{-2}$ .

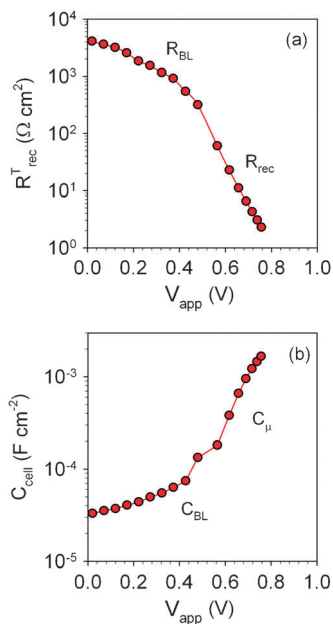


**Fig. 19** Recombination resistance (a) and cell capacitance (b) of a DSC with an acetonitrile-based electrolyte. At low voltages the measured values are dominated by the characteristics of the back layer at the bottom of the  $\text{TiO}_2$  film ( $R_{\text{BL}}$  and  $C_{\text{BL}}$ ). At voltages above 0.4 V, recombination through the porous film and chemical capacitance of  $\text{TiO}_2$  dominate the measured parameters.

#### 4.3 The capacitance

The behaviour of the capacitance in a DSC in a characteristic measurement is shown in Fig. 19(b). At low voltages the dominant capacitance is the combination of the capacitances at the contacts: the counterelectrode, and the exposed surface of the conducting substrate where the nanoporous  $\text{TiO}_2$  is deposited (either if the substrate is coated with a thin insulating layer or not).<sup>16,21,77,97</sup> Additional contributions may appear due to  $\text{TiO}_2/\text{TCO}$  contacts or residual charge accumulated in the initial layers of  $\text{TiO}_2$  colloids.<sup>77,103</sup>

At high voltages, the dominant capacitance is the chemical capacitance of  $\text{TiO}_2$ , which shows a characteristic exponential variation with the voltage. Eventually, at very high voltages, the capacitance of the DSC may tend to reach the surface Helmholtz capacitance of the  $\text{TiO}_2/\text{electrolyte}$  interface,  $C_H$ . This would lead to a saturation in the capacitance value.<sup>71</sup>

As mentioned before, the chemical capacitance describes the density of states in the bandgap. Fig. 19(b) reveals the shape of the DOS, which is an exponential trap distribution below the conduction band of the nanostructured  $\text{TiO}_2$ , compare Fig. 11(c).<sup>69,71</sup>

Quite frequently, in between the two main regimes, there appears a small peak in the capacitance which is attributed to a localized surface state in the  $\text{TiO}_2$ . If these surface states are blocked (*i.e.* by a coating) their contribution to recombination is small, but in some cases they may produce a pronounced valley in the recombination resistance,<sup>71,110</sup> and this is often the case in aqueous electrolytes.<sup>100</sup>

Another effect that is found often at low frequencies is a negative capacitance contribution that makes the impedance

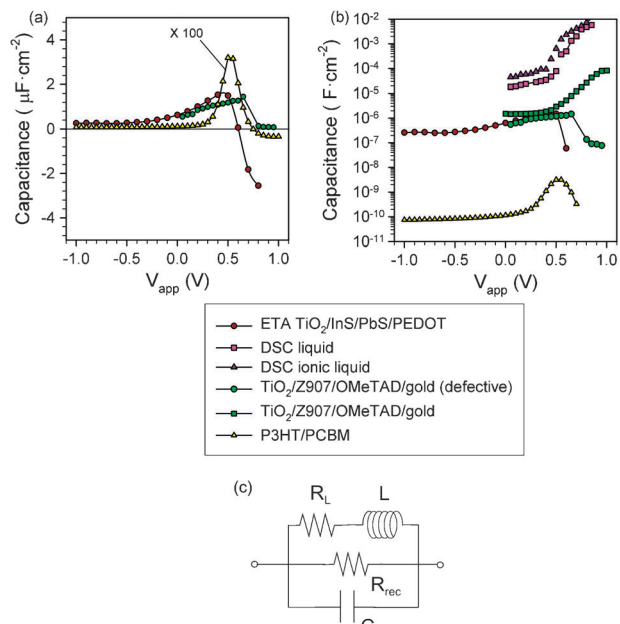


**Fig. 20** (a) Characteristic results of solar cells showing negative capacitance at a forward (negative) bias: extremely thin absorber (ETA) cell based on rough  $\text{TiO}_2$ , dye-sensitized solar cell (defective) with solid OMeTAD hole conductor, and normal P3HT/PCBM bulk heterojunction organic solar cell. (b) Same data as in (a) in logarithmic scale, including the standard (positive) chemical capacitance of two dye-sensitized solar cells (nanostructured  $\text{TiO}_2/\text{N}719/\text{iodide}$  electrolyte) with both liquid and viscous electrolyte, and a regular DSC with OMeTAD hole conductor. (c) Model used to fit negative capacitance.<sup>111</sup>

spectrum to enter the fourth quadrant.<sup>111</sup> The negative capacitance sometimes complicates the interpretation of resistances.<sup>112</sup>

Fig. 20(a) and (b) show the characteristic features of negative capacitance observed at a forward bias in some types of nanostructured solar cells.<sup>111,113</sup> The negative capacitance decreases the charge accumulation ability of the solar cell, reducing its performance.<sup>111</sup> Fig. 20(c) shows an equivalent circuit that can be employed to fit the negative capacitance, even though the physical meaning of the inductor is not straightforward.<sup>113</sup>

#### 4.4 The series resistance

The different contributions to the series resistance in the measurement of a DSC are plotted in Fig. 21(a). The figures reveal that the greater contribution to  $R_{\text{series}}$  has its origin in the conductive glass, which is twice larger than the values of diffusion and counter electrode resistances. Note that the transport resistance term  $R_{\text{tr}}/3$  that appears in eqn (85) can also be included in  $R_{\text{series}}$  to account for the reduction of useful voltage, as it has been previously commented. At the laboratory level, the presence of relatively high series resistances in small area cells ( $R_{\text{series}} \approx 14$  to  $23 \Omega$  for this  $0.23 \text{ cm}^2$  cell) does not represent a major shortcoming since the current passing through the cell is small, and therefore the potential drop associated to  $R_{\text{series}}$  will not be large. However in order to build large current panels a major effort is needed to diminish this resistance as competitor technologies have succeeded in obtaining  $R_{\text{series}} < 0.5 \Omega \text{ cm}^2$ .

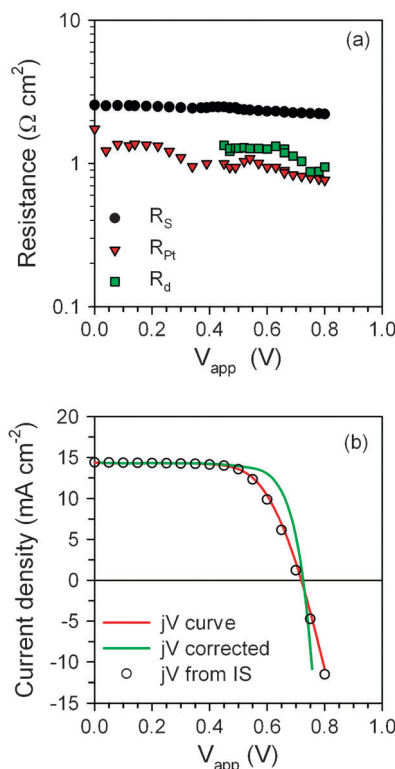


**Fig. 21** (a) The separate contributions to the total series resistance obtained by impedance spectroscopy at the different voltages in an acetonitrile based DSC under 1 sun illumination. (b) The measured current–voltage curve (red line) obtained for the same cell and measurement conditions. The  $jV$  curve is characterized by parameters  $V_{\text{oc}} = 0.73$ ,  $j_{\text{sc}} = 14.4 \text{ mA cm}^{-2}$ , FF = 0.66,  $\eta = 6.9\%$ . Green line shows the simulated  $jV$  curve after removing the series resistance effect. After the correction it is obtained FF = 0.74 and  $\eta = 7.7\%$ . The void circles show the values obtained by integration of resistances measured by IS.

#### 4.5 The $jV$ curve

As explained before, using integration procedures, eqn (90), it is possible to analyze the components of the current–voltage curve of a DSC. In Fig. 21(b) it can be observed a good match between the  $jV$  curve obtained for a DSC with liquid electrolyte (line) and the curve generated through eqn (90) (dots). In this case the moderate fill factor found (0.66) is due to the relatively high values of the series resistance as described above.

To obtain the potential drop in the  $\text{TiO}_2$  film, the active layer, corrected from the series resistance, it is possible to use the integral expression<sup>97</sup>

$$V_F = V_0 + \int_{j_{\text{sc}}}^j R_{\text{AL}} \, dj \quad (91)$$

the resistance of the active layer  $R_{\text{AL}}$  depends on the impedance of the transmission line, *i.e.* the relation between  $R_{\text{tr}}$  and  $R_{\text{rec}}$ , see eqn (80) and (82). Note that for good performing solar cells, especially under illumination,  $R_{\text{rec}} \gg R_{\text{tr}}$  then  $R_{\text{AL}} \approx R_{\text{rec}}$ .  $V_0$  is the potential drop at the series resistance at short circuit conditions.  $V_0$  represents the electrochemical potential difference between the photoactive film and the contacts

at short circuit (when the applied voltage to the DSC is fixed to zero).<sup>84</sup> Note that at  $V_{\text{oc}}$

$$V_0 = V_{\text{oc}} - \int_{j_{\text{sc}}}^0 R_{\text{AL}} \, dj \quad (92)$$

Thus the parameters  $V_{\text{oc}}$ ,  $j_{\text{sc}}$  and the variable  $R_{\text{AL}}$  are the elements that determine the  $jV$  curve with the maximum efficiency attainable by the cell, which further on will be called internal  $jV$  curves and efficiency.

The internal  $jV$  curve of the sample provided after obtaining the corrected voltage ( $V_F$ ) is plotted in Fig. 21(b). It provides a 12% increase in the efficiency of the cell to a 7.7% through the improvement of the FF to a value 0.74.

These data show the importance of optimizing the design of the DSC to minimize the series resistance contribution, specially in the high efficiency and large area cells where the currents are large and therefore, in which the effect of series resistance is more important.

#### 4.6 Comparison of IS parameters of a set of DSCs

For a collection of samples it is important to identify which are the factors that determine the differences in their efficiencies, concerning the open-circuit voltage, short-circuit current and fill factor. As described previously,  $j_{\text{sc}}$  is determined by the absorption of the dye and the internal quantum yield, while the shape of the  $jV$  curve depends on a combination of factors that can be identified with the analysis of IS parameters. We report here the summary of the analysis of a number of DSC devices using different dyes, electrolytes and  $\text{TiO}_2$  pastes. The characteristics of these solar cells are given in Table 3, the impedance parameters are shown in Fig. 22, and selected  $jV$  curves are shown in Fig. 23. The main features observed are the following.

**4.6.1 The total series resistance of the cell.** Fig. 21(a) shows the different contributions to series resistance. The conducting glass substrate and counterelectrode charge transfers are determined externally by the choice of the appropriate geometry of the cell, the sheet resistance of the conductive glass or the amount and area of the catalyst at the counter and remain nearly constant. With the appropriate protocols, these elements may be standardized to obtain cells with the same values of  $R_S$  and  $R_{\text{Pt}}$ .

The contribution of the diffusion resistance depends on factors such as the electrolyte composition, the type of hole conductor, the size of the pores and the current crossing the cell. This last dependence produces a diffusion resistance that changes upon the applied voltage.

From Table 3 we observe that although the absolute value of the average series resistance is quite similar for all the samples, the normalized series resistance (in  $\Omega \text{ cm}^2$ ) differs largely as the active area of each sample is quite different. The greater the normalized resistance, the larger the difference between measured FF and efficiency and their internal values. This difference peaks for samples such as N719a and N719b that have large values of  $j_{\text{sc}}$ , as the potential drop at the series resistance is larger.

**Table 3** Experimental parameters obtained from the fits and characteristics of samples shown in Fig. 22. Internal FF and  $\eta$  are the values obtained after subtracting the potential drop at the series resistance and the calculated FF is the value obtained from eqn (27). The short name of the dyes refer to the following: K19 is Ru-(4,4'-dicarboxylic acid-2,2'-bipyridine)(4,4'-bis(*p*-hexyloxystyryl)-2,2'-bipyridine)(NCS)<sub>2</sub> and it was coadsorbed with phenylpropionic acid (PPA); N719 is *cis*-di(thiocyanato)-*N,N'*-bis(2,2'-bipyridyl-4-carboxylic acid-4'-tetrabutylammonium carboxylate) ruthenium(II); ZnPc is 2,3-dicarboxyanhydride-9,10,16,17,23,24-[4'-(1',1',3",3"-tetramethylbutyl)phenoxy] phthalocyanine; BG1, 3,6-di-*tert*-butyl-9H-carbazole; BG2 3,6-di-*tert*-butyl-9-(4-iodophenyl)-9H-carbazole. The short name of the electrolytes stand for: Z380 is *N*-methylbenzimidazole 0.5 M, guanidinium thiocyanate 0.12 M and iodine (I<sub>2</sub>) 0.2 M in a mixture of 1-methyl-3-propylimidazolium iodide & 1-methyl-3-ethylimidazolium thiocyanate, 65% : 35% volume ratio; Z300 is 0.60 M butylmethyliimidazolium iodide, 0.03 M I<sub>2</sub>, 0.10 M guanidinium thiocyanate and 0.50 M 4-*tert*-butylpyridine in a mixture of acetonitrile and valeronitrile, 85% : 15% volume ratio; Z325 is 0.6 M methylpropylimidazolium iodide, 0.5 M *tert*-butylpyridine, and 0.03 M I<sub>2</sub> in a mixture of acetonitrile and valeronitrile, 75% : 25% volume ratio; E100 is 0.7 M LiI and 0.05 M I<sub>2</sub> in 3-methoxypropionitrile; E105 is 0.5 M LiI and 0.05 M I<sub>2</sub> in 3-methoxypropionitrile

| Sample name               | K19                  | N719a                | N719b                | N719c                | ZnPc                 | H <sub>2</sub> Pc     | BG1                  | BG2                  |
|---------------------------|----------------------|----------------------|----------------------|----------------------|----------------------|-----------------------|----------------------|----------------------|
| $V_{oc}/V$                | 0.68                 | 0.80                 | 0.73                 | 0.45                 | 0.44                 | 0.35                  | 0.45                 | 0.39                 |
| $j_{sc}/mA\ cm^{-2}$      | 14.00                | 17.96                | 18.80                | 10.90                | 3.48                 | 5.71                  | 8.22                 | 10.40                |
| FF                        | 0.71                 | 0.74                 | 0.61                 | 0.50                 | 0.66                 | 0.57                  | 0.58                 | 0.54                 |
| $\eta/(\%)$               | 7.00                 | 10.53                | 8.43                 | 2.50                 | 1.01                 | 1.14                  | 2.14                 | 2.18                 |
| Internal FF               | 0.82                 | 0.82                 | 0.80                 | 0.71                 | 0.68                 | 0.65                  | 0.67                 | 0.67                 |
| Calculated FF             | 0.81                 | 0.82                 | 0.79                 | 0.71                 | 0.63                 | 0.56                  | 0.67                 | 0.67                 |
| Internal $\eta$ (%)       | 7.70                 | 11.58                | 10.96                | 3.47                 | 1.04                 | 1.21                  | 2.47                 | 2.73                 |
| $\beta$                   | 0.78                 | 0.69                 | 0.62                 | 0.64                 | 0.44                 | 0.40                  | 0.50                 | 0.60                 |
| $j_0/mA\ cm^{-2}$         | $1.7 \times 10^{-8}$ | $1.0 \times 10^{-8}$ | $4.8 \times 10^{-7}$ | $1.6 \times 10^{-4}$ | $2.0 \times 10^{-3}$ | $25.5 \times 10^{-3}$ | $1.3 \times 10^{-3}$ | $1.2 \times 10^{-3}$ |
| $j_{0k}/mA\ cm^{-2}$      | 604                  | 230                  | 11 164               | 8363                 | 980                  | 68                    | 3928                 | 21 417               |
| $\alpha$                  | 0.51                 | 0.45                 | 0.26                 | 0.47                 | 0.34                 | 0.40                  | 0.41                 | 0.41                 |
| $E_c - E_{F0}/eV$         | 1.00                 | 1.06                 | 0.99                 | 0.66                 | 0.78                 | 0.68                  | 0.77                 | 0.74                 |
| $-\Delta E_c/V$           | 0.06                 | Ref                  | 0.08                 | 0.40                 | 0.28                 | 0.38                  | 0.29                 | 0.32                 |
| Avg. $R_{series}/\Omega$  | 29                   | 23                   | 23                   | 27                   | 17                   | 19                    | 20                   | 25                   |
| $R_{series}/\Omega\ cm^2$ | 8.12                 | 2.94                 | 6.44                 | 11.61                | 5.61                 | 6.84                  | 5.50                 | 6.25                 |
| Area/cm <sup>2</sup>      | 0.28                 | 0.13                 | 0.28                 | 0.43                 | 0.33                 | 0.36                  | 0.28                 | 0.25                 |
| $L/\mu m$                 | 10.80                | 14.00                | 10.80                | 10.00                | 10.00                | 10.00                 | 10.00                | 10.00                |
| Porosity                  | 0.68                 | 0.68                 | 0.68                 | 0.50                 | 0.50                 | 0.50                  | 0.50                 | 0.50                 |
| $T/K$                     | 300                  | 300                  | 300                  | 300                  | 300                  | 300                   | 300                  | 300                  |
| Electrolyte               | Z380                 | Z300                 | Z325                 | E100                 | E100                 | E100                  | E105                 | E105                 |
| Dye                       | K19                  | N719                 | N719                 | N719                 | ZnPc                 | H <sub>2</sub> Pc     | BG1                  | BG2                  |

**4.6.2 The position of the conduction band of the semiconductor with respect to the redox of the hole conductor.** The shifts observed in the  $C_\mu$  plotted in Fig. 22(a) indicate a displacement in the conduction band. Therefore, the higher the  $E_c$  the larger the displacement of the capacitance towards positive potentials. These shifts have their origin in different dyes, electrolytes and TiO<sub>2</sub> pastes used to build the samples. Making the assumption that the  $N_c$  is the same for all the TiO<sub>2</sub> samples it is possible to estimate the  $\Delta E_c$  through eqn (43). If the values of  $\alpha$  are similar, this  $\Delta E_c$  is simply the displacement of the capacitance normalized to the volume. Taking one sample as reference (Ref), the capacitances of the other samples are shifted until they overlap, see Fig. 22(b). This shift removes the effect of the different conduction band positions, plotting the capacitance vs.  $V_{ecb}$ , the common equivalent conduction band potential, as explained in Section 3.3. In Fig. 22 sample N719a has been used as a reference sample. The approximate value of the position of  $E_c$  has been estimated using  $N_L = 2 \times 10^{20} \text{ cm}^{-3}$ ,<sup>62</sup> see Table 3.

In terms of the performance, for samples with similar photocurrents, a raise in the conduction band produces an increase in the  $V_{oc}$ , see Table 3.

Note that the difference in the composition of the different samples shown in Fig. 22 also produces a change in the value  $\alpha$  which indicates differences in the distribution of subbandgap states in the TiO<sub>2</sub>, see the slope of Fig. 22(b).

**4.6.3 The recombination resistance.** Variations in  $E_c$  also affect the recombination resistance values. A raise in  $E_c$  increases

the value of  $j_0$ , as indicated in eqn (21), which decreases  $R_{rec}$ , as given by eqn (42), and this can be seen in Fig. 22(c). As a consequence  $R_{rec}$  is also shifted depending on the  $E_c$  position, see Fig. 22(c). The effects on  $R_{rec}$  are key in the performance of the cell. It was already pointed out in previous sections that for a given  $j_{sc}$  the lower absolute values of  $R_{rec}$  and  $\beta$  determine, respectively, a lower  $V_{oc}$  and internal FF. In practice the different cells provide variations in  $j_{sc}$ , therefore small modifications are expected to occur. For the same  $R_{rec}$  increasing current provides higher  $V_{oc}$  and, according to eqn (27), larger internal FF.

In order to remove the effect of the  $E_c$  position, as in the case of  $C_\mu$ ,  $R_{rec}$  has to be plotted vs.  $V_{ecb}$ , see Fig. 22(d) and (e), applying exactly the same shift as the one applied for the chemical capacitance. We have split the plots of  $R_{rec}$  vs.  $V_{ecb}$  for clarity reasons. The representation vs.  $V_{ecb}$  allows us to analyze the cell performance in terms of recombination. In Fig. 22(d) the samples, from Table 3, with the highest  $\beta$  have been plotted. Sample N719a presents the highest recombination resistance (lower recombination), and in consequence it presents the highest  $V_{oc}$ , see Table 3. Note that in terms of the diode model sample N719a presents the lowest  $j_{0k}$ . Comparing samples N719, among them the added effect of lower recombination, higher  $\beta$  and higher conduction band makes the cell N719a the highest performing cell. In addition, in the case of the internal FF the values obtained have an excellent agreement with eqn (27), see calculated FF in Table 3, using the practical  $\beta$  and  $V_{oc}$  obtained for the different samples. The changes in the actual FF obtained from the cell and

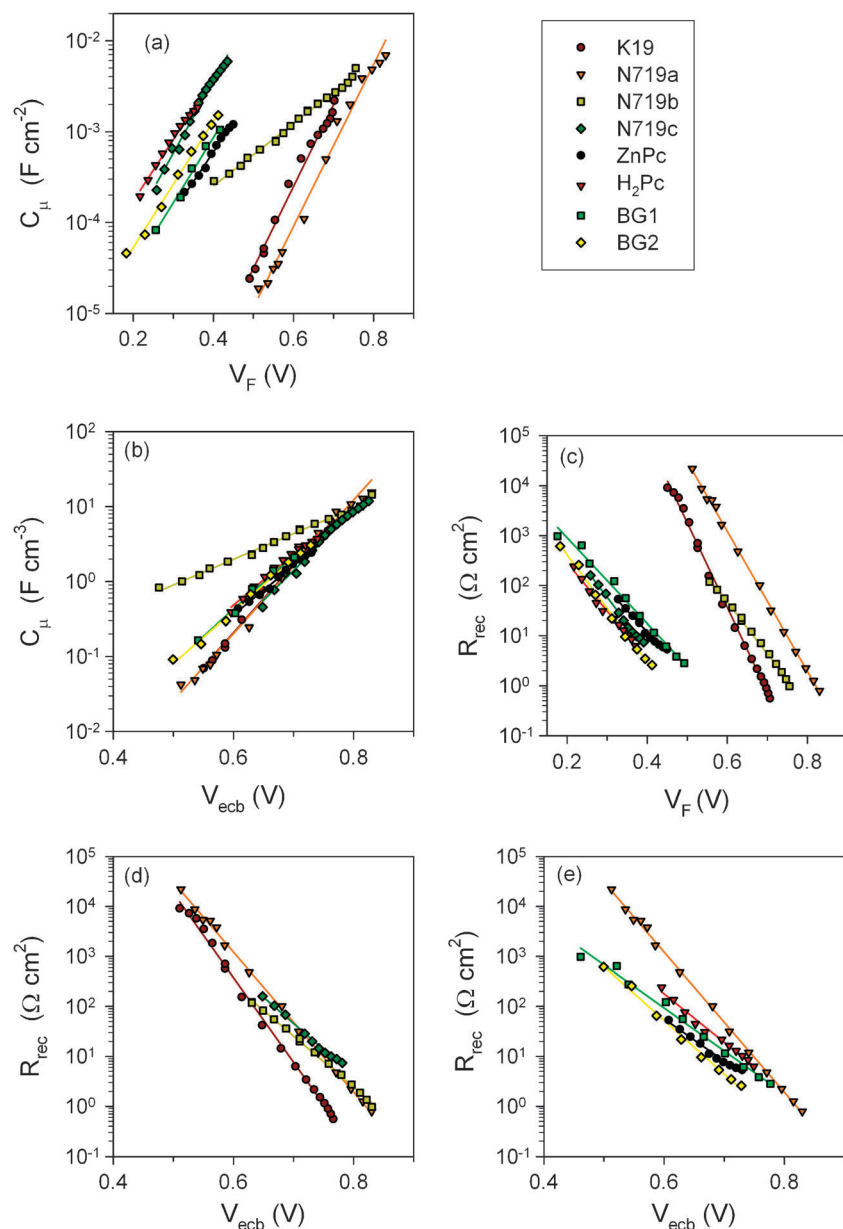


**Fig. 22** Chemical capacitance (a) and recombination resistance (c) of a collection of DSCs with different dyes and electrolytes as described in Table 3, plotted against  $V_F$ . The effect of different conduction band positions has been removed by plotting the chemical capacitance (b) and recombination resistance, (d) and (e), vs.  $V_{\text{ecb}}$ .

the corresponding reduction in efficiency are thus attributable exclusively to the effect of  $R_{\text{series}}$ .

In Fig. 22(e) the cells, from Table 3, with the lowest  $\beta$  and the reference cell N719a are represented. Again the sample with the lowest  $j_{0k}$ , H<sub>2</sub>Pc, presents the highest recombination resistance. However, H<sub>2</sub>Pc presents the lowest  $\beta$ , suggesting that finally this cell presents the highest  $j_0$  and consequently the highest recombination. See for comparison in Table 3 that cell N719a presents the lowest  $j_0$ . In this sense the recombination can be easily evaluated in terms of  $j_{0k}$  and  $\beta$ , if the effect of the conduction band is removed. It is interesting to point out that for samples ZnPc and H<sub>2</sub>Pc there is a discrepancy between the internal FF and the calculated FF, which means that the

reduced FF observed in these cells is not due exclusively to the effect of series resistance, and other effects are contributing to this FF reduction.

Note that the representation plotted in Fig. 22 of  $C_\mu$  and  $R_{\text{rec}}$  vs.  $V_F$  and  $V_{\text{ecb}}$ , and the  $j_{\text{sc}}$  obtained from  $jV$  curves, permits a proper characterization of DSCs in terms of photocurrent, conduction band and recombination, allowing us to determine the main limiting factors in the cell performance. There are many examples in the literature of the use of IS for comparing different cells, but using only one applied voltage data point. It is important to remark that this analysis cannot discriminate the origin of differences observed between samples, revealing whether a change in the position of

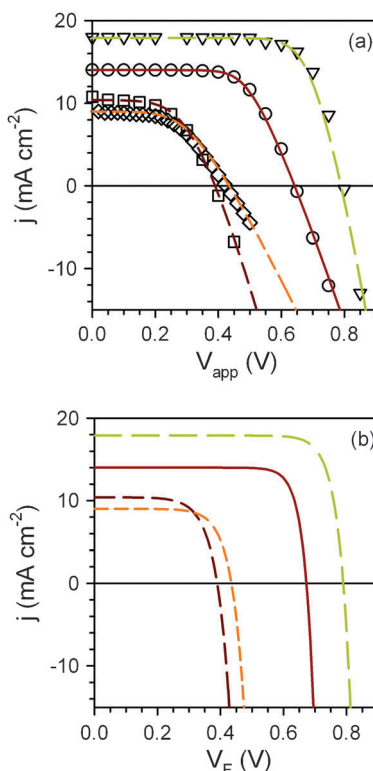


**Fig. 23** (a) Experimental  $jV$  curves (dots) and regenerated  $jV$  curves obtained from impedance data (lines) for a collection of samples from Table 3. (b) Internal  $jV$  curves for the same samples.

the band or different recombination took place. Impedance analysis at varying applied voltage is required to determine the shift in conduction band, by the displacement observed in  $C_\mu$ . In addition, this analysis, sweeping different forward applied voltages, allows to calculate the  $\beta$  parameter and compare properly  $R_{rec}$ , in order to evaluate the recombination term.

In Fig. 23 the  $jV$  curves of a collection of samples from Table 3 are plotted. Experimental  $jV$  curves are represented as dots while the lines represent the  $jV$  curves obtained from the parameters given in Table 3 and eqn (90), see Fig. 23(a). In Fig. 23(b) the internal  $jV$  curves, removing series resistance effect, are plotted.

## 5. Materials and processes in dye-sensitized solar cells

### 5.1 Energetics

As we have just seen, the use of different dyes and electrolytes and also the preparation procedure of the  $TiO_2$  may produce displacements in the conduction band position that affect the overall performance of the cell. Drawing the energy position of  $E_c$  together with the position of the LUMO and the HOMO of the dye and the redox of the electrolyte and considering the energetic distribution of these levels is a helpful tool in the description and interpretation of some of the main limitations of the solar cells.<sup>3,62,114</sup> A detailed view and analysis of the dye excited state and dye regeneration are provided in the work of Meyer and coworkers.<sup>115–117</sup>

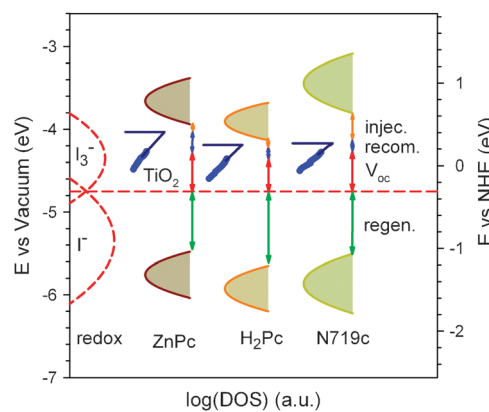


**Fig. 24** Energy diagrams of the active components in some DSC samples prepared with the same electrolyte, E100 (0.7 M LiI and 0.05 M  $I_3^-$  in 3-methoxypropionitrile), and different dyes, ZnPc,  $H_2Pc$  and N719. To represent acceptor and donor states of the  $I_3^-/I^-$  redox couple (dashed line), it has been taken a reorganization energy of 0.5 eV. For the HOMO and LUMO states of the dyes it has been considered the effect of absorption and solvation (continuous lines). The density of electron states below the conduction band of the  $TiO_2$  has been obtained from capacitance measurements (dots). The shape of the DOS has been estimated, also from the values of capacitance, up to the conduction band (blue line).

In Fig. 24 it has been plotted this detailed energetic diagram for several samples using the same  $TiO_2$  paste, electrolyte and different dyes, Zn phthalocyanine, (ZnPc), an unsubstituted phthalocyanine ( $H_2Pc$ ) and N719 as an example. In this diagram the HOMO and LUMO of the dye have been obtained from cyclic voltammetry and light absorption measurements. The distribution of these levels has been approached using light absorption measurements and considering the broadening effects of absorption onto the  $TiO_2$  and solvation by the electrolyte. To simplify the scheme a Gaussian has been used to describe the distribution of the dye levels. The acceptor and donor states in the redox have been also approximated to a Gaussian distribution with a reorganization energy of 0.5 eV. For the  $TiO_2$ , the conduction band edge is represented as a horizontal line and the distribution of the states below it as the diagonal line pointing the upward increase of the DOS in the semiconductor. The dots over this line represent the values obtained from the measured capacitances.

From the scheme of Fig. 24 we may derive the following conclusions. In all the samples it is observed that the major loss of voltage is produced by the mismatch between the HOMO of the dye and the redox couple. The higher recombination resistance found for ZnPc is attributed to the higher position of its  $E_c$ . This is interpreted in terms of the charge transfer features in the Marcus model. The recombination takes place between levels at the same energy in  $TiO_2$  and the redox couple, hence, for the cell with a higher conduction band, at a certain voltage ( $E_{Fn}$ ) there are less states full of electrons in the  $TiO_2$  able to recombine with the  $I_3^-$  acceptor in the redox.

In terms of injection, the position of the conduction band relative to the position of the LUMO of the dye may limit the efficient injection of electrons in the semiconductor if  $E_c$  is above the LUMO. This is not the case in the samples of Fig. 24 owing to the use of an electrolyte with high contents of Li and

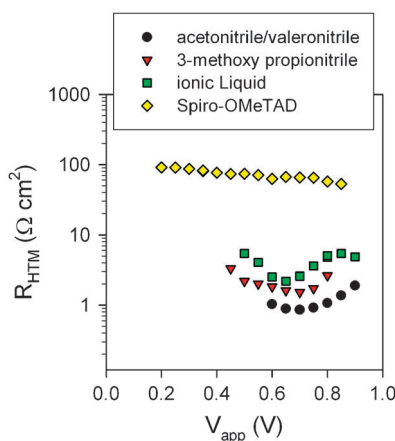


Fig. 25 Comparison of the transport resistance for different hole conductors.

no other additives such as *tert*-butyl-pyridine that raise the conduction band in TiO<sub>2</sub>.

## 5.2 The hole conductor

The choice of the right hole conductor is an important aspect conditioned by the final purpose of the dye solar cell. In liquid electrolyte cells, the ideal situation would be to use a low viscosity nonvolatile solvent which combines low diffusion resistance for the transport of holes towards the counterelectrode and stability at high temperatures. Unfortunately, obtaining both properties at the same time is not possible and therefore a compromise needs to be taken. If record cells are to be obtained very low viscosity electrolytes are used, as this reduces the series resistance contribution from the hole conductor to a minimum. Typically combinations of acetonitrile and valeronitrile are used for this purpose.<sup>3</sup> If the objective is to obtain cells with high stability avoiding the problems caused by leakages due to high volatile solvents, electrolytes based on methoxypropionitrile or ionic liquids<sup>97</sup> are used. As it is shown in Fig. 25, the price to pay is a larger  $R_{\text{HTM}}$  due to their higher viscosity.

Some advances have been shown recently by the addition of clays to electrolytes.<sup>118,119</sup> These both produce a gel phase that diminishes the volatility of solvents and keep very high mobility in the electrolyte with little changes in  $R_{\text{HTM}}$ .

In solid state hole conductors, such as 2,2',7,7'-tetrakis(*N,N*-di-*p*-methoxyphenyl amine)-9,9'-spirobifluorene (spiro-OMeTAD), poly(3,4-ethylenedioxythiophene) (PEDOT) or poly-3-hexylthiophene (P3HT), the characteristic transport time in the electrolyte or hole conductor is close or even larger than the electron lifetime, in terms of their characteristic frequencies,  $\omega_d^0 \geq \omega_{\text{rec}}$ . Then it is required the use of the transmission line model that considers resistance both for electron and hole transport,<sup>27,93</sup> as it is suggested in Fig. 16(b).

By using this model, it was possible to measure the  $R_{\text{HTM}}$  ( $= r_{\text{HTM}} \times L$ ) in spiro-OMeTAD of a 4% efficient cell<sup>27</sup> finding that it presents larger values than the liquid electrolyte cells, see Fig. 25. Therefore apart from the pore filling problems typically reported for solid DSCs<sup>3</sup> and the higher recombination typically found in them,<sup>17,120–122</sup> doping of the hole conductor

material needs to be raised to obtain larger conductivities and thus lower  $R_{\text{HTM}}$ .

## 5.3 Substrates

The functions of the substrate over which the TiO<sub>2</sub> layer is deposited are to: (i) provide a physical structure to which the active film adheres firmly, (ii) provide good electrical contact with the TiO<sub>2</sub>, (iii) evacuate efficiently the photogenerated electrons and (iv) allow the light to pass through.

The most common material used as a substrate in DSC is a glass with a thin layer of fluorine doped tin oxide (SnO<sub>2</sub>:F) commonly known as FTO. FTO beats other transparent conductor oxides such as the solid solution of indium oxide and tin oxide (known as ITO) or doped zinc oxides (ZnO:Ga, ZnO:Al, etc.) due to its superior thermal and mechanical stabilities. In the case of ITO, the cost is also an issue despite its superior sheet resistance, while in the case of ZnO based electrodes the main limitation found is the chemical stability of the electrode in the electrolyte.

The resistance of the substrate is given by

$$R_S = R_{\text{sheet}} \frac{d_L}{d_w} \quad (93)$$

with  $d_L$  the length of the substrate electrode and  $d_w$  its width. As may be seen in Fig. 21(a),  $R_S$  contribution to the total series resistance of the cell is usually the largest, thus for high efficiency devices it should be minimized. Diminishing the sheet resistance of the conducting substrate has the counter effect of limiting the total transmittance of the SnO<sub>2</sub>:F layer and thus the charge generation. Thus, transparency typically takes values between 75–90% for sheet resistances that oscillate between 7 and 100 Ω/□. The alternative is to minimize  $d_L$  and maximize  $d_w$  to obtain low resistance geometries, which may be combined with the use of metallic grids to efficiently collect the charge as used in other solar technologies.<sup>123,124</sup>

The use of FTO glass as a substrate presents advantages as stable, tight and rigid material for outdoor applications, but also some drawbacks as weight, fragility and cost for large area panels or, with other purposes, its lack of flexibility. Flexible transparent materials such as ITO coated polyethylene teraphthalate (PET),<sup>29</sup> ITO coated polyethylene naphthalate (PEN),<sup>125</sup> or, more recently, metallic wired fabrics have been proposed as alternatives.<sup>126</sup> However these substrates present two main drawbacks: by one side the semiconductor needs to be adhered to the plastic substrate at low temperatures, which produces poorer TiO<sub>2</sub> connection between colloids and at the substrate/colloid contact, and by the other these substrates present certain permeability to contaminants such as water which limits their long term stability.

Another approach consists in the use of metallic foils such as titanium<sup>127</sup> and incomel.<sup>128</sup> Attempts to use a stainless steel foil have not been successful as it degrades in the presence of the iodine based electrolyte.<sup>128</sup>

The use of metallic substrates has the advantage of providing higher conductivity than the transparent films but as light cannot be collected from the photoelectrode side, some photons are lost due to absorption in both the counterelectrode and the layer of electrolyte on top of the TiO<sub>2</sub>. Incomel presents also the inconvenience that the thick oxide layer

formed between  $\text{TiO}_2$  and the foil produces an extra contribution to series resistance.<sup>128</sup>

#### 5.4 Counterelectrodes

From the electrical point of view, the main functions of the counterelectrodes are (i) to collect the holes carried by the hole conductor and (ii) to evacuate them efficiently.

Typical counterelectrodes used in DSCs consist of a FTO glass, in charge of facilitating the evacuation, coated with a small amount of Pt to facilitate the charge transfer of holes from the redox, by a catalytic effect. To reduce the cost of DSCs for industrial production, the Pt typically used in the counter electrode is substituted by different forms of carbon: carbon black, graphite and carbon black mixtures, carbon nanotubes and nanofibers, *etc.* Apart from cost, the advantages of using carbon are high stability and good conductivity.

However, charge transfer efficiency of carbon is in general lower than in the case of Pt-based counter electrodes, therefore two approaches are used: thick layers of porous carbon electrodes, incrementing the surface to transfer the charge<sup>129</sup> and the combination of carbon counter electrodes with small amounts of Pt. However, the increase of the film thickness has a general consequence of an increase of the series resistance of the cell due to the transport resistance of the carbon.

Recently, carbon nanofibers have been used presenting excellent photocatalytic response (low  $R_{ce}$ ) but poor conductivity<sup>130</sup> yielding to a total contribution to series resistance higher than standard Pt-based counterelectrodes.

Monolithic cells<sup>131</sup> completely substitute FTO glass and Pt by carbon counterelectrodes with the double advantage of eliminating those relatively costly materials.

Organic hole conductors poly(3,4-ethylenedioxythiophene): poly(styrene sulfonate) (PEDOT:PSS) alone or combined with carbon nanotubes<sup>132,133</sup> are also being studied as possible alternatives to Pt in the counter electrode, presenting promising results with charge transfer resistances slightly higher than platinized electrolytes.<sup>134</sup>

If flexibility is a need, Pt-Ti foil, Pt-ITO PEN and PEDOT:PSS may be used as counterelectrodes.<sup>125,135,136</sup> Until now, the best performance is attained by those containing Pt.

#### 5.5 Ordered metal oxide architectures

With the aim of obtaining DSCs with improved electrical properties, ordered nanostructures such as nanowires and nanotubes have raised considerable interest. The ordered material architecture offers the benefits of: (i) more direct transport pathways uninterrupted by inter-particle connections; (ii) the possibility to form surface electrical fields that should reduce recombination by confining the injected electrons in the central zone of the wires<sup>78,79</sup> and (iii) superior void penetration of the organic hole conductor in preparation of solid-state DSCs due to the less intricate shape of the nanostructure.<sup>137</sup> Several metal-oxide nanowire and nanotube architectures deposited on a conducting substrate for DSC application have been reported, with the majority of studies focusing on the use of  $\text{TiO}_2$ <sup>138</sup> and  $\text{ZnO}$ .<sup>78,79</sup>

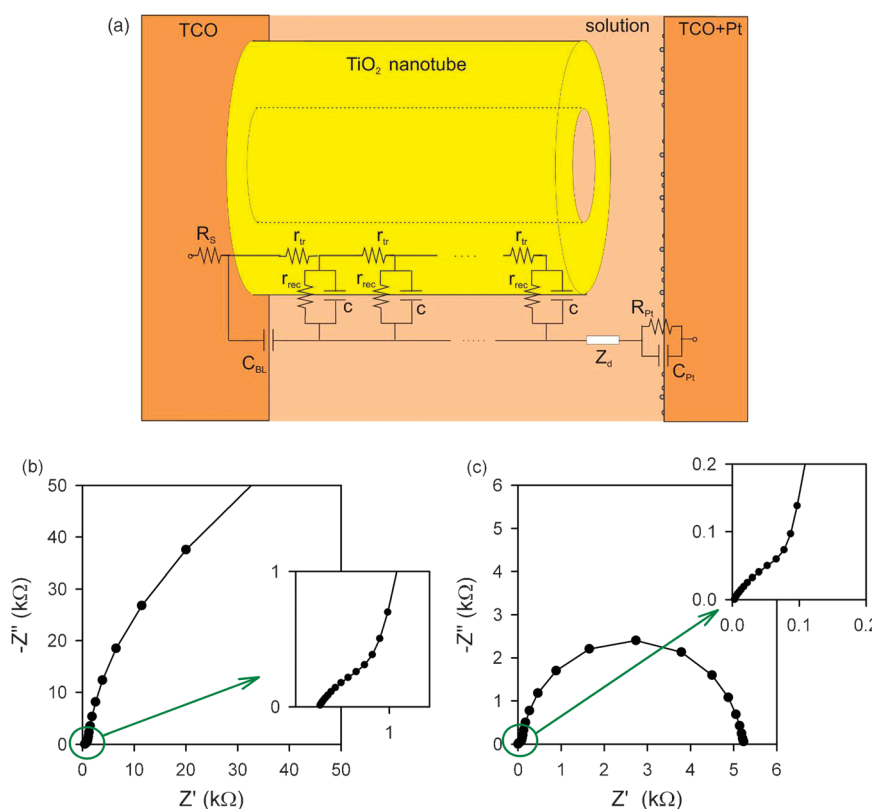


**Fig. 26** (a) Scheme of the equivalent circuit (transmission line) describing IS measurements of a semiconductor nanotube. (b) Impedance spectrum of a nanotube film in an aqueous solution adjusted at pH 11 with KOH at  $V_{app} = 0.35$  V vs. Ag/AgCl. (c) The impedance results of a DSC made with the same type of films, at  $V_{app} = 0.4$  V.

**5.5.1 TiO<sub>2</sub> nanotubes.** A scheme of the application of the transmission line model in semiconductor nanotubes or nanowires is shown in Fig. 26. Concerning the electronic conductivity and the effect of the applied bias voltage in nanowires, we can distinguish two basic situations. The first one has been already explained in Fig. 14: if the nanowire is relatively highly doped, it has a surface depletion layer and a conducting core formed by the neutral region. But in a second case, we consider a thin wire or tube in which doping is low, then we can get a homogenous increase of the Fermi level upon application of

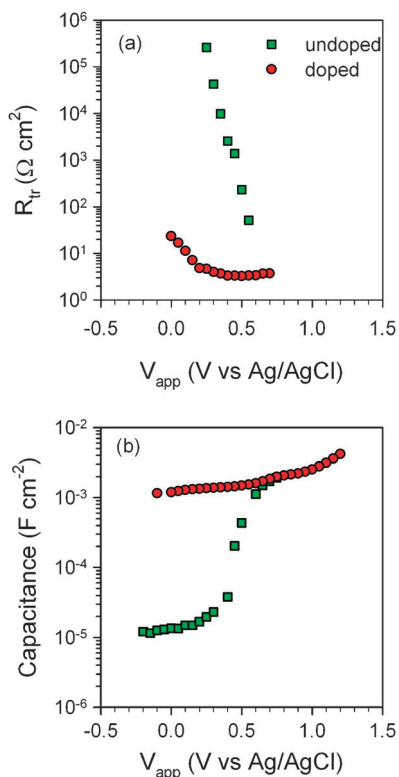


**Fig. 27** (a) The transport resistance and (b) the capacitance of a 5.0  $\mu\text{m}$  long nanotube before and after electrochemical doping. Note that transport resistance values below 10 ohm present a large uncertainty, however they are plotted as a reference. Note that the sign of the potential is changed to preserve the same notation as in the text.

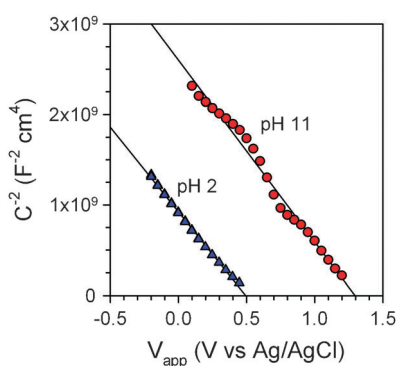


**Fig. 28** Mott-Schottky plots of doped nanotubes in aqueous solution at two different values of pH. Note that the sign of the potential is changed to preserve the notation as in the text.

the voltage. These two situations are in principle distinguished by the behaviour of capacitance and resistance that are obtained in Fig. 27 using the model of Fig. 26. In the highly doped case, the capacitance should obey Mott-Schottky characteristics, see Fig. 28, and the transport resistance should vary relatively slowly with bias (unless full depletion is obtained). In the low-doped case we should record a chemical capacitance and a strong variation of the carrier density, and consequently of the transport resistance, by variation of the voltage.

IS measurements of nanotube arrays of TiO<sub>2</sub> shown in Fig. 26 indicate that the transmission line model is suitable for the description of the IS characteristics.<sup>103</sup> The fresh nanotubes present the normal diffusion-recombination pattern that consists of the high frequency Warburg-like impedance and the recombination arc at low frequency, see Fig. 26(c).<sup>103</sup> By analysis of the IS parameters, shown in Fig. 27, we see that the transport resistance and the capacitance of the film follow in this case the same behaviour as in the case of TiO<sub>2</sub> samples formed of random nanoparticulate networks described above. An exponential decrease of the transport resistance is observed when raising the voltage. A nearly constant value of the capacitance is obtained at low voltages, followed by an exponential increase due to the chemical capacitance when the Fermi level of electrons in TiO<sub>2</sub> raises up.

However, a different behaviour of the parameters is observed when the TiO<sub>2</sub> film is maintained at high voltage for certain time in the presence of protons or Li ions, as observed in Fig. 27. These ions diffuse inside the TiO<sub>2</sub> material, which becomes doped.<sup>103,139,140</sup> In nanotubes, this doped situation is very stable in time.<sup>140</sup> As a consequence, the transport resistance becomes much smaller and nearly constant, Fig. 27(a). Eventually, the values of transport resistance become so low that the impedance spectrum of the nanotube becomes a single arc accounting for charge accumulation and recombination. The effect of doping on the capacitance, Fig. 27(b), is also very relevant. The chemical capacitance change with voltage disappears as the TiO<sub>2</sub> is kept with a large concentration of electrons independently of the voltage.

The high level of doping allows the bending of the conduction band inside the nanotubes, as indicated in Fig. 14, a situation that is not possible in low doped materials.<sup>141</sup> From the data in Fig. 27 and eqn (54), we have determined  $N_D = 1.6 \times 10^{21} \text{ cm}^{-3}$ , with a depletion width, given by eqn (49), of value  $w < 1.5 \text{ nm}$ , see Fig. 28.

**5.5.2 ZnO nanorods.** The electrodeposited synthesis procedure of ZnO nanorods and nanotubes provides highly doped films (up to  $10^{20} \text{ cm}^{-3}$ ). This doping level may be reduced to a value of  $10^{17} \text{ cm}^{-3}$  by using thermal treatments.<sup>78,79</sup>

ZnO wires of relatively large diameter (100–300 nm) can sustain internal band bending at the surface, and are characterized by a depletion layer at the semiconductor/electrolyte interface with a highly conducting central region, providing a dielectric capacitance as indicated in eqn (56).<sup>69,78,79</sup> Capacitance data and fits to the model of eqn (55) and (56) are shown in Fig. 29. For the sample measured as prepared, the standard Mott-Schottky plot is obtained, with a donor density of  $6.2 \times 10^{19} \text{ cm}^{-3}$ . For the annealed sample the Mott-Schottky

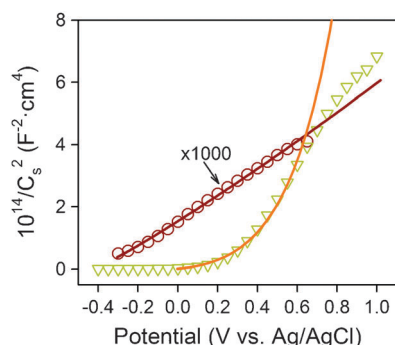


**Fig. 29** Mott–Schottky plots of a ZnO nanowire sample before (dots) and after (triangles) thermal annealing at 450 °C. The solid lines represent the fits to the model explained in the main text.

is bent due to the fact that the donor density has decreased to  $5.5 \times 10^{17} \text{ cm}^{-3}$ .

Thin ZnO layers deposited at the surface on an insulating framework exhibit a very large conductivity.<sup>142</sup> For thick wires the resistance of the core conducting region (Fig. 14) is very small and it is difficult to measure. However, He *et al.*<sup>143</sup> succeeded in obtaining the diffusion–recombination patterns of IS in ZnO nanorods, which allows us to obtain all transport and capacitance parameters.

## 6. Quantum dot sensitized solar cells

The use of inorganic semiconductors as light absorbing materials, instead of organic dyes, in metal oxide nanostructured sensitized cells has attracted increasing attention.<sup>9–11,13,14,136,144</sup> Semiconductor sensitized solar cells (SSCs) are also commonly known as quantum dot sensitized solar cells (QDSCs), when the semiconductor absorbing material demonstrates a quantum confinement regime or extremely thin absorber cells (ETA) if the absorber is distributed continuously on the surface of the electron conducting medium. Inorganic semiconductor materials are specially interesting as light absorbing materials as they present higher extinction coefficients than molecular dyes and a tunable band gap (tuned, for example, changing the QD size and consequently the quantum coefficient).<sup>145</sup> In addition, semiconductor QDs can be prepared in a relatively easy way in a colloidal form or grown directly on the wide band gap nanostructured matrix (*i.e.* TiO<sub>2</sub>, ZnO).<sup>100</sup> Although currently SSCs have efficiencies lower than DSCs (5.13% being the highest reported value<sup>146</sup> under 1 sun illumination), their efficiencies are experiencing a rapid growth in recent years. In order to obtain a further increase in the performance of QDSCs, coherent models of the device performance are needed and the power and versatility of IS will undoubtedly contribute to attain this goal.

### 6.1 Impedance spectra of QDSCs

QDSCs are formally analogous to DSCs, in this sense, the impedance models developed for DSC, Fig. 16 and 18, can be employed in the analysis of QDSCs, but the special characteristics of QDSCs must be taken into account, as electrolyte, counterelectrode or QD deposition mode. Currently one of the most important limiting factors for the development of QDSCs is the hole conductor material.<sup>11,13</sup> The iodine redox

couple, commonly used in DSCs, has to be avoided in QDSCs (unless QDs are protected),<sup>147</sup> and alternative redox couples are used to avoid photocorrosion. The pattern of the IS will depend on the redox used, as different redox have different transporting properties and different charge transfer behavior with the counterelectrode.

Co-redox presents good charge transfer properties between an electrolyte and a platinized counterelectrode, consequently IS similar to the ones depicted in Fig. 17 is obtained, where the transmission line is perfectly recognized.<sup>37</sup> On the other hand, Co-redox presents a photocurrent limitation due to the electrolyte diffusion, as demonstrated through impedance measurements.<sup>148</sup> A polysulfide electrolyte has been employed to avoid this photocurrent limitation, and the energy level of this redox couple as well as a number of CdSe QDs of varying sizes are indicated in Fig. 7(b). Charge transfer between the polysulfide electrolyte and platinized counter electrode is low, producing a problem of high counter electrode resistance that strongly reduces the cell performance.<sup>54</sup> This increase of the counter electrode resistance is reflected in the impedance pattern as an increase of the size of the first arc observed in Fig. 18, obtained at high frequencies. The overlap of the first (counterelectrode) and second arcs (active layer) does not allow us to distinguish the transmission line pattern (the straight line), and the impedance spectra can be fitted using the simple model plotted in Fig. 18(e),<sup>100</sup> but the information about electron transport is lost. The use of alternative counter electrodes with the polysulfide electrolyte can solve partially this problem. Cu<sub>2</sub>S presents lower charge transfer resistance with the polysulfide electrolyte,<sup>149,150</sup> reducing the device series resistance and increasing consequently the cell FF. From the point of view of impedance analysis the complete pattern of the sensitized solar cell is recovered, distinguishing clearly the transmission line behaviour,<sup>35,36</sup> when Cu<sub>2</sub>S is employed.

One of the strongest points of the SSCs is their versatility. Different kinds of inorganic semiconductors can be employed<sup>9,10</sup> whenever their conduction bands lie above the conduction band of the nanostructured electron transporter, in order to allow the electron photoinjection. The sun spectra can be matched varying either the semiconductor employed or the semiconductor confinement that allows a band gap tuning to higher values than the bulk band gap. In addition, a specific semiconductor material can be deposited in several ways.<sup>100</sup> The cell performance is influenced by the deposition mode and its effect can be analyzed by impedance spectroscopy. As an example, we have shown that QDSCs using colloidal CdSe QDs present lower recombination resistance than CdSe QDs grown by chemical bath deposition (CBD), inducing a higher  $V_{oc}$  in the latter cells.<sup>100</sup> CBD samples allow the deposition of a larger amount of light absorbing semiconductor material, producing a more effective covering of the TiO<sub>2</sub> surface than in the case of colloidal QDs. Thus, QDs themselves act as blocking layers, hindering the recombination of electrons in the TiO<sub>2</sub> with the acceptor species in the electrolyte. Then, the covering of TiO<sub>2</sub> improves, generally, the recombination resistance that becomes higher.

### 6.2 Surface treatments on QDSCs

Surface treatments have a dramatic effect on QDSC performance<sup>73</sup> as it is reflected in Fig. 30(a). The origin of this behavior can be

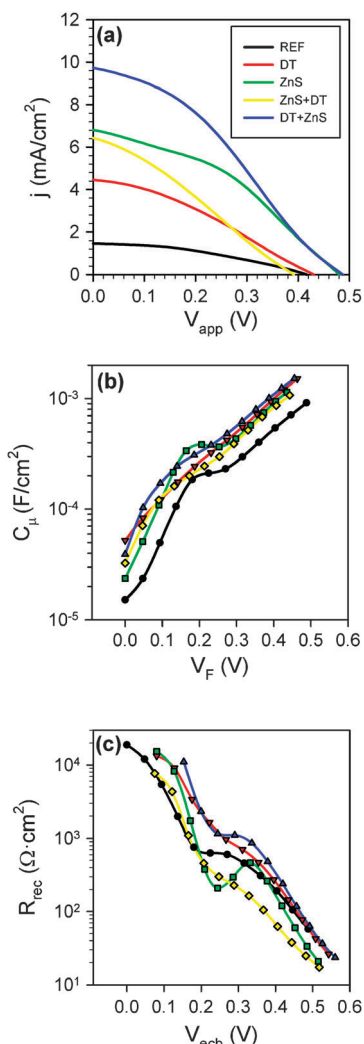


**Fig. 30** Analysis of different quantum dot sensitized electrodes with various surface treatments, using polysulfide as electrolyte and platinized FTO as counter electrode. The sample after QD growth by chemical bath deposition with no treatment is taken as the reference sample (Ref). Two configurations with only one treatment have been analyzed: with ZnS coating (ZnS sample) and with dipole grafting (DT sample, using 4-methoxybenzenethiol as molecular dipole). In addition, samples with two treatments: first DT and second ZnS coating (DT + ZnS) and first ZnS coating and second a dipole treatment (ZnS + DT) have been explored. (a)  $j$ - $V$  curves. The cells presented an efficiency of Ref ( $\eta = 0.23\%$ ), DT ( $\eta = 0.63\%$ ), ZnS ( $\eta = 1.25\%$ ), ZnS + DT ( $\eta = 0.71\%$ ) and DT + ZnS ( $\eta = 1.60\%$ ); (b) capacitance vs.  $V_F$  and (c) recombination resistance vs.  $V_{ecb}$ .<sup>73</sup>

understood by analyzing the data extracted from impedance measurements, specially taking into account the chemical capacitance, Fig. 30(b), and the recombination resistance, Fig. 30(c). The different surface treatments performed on CdSe sensitized electrodes produce a downwards shift of the TiO<sub>2</sub> conduction band, see Fig. 30(b). In addition, the use of molecular dipoles shifts the QD bands up.<sup>147</sup> Both effects contribute to increase the photogenerated electron driving force<sup>151,152</sup> and consequently the photocurrent, see Fig. 30(a). The downwards movement of TiO<sub>2</sub> bands is associated commonly with an increase of the photocurrent and a diminution in photovoltage.

But, this is not the case observed in Fig. 30(a), where an increase of photovoltage is observed after the treatments. This increase of the photovoltage is due to an increase of the recombination resistance for the treated cells, see Fig. 30(c). This result points out to the important role of the surface treatment in the enhancement of QDSCs performance,<sup>73</sup> and how IS characterization can help to attain this goal.

It is also interesting to highlight the peak observed in the chemical capacitance and in the recombination resistance. This behavior is commonly associated with the recombination through TiO<sub>2</sub> surface states.<sup>72,99,100,153,154</sup>

### 6.3 Semiconductor light absorbing material for QDSCs

Although the basic configuration of QDSCs and DSCs is similar, there are important points of departure of the specific mechanisms. Multiple layers of absorbing semiconductor on the oxide and charge traps in the absorbing semiconductor originate important differences that influence the solar cell performance.<sup>13</sup> The existence of surface states in the semiconductor light absorbing material introduces an alternative recombination pathway, through these states, non-existent in conventional DSCs.<sup>13</sup> The nature of the surface states depends not only on the semiconductor preparation method but also on the semiconductor material. QDSCs using three different semiconductor materials: PbS with bulk band gap  $E_g = 0.41$  eV, CdSe  $E_g = 1.73$  eV and CdS  $E_g = 2.42$  eV, grown by successive ionic layer deposition and reaction (SILAR) are compared in Fig. 31. The semiconductor light absorbing material influences the TiO<sub>2</sub> conduction band position, see Fig. 31(b). The differences in photocurrent observed, see Fig. 31, are originated in one hand on the different semiconductor gaps, but recombination also plays a remarkable role in cell performance. PbS presents the narrowest gap and the higher photocurrent should be expected. In contrast low photocurrent and photovoltage are obtained for PbS QDSCs, see Fig. 31(a), due to an important recombination observed when this semiconductor is employed, Fig. 31(c). CdS exhibits a significant lower recombination, as the high recombination resistance reflects. Thus, CdS is an especially attractive sensitizer from the point of view of recombination. The recombination of PbS QDSCs can be significantly reduced if PbS is coated with CdS, see Fig. 31(c), and photocurrent and photovoltage considerably enhanced, see Fig. 31(a), by the combination of both materials. In addition, the CdS avoids the photo-corrosions of PbS with the polysulfide electrolyte stabilizing the cell.<sup>35</sup> QDSC of CdSe prepared with three SILAR cycles presented an intermediate recombination between PbS and CdS. The recombination decreases with the number of CdSe SILAR cycles, see Fig. 31(c), while the downwards shift of the TiO<sub>2</sub> conduction band increases, see Fig. 31(b). Both effects could be attributed to the effect of the blocking layer performed by the QD absorber, as it has been previously commented.<sup>36</sup>

On the other hand, CdS<sub>5</sub>, PbS<sub>2</sub>/CdS<sub>5</sub> and CdSe<sub>3</sub> present values of  $\beta$  relatively close to 0.5, commonly observed in conventional DSCs, see Fig. 31(c). The  $\beta$  value decreases for CdSe QDSCs as the number of SILAR cycles increases. This fact could indicate a change in the recombination pathway from a recombination of electrons in the TiO<sub>2</sub> with

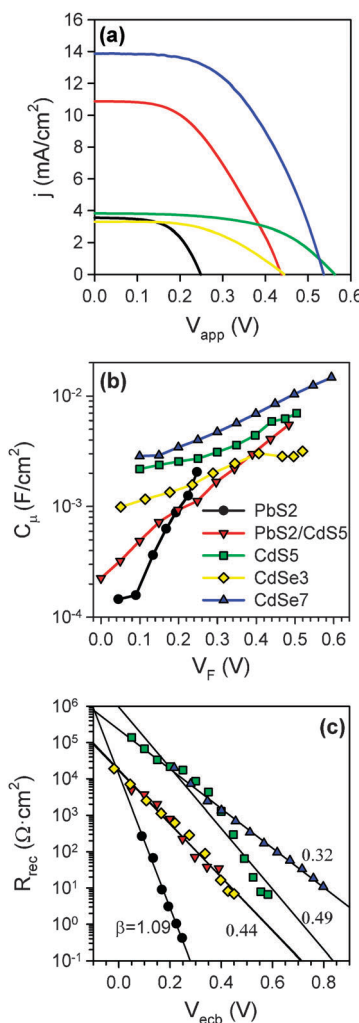


**Fig. 31** Analysis of different quantum dot sensitized electrodes using different semiconductor light absorbing materials, using polysulfide as an electrolyte and Cu<sub>2</sub>S as a counter electrode. All the samples have been coated with two SILAR cycles of ZnS. The different semiconductors have been grown by SILAR,<sup>35,36</sup> the number after the name of the semiconductor material indicates the number of SILAR cycles performed. (a)  $j$ - $V$  curves. The cells presented an efficiency of PbS<sub>2</sub> ( $\eta = 0.51\%$ ), PbS<sub>2</sub>/CdS<sub>5</sub> ( $\eta = 2.21\%$ ), CdS<sub>5</sub> ( $\eta = 1.22\%$ ), CdSe<sub>3</sub> ( $\eta = 0.73\%$ ) and CdSe<sub>7</sub> ( $\eta = 3.83\%$ ); (b) capacitance vs.  $V_F$  and (c) recombination resistance vs.  $V_{ecb}$ , solid lines are the linear fits of the experimental data. Using eqn (26) the  $\beta$  parameter of each cell has been obtained and indicated on the graph.

the acceptor states in the electrolyte, process  $R_{HC}$  in Fig. 32, for low number of SILAR cycles, to a recombination through the QDs for a high number of SILAR cycles, process  $R_{SC}$  in Fig. 32. The recombination pathways in QDSCs could be mediated by trapping events, see Fig. 32. The role of QD traps in the recombination is an important issue that needs a deeper analysis in order to increase the QDSCs performance.<sup>11,13</sup> CdSe<sub>7</sub> and CdS<sub>5</sub> present  $R_{rec}$  values very close, but a  $\beta$  value for CdSe<sub>7</sub> is 0.32, while for CdS<sub>5</sub> is 0.49. Then, the CdS<sub>5</sub> sample presents lower recombination than the CdSe<sub>7</sub> sample, as discussed in Section 4.6.3. In addition the  $\beta$  value, higher than one, obtained for PbS<sub>2</sub> QDSCs is an indication of a degradation process.

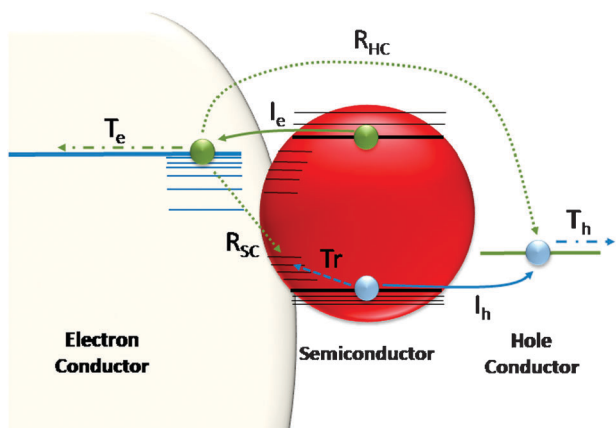


**Fig. 32** Charge transfer and transport processes for photogenerated electron (green arrows) and hole (blue arrow) in QDSCs. Injection (solid arrow), trapping (dashed arrow), recombination (dotted arrow) and transport (dash-dotted arrow) are indicated. Photogenerated electrons (green) are injected from the QD conduction “band” (CB) to the electron conductor CB,  $I_e$ . The injected electron is transported in the electron conductor media,  $T_e$ . Holes (grey) are injected into the hole conducting media  $I_h$ . For efficient cell operation charge transfer and transport processes have to be faster than recombination. There are different recombination pathways in QDSCs. Electrons in the CB of the electron conductor can recombine with acceptor species in the hole conductor,  $R_{HC}$ . In addition, there is an alternative recombination pathway through the semiconductor,  $R_{SC}$ , this recombination could be mediated by trapping events,  $Tr$ , either in the electron conductor or in the light absorbing semiconductor. This representation provides a simplified view of the system, more complete cartoons can be consulted in ref. 11.

## 7. Organic bulk heterojunction solar cells

Organic conducting materials are at the heart of BHJ solar cells, a promising alternative to silicon-based solar cells due to their optical, electronic and mechanical properties.<sup>4,7</sup> BHJ are formed by an interpenetrating blend of an optically active polymer and electron accepting molecules. At the optically active polymer, excitons are created by light absorption. These excitons dissociate at the polymer/molecule interface, thus spatially separating the electrons and holes which therefore can be transported to the electrodes by hopping. Hence the absorbing blend forms an effective transporting medium in which electrons occupy electronic states of the LUMO of the acceptor fullerene, and holes populate the HOMO of the donor polymer. The absorbing blend is sandwiched between two contacting materials, usually metallic cathodes and highly-doped organic transporting layers.

The archetypical BHJ structure uses polythiophene and fullerene derivatives to form the active blend as ITO/PEDOT: PSS/P3HT:PCBM/M (P3HT: 3-hexylthiophene, PCBM: phenyl C<sub>61</sub>-butyric acid methyl ester, and M: a metallic cathode). Solution-processed polymer:fullerene cells achieved between 6% and 8% power conversion efficiency by the use of novel compounds, substrates and contacting materials as well as additives optimizing the phase separation.<sup>155,156</sup> In particular a new class of PTB polymers with low bandgap has provided the highest efficiencies.<sup>5,157</sup>

It is widely agreed that the open-circuit voltage is given by the separation of Fermi levels of electrons in the fullerene and holes in the polymer. Therefore the basic scheme in Fig. 1 applies well in the BHJ. However there are many uncertainties concerning the explanation of the  $jV$  curve and the generation of photocurrent and the transport mechanism in general. The literature heavily emphasizes the dissociation of excitons (and charge transfer states) as a predominant factor for the photocurrent and fill factor. This approach usually relies on the dependence of the dissociation factor (or suppression of recombination) on a macroscopic electrical field in the device that would be regulated by the applied voltage.<sup>158,159</sup> It has even been suggested that the photocurrent is space-charge limited.<sup>160</sup> Elsewhere we will present a critique of these models that are largely based on earlier models for photoconduction in insulators. Here we provide our view on charge distribution and energetics in standard BHJ devices, as obtained from the interpretation of the measured capacitances. As this model is markedly different from the prevalent picture in the literature, we first explain the properties of the device and then we show some evidence from capacitance results.

### 7.1 Energetic picture of the BHJ device

The basic device model is shown in Fig. 33. First, Fig. 33(a) shows central properties of the polymer/fullerene blend. The equilibrium Fermi level of electrons and holes is shown close to the HOMO level of P3HT, and this means that from the beginning we assume that the blend is not an insulator, rather it contains hole majority carriers, with characteristic densities (in our measurements) of  $10^{15}$ – $10^{17} \text{ cm}^{-3}$ , which is a significant concentration, as the photogenerated carrier density at 1 sun can barely exceed these numbers. The origins of these majority carriers are negatively charged defects that cause p-doping of

P3HT when exposed to air or moisture,<sup>161,162</sup> or caused by structural defects induced during blend processing.<sup>163</sup>

When the blend is contacted with the electron extracting contact with a low work function  $\phi_c$  a Schottky barrier is formed *at this contact*. The height of the barrier, which is the flatband potential, is given by the difference of the Fermi level of the blend,  $\phi_s = E_{F0}$ , and the cathode workfunction

$$V_{fb} = [E_{F0} - \phi_c]/q \quad (94)$$

as shown in Fig. 33(b) (neglecting interfacial dipole). Consequently, a depletion zone at the P3HT/M contact is formed which entails bending of the transporting bands, and this is indicated also in Fig. 33(b). On the other hand, the anode contact is regarded as ohmic because of the practical alignment between the PEDOT:PSS hole transport layer at the contact and P3HT HOMO levels.

This model implies that in equilibrium (zero bias voltage in the dark) the depletion zone occupies a large portion of the active layer. The width of the depletion zone obviously depends on the layer thickness and the doping level. At a low forward bias the depletion zone decreases and is confined to the cathode contact, Fig. 33(c). At  $V_{app} = V_{fb}$  (flat-band conditions), which is about  $V_{fb} = 0.3$ – $0.5$  V, the depletion layer adjacent to the P3HT:PCBM/M contact disappears and the neutral, doped region extends along the whole diode bulk.

One important consequence of this model is that there is no overall electrical field in the device associated with the difference of the work functions of the contact materials at the two sides of the blend. Instead, each contact has its own equilibration, due to the starting number of electronic carriers in the blend.

If a reverse voltage is applied, then all the carriers are removed from the blend region, and in this case there is an overall field and the blend becomes a dielectric. But according

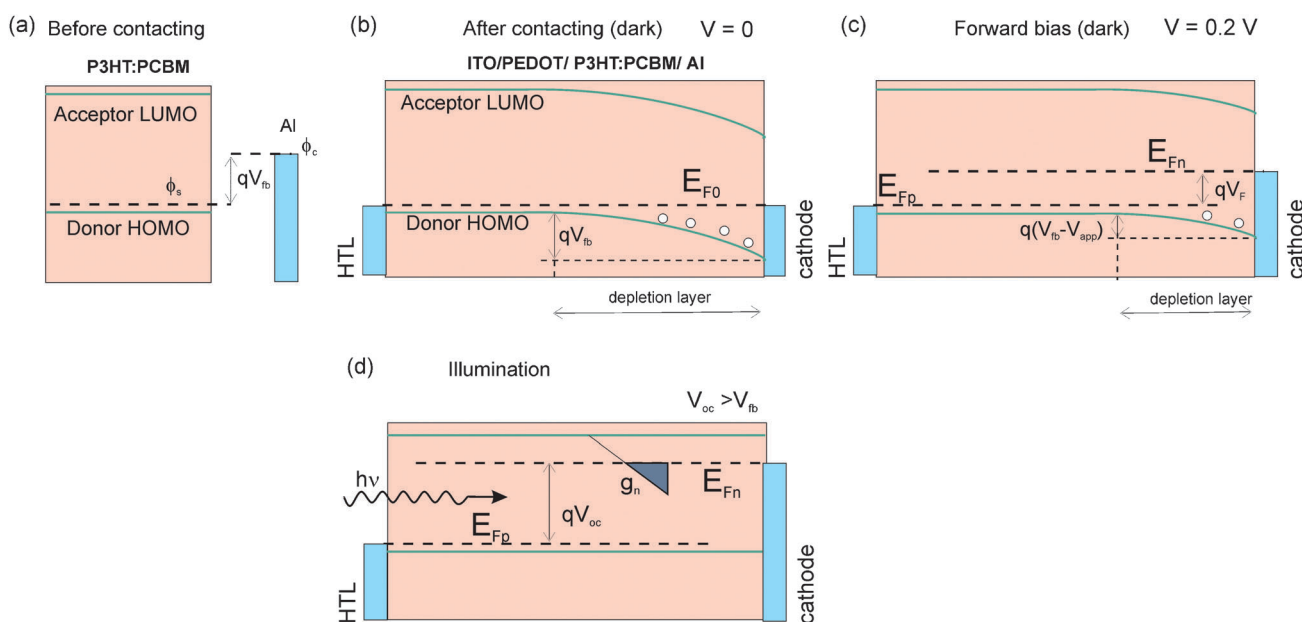


**Fig. 33** Band structure of the P3HT:PCBM heterojunction. (a) Separate representation of the blend and the cathode metal. (b) Equilibrium after contact ( $V_{app} = 0$ ). Band bending appears near the cathode and holes can occupy HOMO states of the P3HT within the neutral region. (c) Forward voltage lower than flatband condition at the cathode. (d) Open circuit condition under illumination.

to our model, this situation is restricted to the reverse voltage. In forward, the raise of the Fermi level of the electrons first removes the barrier at the contact with the cathode, as already explained. Then, at even higher forward voltage, the Fermi level continues to raise. This is shown in Fig. 33(d), corresponding to the open-circuit condition under illumination, and is indeed similar to the basic and general model given in Fig. 1(b).

## 7.2 Interpretation of the measured capacitance as a function of voltage

Now we describe how the model of Fig. 33 allows the interpretation of the measured capacitance as a function of voltage. A characteristic measurement is shown in Fig. 34(a) and the following four feature regions can be distinguished.

- (i) At a large reverse bias, the sample is a dielectric capacitor with a constant capacitance.
- (ii) At a moderate reverse and low forward bias ( $V_{app} < V_{fb}$ ) the applied voltage modulates the width of the depletion zone, which results in the capacitance–voltage relationship which approaches a Mott–Schottky expression given in eqn (52). This behaviour is shown in Fig. 34(b). The charge coming from negatively charged defects is distributed along the depletion zone, whose width is variable with the applied voltage. More generally the spatial charge distribution along the layer thickness gives rise to a wide variety of capacitance–voltage behaviours. Because organic active layers are usually thin ( $\sim 100$  nm) full

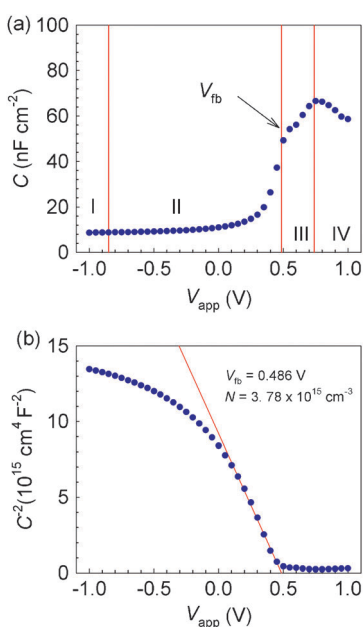


**Fig. 34** (a) Characteristic capacitance response (100 Hz) of a BHJ device with structure ITO/PEDOT:PSS/P3HT:PCBM/Al, as a function of bias voltage. Vertical lines separate voltage regions for which capacitance is determined by the geometrical value  $C_g$  (zone I:  $V_{app} \ll V_{fb}$ ), depletion layer modulation  $C_{sc}$  (zone II:  $V_{app} < V_{fb}$ ), the storage of excess carriers  $C_\mu$  (zone III:  $V_{app} > V_{fb}$ ), and limitation mechanisms (zone IV:  $V_{app} \gg V_{fb}$ ). (b) Mott–Schottky curve (100 Hz) which exhibits a straight line from which the values  $V_{fb} = 0.49$  V and  $N_A = 3.8 \times 10^{15} \text{ cm}^{-3}$  are determined, assuming  $\epsilon = 3$  for P3HT:PCBM.

depletion is reached at a relatively low reverse bias, and the measured capacitance corresponds to the geometrical value, as mentioned in (i).

- (iii) At a forward voltage in excess of the flat-band potential ( $V_{app} \geq V_{fb}$ ) the depletion zone collapses so that the capacitance is governed by a chemical capacitance due to the excess carriers  $C_\mu$ <sup>69,164</sup> that is related to the change of the occupancy of charge carriers in the fullerene LUMO and polymer HOMO. This is shown in Fig. 33(d).

- (iv) At a larger forward bias it is usually observed that the capacitance saturates and eventually decreases giving even negative values.<sup>113</sup>

We show in Fig. 34(a) results of the measurement of capacitance using aluminium contacts that satisfy eqn (54) and exhibit a straight line over a bias voltage range between approximately zero and  $V_{fb}$ , Fig. 34(b). From the fit to Mott–Schottky curve we obtain  $V_{fb} = 0.49$  V and  $N_A = 3.8 \times 10^{15} \text{ cm}^{-3}$ , assuming  $\epsilon = 3$  for P3HT:PCBM.<sup>38,165</sup>

In Fig. 35 two extreme examples of the behaviour of the capacitance in a BHJ are shown. On one hand is the case of a thick P3HT:PCBM layer (200 nm) in which the linear Mott–Schottky relationship extends to a large reverse bias. In this case the depletion region for a reverse bias voltage between 0–1 V results to be varying between 63–115 nm, compatible with an active layer thickness of 200 nm. This behaviour occurs because of a relatively high p-doping,  $N_A = 3.5 \times 10^{16} \text{ cm}^{-3}$ . The second example exhibits a nearly full depletion of the active layer even at a positive bias, as derived from the saturation in reverse of the  $C_{sc}^{-2}$  vs.  $V_{app}$  plot [Fig. 35(b)].

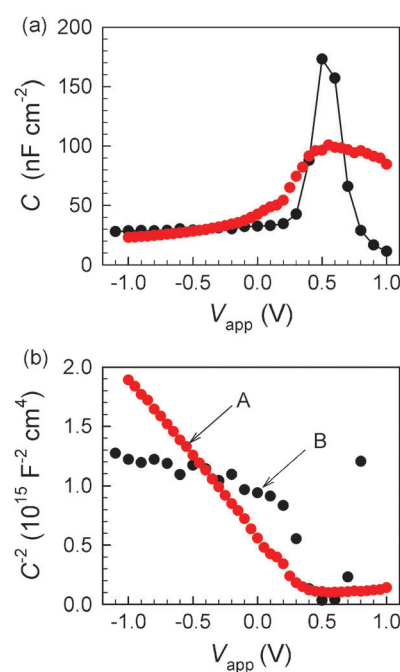


**Fig. 35** Examples of (a) capacitance–voltage and (b) Mott–Schottky curve measured at 1 kHz of structures ITO/PEDOT:PSS/P3HT:PCBM/M which exhibits a straight line in a wide or narrow voltage region depending on the doping level and active layer thickness. Curve A:  $N_A = 3.5 \times 10^{16} \text{ cm}^{-3}$ , and 200 nm thick layer. Curve B:  $N_A = 1.3 \times 10^{16} \text{ cm}^{-3}$ , and thinner films (90 nm), assuming  $\epsilon = 3$  for P3HT:PCBM. Full depletion is achieved for curve B even at positive bias.

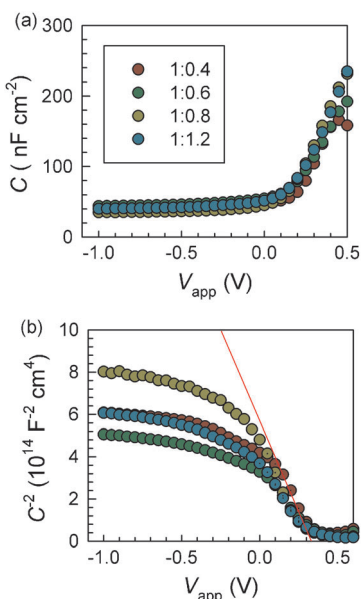


**Fig. 36** (a) Capacitance and (b) Mott–Schottky curve (100 Hz) of structures ITO/PEDOT:PSS/P3HT:PCBM/Ca/Al which exhibits a straight line yielding  $V_{\text{fb}} = 0.35\text{--}0.40$  V and  $N_A = 1\text{--}2 \times 10^{16} \text{ cm}^{-3}$ , assuming  $\varepsilon = 3$  for P3HT:PCBM. Full depletion is achieved at a reverse bias and a linear relationship, eqn (53), at low forward bias (0.0–0.3 V). Different polymer/fullerene weight ratios are explored. The active layer thickness was approximately 100 nm.

The reduced doping level ( $N_A = 1.3 \times 10^{16} \text{ cm}^{-3}$ ) and thinner films (90 nm) make the linear Mott–Schottky part confined into a narrow voltage range.

Additional examples are shown in Fig. 36. These Mott–Schottky plots correspond to solar cells of structure ITO/PEDOT:PSS/P3HT:PCBM/Ca/Ag of different polymer/fullerene weight ratios, and active layer thicknesses around 100 nm.<sup>166</sup> Energetics and density of impurity, defect, or trap levels in BHJ have been recently determined based on analysis of capacitance spectra  $C_{\text{sc}}(f)$ .<sup>167–169</sup> The technique consists in calculating the junction capacitance derivative with respect to the angular frequency of the small voltage perturbation.<sup>170</sup>

### 7.3 Interpretation of the impedance spectra

The primary goal of our measurements so far has been the understanding of the photovoltage in connection with the energy picture drawn in Fig. 33. In order to force the photovoltaic device to mainly operate under recombination conditions, one can perform IS measurements at the open-circuit. Under such conditions no direct current is allowed  $j_{\text{dc}} = 0$ , so that transport mechanisms play a secondary role.

Typical impedance responses in open-circuit conditions by varying the illumination level can be seen in Fig. 37 and 38.<sup>171</sup> The spectra are characterized by a major  $RC$  arc plus additional minor features at high frequency. The high-frequency part of the spectra may contain information of transport and series resistance elements, as well as dielectric contributions.<sup>38</sup> The low frequency arc is attributed to recombination in the photoactive blend.<sup>72</sup> The capacitance, resistance, and lifetime

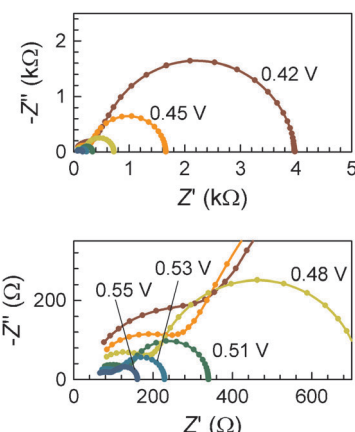


**Fig. 37** Impedance spectra of BHJ devices of structure (ITO/PEDOT:PSS/P3HT:PCBM/LiF/Al) measured in open-circuit conditions under varying illumination. Experimental points (symbols) and fitting results (solid line). Open-circuit voltage is marked in each spectrum.

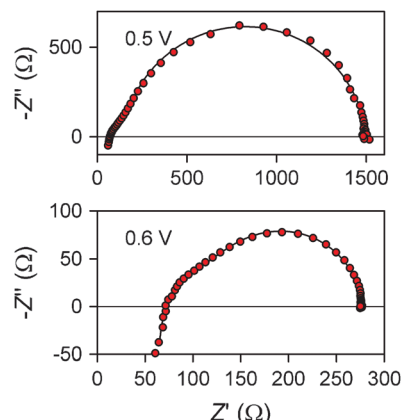


**Fig. 38** Impedance spectra of BHJ devices of structure (ITO/PEDOT:PSS/P3HT:PCBM/LiF/Al) measured in the dark at different biases as indicated. Experimental points (symbols) and fitting results (solid lines). An additional inductive element has been included in series accounting for the wire induction.

values, as a function of open-circuit voltage, are shown in Fig. 39.

At increasing  $V_{\text{oc}}$  the capacitance in Fig. 39(a), corresponding to the region III of Fig. 34, records the density of states of the LUMO level of the acceptor fullerene. The DOS shows a broad disorder, it can be usually described by a Gaussian distribution but as we can only observe the lower tail of the DOS, in some cases the capacitance is well approximated by an exponential distribution.

The resistance of the main arc is the recombination resistance, Fig. 39(b).  $R_{\text{rec}}$  shows an exponential decrease with the bias voltage as stated before in  $\beta$ -recombination model, eqn (42).

The presence of the negative capacitance should be remarked. In Fig. 40(a), which corresponds to the  $C$ – $V$  curve of a P3HT:PCBM-based structure, it is observed a reduction in capacitance that develops negative values for  $V_{\text{app}} > 0.75$  V. This negative capacitance effect can be identified either as a crossing point at low-frequencies in a  $Z'$ – $Z''$  plot, Fig. 40(b),

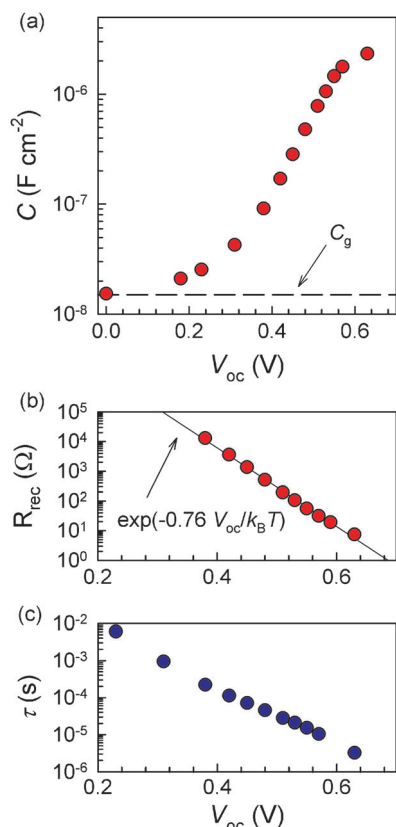


**Fig. 39** Parameters extracted from impedance spectra of BHJ devices of structure (ITO/PEDOT:PSS/P3HT:PCBM/LiF/Al) measured in open-circuit conditions under varying illumination. (a) Capacitance and (b) recombination resistance values from fits of the low-frequency arc of the impedance spectra as a function of varying illumination levels (0.01 to 1 sun). (c) Recombination time (effective lifetime) as a function of  $V_{oc}$  calculated from the  $RC$  time constant.

or as a singularity in the capacitance spectra of Fig. 40(c). As discussed elsewhere, several electronic mechanisms have been proposed in order to explain it, related to either outer interfacial phenomena, or limitation of charge storage at the device bulk.<sup>113</sup>

#### 7.4 Main characteristics of BHJ solar cells according to IS results

In general we obtain the picture of Fig. 41. In IS we measure electrons and holes that are thermalized in the respective materials and provide the respective Fermi levels that ultimately produce the measured voltage. There is clear evidence for a wide distribution of the electron states in the fullerene, and we assume that the polymer states are equally broadened in energy (though there is no direct evidence for this). In any case, the number of carriers after charge separation is regulated by recombination. In our view, recombination is produced by separate electrons and holes, there is a probability of a charge transfer as described in ref. 171. In addition to the kinetics of charge transfer of electrons and holes, the actual value of  $V_{oc}$  is strongly influenced by the shape of the DOS (that determines the position of the Fermi level).<sup>172</sup> The comparison of the DOS of different fullerene acceptors provides an explanation

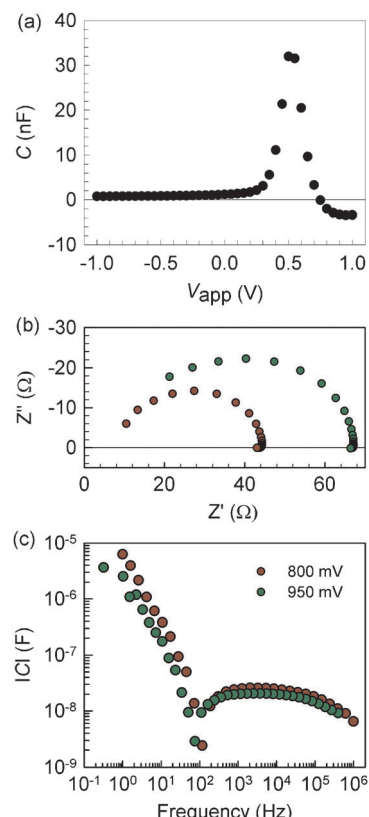


**Fig. 40** (a)  $C$ - $V$  curve exhibiting the negative capacitance effect at large forward bias. (b) Impedance spectra of BHJ devices of structure (ITO/PEDOT:PSS/P3HT:PCBM/LiF/Al) measured in dark conditions at large forward bias. At low-frequencies points describe the negative capacitance effect. (c) Spectra of the capacitance modulus showing the change of quadrant around 100 Hz.

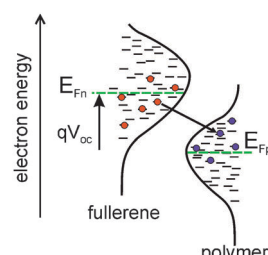


**Fig. 41** Energy scheme suggesting the broad density of states (DOS) in both the polymer and fullerene materials forming a bulk heterojunction solar cell. Thermalized electrons in the fullerene and thermalized holes in the polymer are located predominantly, respectively, in the lower and upper tails of the DOS. The distribution of charges determines the Fermi levels of electrons ( $E_{Fn}$ ) and holes ( $E_{Fp}$ ) whose difference gives the open-circuit voltage  $V_{oc}$  ( $q$  is the elementary charge). Recombination of an electron in a localized state in the fullerene with a hole in the polymer is indicated by an arrow.

to the observed differences of the photovoltage in BHJ solar cells.<sup>42</sup> The  $\beta$ -recombination model holds well, as attested by the exponential shape of the resistance. Therefore the methods based on the recombination diode described in Section 3 of this paper will account for the  $jV$  curve of BHJ solar cells.

## 8. Conclusion

Impedance spectroscopy has become a very useful tool for device characterization and model developing. The technique is versatile because it applies to complete devices while allowing for a distinction among different operating processes. Doping amount, transport features, charge storage, recombination kinetics, and contact effects are some of the functioning mechanisms which can be addressed.

## Acknowledgements

We thank financial support from Ministerio de Ciencia e Innovación under project HOPE CSD2007-00007, and Generalitat Valenciana under projects PROMETEO/2009/058, ACOMP/2009/056 and ACOMP/2009/095.

## References

- 1 T. W. Hamman, R. A. Jensen, A. B. F. Martinson, H. V. Ryswykac and J. T. Hupp, *Energy Environ. Sci.*, 2008, **1**, 66.
- 2 M. Grätzel, *Acc. Chem. Res.*, 2009, **42**, 1788.
- 3 A. Hagfeldt, G. Boschloo, L. Sun, L. Kloo and H. Pettersson, *Chem. Rev.*, 2010, **110**, 6595.
- 4 G. Dennler, M. C. Scharber and C. J. Brabec, *Adv. Mater.*, 2009, **21**, 1323.
- 5 Y. Liang and L. Yu, *Acc. Chem. Res.*, 2010, **43**, 1227.
- 6 J. Goldstein, I. Yakupov and B. Breen, *Sol. Energy Mater. Sol. Cells*, 2010, **94**, 638.
- 7 F. C. Krebs, *et al.*, *Sol. Energy Mater. Sol. Cells*, 2009, **93**, 1968.
- 8 Q. Yu, Y. Wang, Z. Yi, N. Zu, J. Zhang, M. Zhang and P. Wang, *ACS Nano*, 2010, **4**, 6032.
- 9 P. V. Kamat, *J. Phys. Chem. C*, 2008, **112**, 18737.
- 10 S. Rühle, M. Shalom and A. Zaban, *ChemPhysChem*, 2010, **11**, 2290.
- 11 I. Mora-Seró and J. Bisquert, *J. Phys. Chem. Lett.*, 2010, **1**, 3046.
- 12 A. Kojima, K. Teshima, Y. Shirai and T. Miyasaka, *J. Am. Chem. Soc.*, 2009, **131**, 6050.
- 13 G. Hodes, *J. Phys. Chem. C*, 2008, **112**, 17778.
- 14 P. V. Kamat, K. Tvrdy, D. R. Baker and J. G. Radich, *Chem. Rev.*, 2010, **110**, 6664.
- 15 J. Bisquert, *J. Phys. Chem. B*, 2002, **106**, 325.
- 16 F. Fabregat-Santiago, J. Bisquert, G. Garcia-Belmonte, G. Boschloo and A. Hagfeldt, *Sol. Energy Mater. Sol. Cells*, 2005, **87**, 117.
- 17 F. Fabregat-Santiago, J. Bisquert, E. Palomares and J. R. Durrant, *J. Appl. Phys.*, 2006, **100**, 034510.
- 18 Q. Wang, J.-E. Moser and M. Grätzel, *J. Phys. Chem. B*, 2005, **109**, 14945.
- 19 T. Hoshikawa, R. Kikuchi and K. Eguchi, *J. Electroanal. Chem.*, 2006, **588**, 59.
- 20 M. Adachi, M. Sakamoto, J. Jiu, Y. Ogata and S. Isoda, *J. Phys. Chem. B*, 2006, **110**, 13872.
- 21 Q. Wang, S. Ito, M. Grätzel, F. Fabregat-Santiago, I. Mora-Seró, J. Bisquert, T. Bessho and H. Imai, *J. Phys. Chem. B*, 2006, **110**, 19406.
- 22 L. Han, N. Koide, Y. Chiba and T. Mitate, *Appl. Phys. Lett.*, 2004, **84**, 2433.
- 23 D. Zhou, Y. Bai, J. Zhang, N. Cai, M. Su, Y. Wang, M. Zhang and P. Wang, *J. Phys. Chem. C*, 2011, **115**, 816–822.
- 24 J. Liu, R. Li, X. Si, D. Zhou, Y. Shi, Y. Wang, X. Jing and P. Wang, *Energy Environ. Sci.*, 2010, **3**, 1924.
- 25 L. Andrade, S. M. Zakeeruddin, M. K. Nazeeruddin, H. A. Ribeiro, A. Mendes and M. Grätzel, *ChemPhysChem*, 2009, **10**, 1117.
- 26 M. Wang, P. Chen, R. Humphry-Baker, S. M. Zakeeruddin and M. Grätzel, *ChemPhysChem*, 2009, **10**, 290.
- 27 F. Fabregat-Santiago, J. Bisquert, L. Cevey, P. Chen, M. Wang, S. M. Zakeeruddin and M. Grätzel, *J. Am. Chem. Soc.*, 2009, **131**, 558.
- 28 K. Miettunen, J. Halme, M. Toivola and P. Lund, *J. Phys. Chem. C*, 2008, **112**, 4011.
- 29 K. Miettunen, J. Halme, P. Vahermaa, T. Saukkonen, M. Toivola and P. Lund, *J. Electrochem. Soc.*, 2009, **156**, B876.
- 30 B. M. Klahr and T. W. Hamann, *J. Phys. Chem. C*, 2009, **113**, 14040.
- 31 J. W. Ondersma and T. W. Hamann, *J. Phys. Chem. C*, 2009, **114**, 638.
- 32 J. Bisquert and I. Mora-Seró, *J. Phys. Chem. Lett.*, 2010, **1**, 450.
- 33 J. Villanueva-Cab, H. Wang, G. Oskam and L. M. Peter, *J. Phys. Chem. Lett.*, 2010, **1**, 748.
- 34 J. R. Jennings, F. Li and Q. Wang, *J. Phys. Chem. C*, 2010, **114**, 14665.
- 35 A. Braga, S. Giménez, I. Concina, A. Vomiero and I. Mora-Seró, *J. Phys. Chem. Lett.*, 2011, **2**, 454–460.
- 36 V. Gómez-Pedro, X. Xu, I. Mora-Seró and J. Bisquert, *ACS Nano*, 2010, **4**, 5783.
- 37 H. J. Lee, M. Wang, P. Chen, D. R. Gamelin, S. M. Zakeeruddin, M. Grätzel and M. K. Nazeeruddin, *Nano Lett.*, 2009, **9**, 4221.
- 38 G. García-Belmonte, A. Munar, E. M. Barea, J. Bisquert, I. Ugarte and R. Pacios, *Org. Electron.*, 2008, **9**, 847.
- 39 J. Bisquert, G. García-Belmonte, A. Munar, M. Sessolo, A. Soriano and H. J. Bolink, *Chem. Phys. Lett.*, 2008, **465**, 57.
- 40 M. Glatthaar, M. Riede, N. Keegan, K. Sylvester-Hvid, B. Zimmermann, M. Niggemann, A. Hinsch and A. Gombert, *Sol. Energy Mater. Sol. Cells*, 2007, **91**, 390.
- 41 T. Kuwabara, Y. Kawahara, T. Yamaguchi and T. Takahashi, *ACS Appl. Mater. Interfaces*, 2009, **1**, 2107.
- 42 G. García-Belmonte, P. P. Boix, J. Bisquert, M. Lenes, H. J. Bolink, A. La Rosa, S. Filipponi and N. Martin, *J. Phys. Chem. Lett.*, 2010, **1**, 2566.
- 43 I. Mora-Seró, G. García-Belmonte, P. P. Boix, M. A. Vázquez and J. Bisquert, *Energy Environ. Sci.*, 2009, **2**, 678.
- 44 Y. Y. Proskuryakov, K. Durose, M. K. Al Turkestani, I. Mora-Seró, G. García-Belmonte, F. Fabregat-Santiago, J. Bisquert, V. Barrio, D. Lamb, S. J. C. Irvine and E. W. Jones, *J. Appl. Phys.*, 2009, **106**, 0044507.
- 45 J. Bisquert, D. Cahen, S. Rühle, G. Hodes and A. Zaban, *J. Phys. Chem. B*, 2004, **108**, 8106.
- 46 W. Shockley and H. J. Queisser, *J. Appl. Phys.*, 1961, **32**, 510.
- 47 Y. Tachibana, K. Hara, K. Sayama and H. Arakawa, *Chem. Mater.*, 2002, **14**, 2527.
- 48 W. Kubo, A. Sakamoto, T. Kitamura, Y. Wada and S. Yanagida, *J. Photochem. Photobiol. A*, 2004, **164**, 33.
- 49 G. Lozano, S. Colodrero, O. Caulier, M. E. Calvo and H. n. Míguez, *J. Phys. Chem. C*, 2010, **114**, 3681.
- 50 G. P. Smestad, F. C. Krebs, C. M. Lampert, C.-G. Granqvist, K. L. Chopra, X. Mathew and H. Takakura, *Sol. Energy Mater. Sol. Cells*, 2008, **92**, 371.
- 51 P. T. Landsberg and T. Markvart, *Solid-State Electron.*, 1998, **42**, 657.
- 52 C. B. Honsberg, S. P. Bremmer and R. Corkish, *Physica E (Amsterdam)*, 2002, **14**, 136.
- 53 J. García-Cañadas, F. Fabregat-Santiago, H. Bolink, E. Palomares, G. García-Belmonte and J. Bisquert, *Synth. Met.*, 2006, **156**, 944.
- 54 I. Mora-Seró, S. Giménez, T. Moehl, F. Fabregat-Santiago, T. Lana-Villareal, R. Gómez and J. Bisquert, *Nanotechnology*, 2008, **19**, 424007.
- 55 T. Trupke, S. Baumgärtner and P. Würfel, *J. Phys. Chem. B*, 2000, **104**, 308.
- 56 T. Kirchartz and U. Rau, *Phys. Status Solidi A*, 2009, **205**, 2737.
- 57 T. Kirchartz, A. Helbig, W. Reetz, M. Reuter, J. H. Werner and U. Rau, *Progr. Photovolt.: Res. Appl.*, 2009, **17**, 394.
- 58 L. D. Partain, *Solar cells and their applications*, Wiley, Weinheim, 1st edn, 1995.
- 59 D. Veldman, S. C. J. Meskers and R. A. J. Janssen, *Adv. Funct. Mater.*, 2009, **19**, 1939.
- 60 E. M. Barea, C. Zafer, B. Gultein, B. Aydin, S. Koyuncu, S. Icli, F. Fabregat-Santiago and J. Bisquert, *J. Phys. Chem. C*, 2010, **114**, 19840.
- 61 T. Trupke, P. Würfel, I. Uhendorf and I. Lauermann, *J. Phys. Chem. B*, 1999, **103**, 1905.
- 62 E. M. Barea, J. Ortiz, F. J. Payá, F. Fernández-Lázaro, F. Fabregat-Santiago, A. Sastre-Santos and J. Bisquert, *Energy Environ. Sci.*, 2010, **3**, 1985.

- 63 C. H. Henry, *J. Appl. Phys.*, 1980, **51**, 4494.
- 64 M. C. Hanna and A. J. Nozik, *J. Appl. Phys.*, 2006, **100**, 074510.
- 65 *Dye-sensitized solar cells*, ed. J. Bisquert, F. Fabregat-Santiago and K. Kalyanasundaram, CRC Press, Boca Raton, 2010.
- 66 J. Bisquert, A. Zaban and P. Salvador, *J. Phys. Chem. B*, 2002, **106**, 8774.
- 67 M. A. Green, *Solar Cells: Operating Principles, Technology, and System Applications*, Prentice Hall, New Jersey, 1981.
- 68 J. R. Jennings and Q. Wang, *J. Phys. Chem. C*, 2010, **114**, 1715.
- 69 J. Bisquert, *Phys. Chem. Chem. Phys.*, 2003, **5**, 5360.
- 70 J. Jamnik and J. Maier, *Phys. Chem. Chem. Phys.*, 2001, **3**, 1668.
- 71 J. Bisquert, F. Fabregat-Santiago, I. Mora-Seró, G. Garcia-Belmonte, E. M. Barea and E. Palomares, *Inorg. Chim. Acta*, 2008, **361**, 684.
- 72 J. Bisquert, F. Fabregat-Santiago, I. Mora-Seró, G. Garcia-Belmonte and S. Giménez, *J. Phys. Chem. C*, 2009, **113**, 17278.
- 73 E. M. Barea, M. Shalom, S. Giménez, I. Hod, I. Mora-Seró, A. Zaban and J. Bisquert, *J. Am. Chem. Soc.*, 2010, **132**, 6834.
- 74 P. Salvador, M. González-Hidalgo, A. Zaban and J. Bisquert, *J. Phys. Chem. B*, 2005, **109**, 15915.
- 75 S. M. Sze, *Physics of Semiconductor Devices*, John Wiley and Sons, New York, 1981.
- 76 R. de Gryse, W. P. Gomes, F. Cardon and J. Vennik, *J. Electrochem. Soc.*, 1975, **125**, 711.
- 77 F. Fabregat-Santiago, G. Garcia-Belmonte, J. Bisquert, P. Bogdanoff and A. Zaban, *J. Electrochem. Soc.*, 2002, **150**, E293.
- 78 I. Mora-Seró, F. Fabregat-Santiago, B. Denier, J. Bisquert, R. Tena-Zaera, J. Elias and C. Lévy-Clement, *Appl. Phys. Lett.*, 2006, **89**, 203117.
- 79 R. Tena-Zaera, J. Elias, C. Levy-Clément, C. Bekeny, T. Voss, I. Mora-Seró and J. Bisquert, *J. Phys. Chem. C*, 2008, **112**, 16318.
- 80 G. Hodes, I. D. J. Howell and L. M. Peter, *J. Electrochem. Soc.*, 1992, **139**, 3136.
- 81 S. Södergren, A. Hagfeldt, J. Olsson and S. E. Lindquist, *J. Phys. Chem.*, 1994, **98**, 5552.
- 82 P. R. F. Barnes and B. O'Regan, *J. Phys. Chem. C*, 2010, **114**, 19134.
- 83 P. R. F. Barnes, A. Y. Anderson, J. R. Durrant and B. C. O'Regan, *Phys. Chem. Chem. Phys.*, 2011, **13**, 5798–5816.
- 84 J. Halme, P. Vahermaa, K. Miettunen and P. Lund, *Adv. Mater.*, 2010, **22**, E210.
- 85 A. Gagliardi, S. Mastroianni, D. Gentilini, F. Giordano, A. Reale, T. M. Brown and A. Di Carlo, *IEEE J. Sel. Top. Quantum Electron.*, 2010, **16**, 1611.
- 86 J. Bisquert and V. S. Vikhrenko, *J. Phys. Chem. B*, 2004, **108**, 2313.
- 87 J. Bisquert, *Phys. Rev. B: Condens. Matter Mater. Phys.*, 2008, **77**, 235203.
- 88 J. Bisquert, *Phys. Chem. Chem. Phys.*, 2008, **10**, 3175.
- 89 J. Bisquert and V. S. Vikhrenko, *Electrochim. Acta*, 2002, **47**, 3977.
- 90 A. Pitarch, G. Garcia-Belmonte, I. Mora-Seró and J. Bisquert, *Phys. Chem. Chem. Phys.*, 2004, **6**, 2983.
- 91 J. Bisquert, M. Grätzel, Q. Wang and F. Fabregat-Santiago, *J. Phys. Chem. B*, 2006, **110**, 11284.
- 92 P. R. F. Barnes, A. Y. Anderson, M. Juozapavicius, L. Liu, X. Li, E. Palomares, A. Forneli and B. C. O'Regan, *Phys. Chem. Chem. Phys.*, 2011, **13**, 3547.
- 93 J. Bisquert, G. Garcia-Belmonte, F. Fabregat-Santiago, N. S. Ferriols, P. Bogdanoff and E. C. Pereira, *J. Phys. Chem. B*, 2000, **104**, 2287.
- 94 J. Bisquert, A. Zaban, M. Greenshtein and I. Mora-Seró, *J. Am. Chem. Soc.*, 2004, **126**, 13550.
- 95 J. Bisquert, *J. Phys. Chem. B*, 2004, **108**, 2323.
- 96 A. Hauch and A. Georg, *Electrochim. Acta*, 2001, **46**, 3457.
- 97 F. Fabregat-Santiago, J. Bisquert, E. Palomares, L. Otero, D. Kuang, S. M. Zakeeruddin and M. Grätzel, *J. Phys. Chem. C*, 2007, **111**, 6550.
- 98 E. M. Barea, R. Caballero, F. Fabregat-Santiago, P. de la Cruz, F. Langa and J. Bisquert, *ChemPhysChem*, 2009, **11**, 245.
- 99 I. Mora-Seró and J. Bisquert, *Nano Lett.*, 2003, **3**, 945.
- 100 I. Mora-Seró, S. Giménez, F. Fabregat-Santiago, R. Gomez, Q. Shen, T. Toyoda and J. Bisquert, *Acc. Chem. Res.*, 2009, **42**, 1848.
- 101 J. Bisquert, *J. Electroanal. Chem.*, 2010, **646**, 43.
- 102 M. Grätzel, *Inorg. Chem.*, 2005, **44**, 6841.
- 103 F. Fabregat-Santiago, E. M. Barea, J. Bisquert, G. K. Mor, K. Shankar and C. A. Grimes, *J. Am. Chem. Soc.*, 2008, **130**, 11312.
- 104 Y. Cao, Y. Bai, Q. Yu, Y. Cheng, S. Liu, D. Shui, F. Gao and P. Wang, *J. Phys. Chem. C*, 2009, **113**, 6290.
- 105 S. Kim, J. K. Lee, S. O. Kang, J. Ko, J. H. Yum, S. Fantacci, F. De Angelis, D. Di Censo, M. K. Nazeeruddin and M. Grätzel, *J. Am. Chem. Soc.*, 2006, **128**, 16701.
- 106 W. X. M. Liang, F. Cai, P. Chen, B. Peng, J. Chen and Z. Li, *J. Phys. Chem. C*, 2007, **111**, 4465.
- 107 T. M. D. P. Hagberg, K. M. Karlsson, K. Nonomura, P. Qin, G. Boschloo, T. Brinck, A. Hagfeldt and L. Sun, *J. Org. Chem.*, 2007, **72**, 9550.
- 108 B. A. Gregg, F. Pichot, S. Ferrere and C. L. Fields, *J. Phys. Chem. B*, 2001, **105**, 1422.
- 109 P. J. Cameron and L. M. Peter, *J. Phys. Chem. B*, 2005, **109**, 7392.
- 110 M. J. de Vries, M. J. Pellin and J. T. Hupp, *Langmuir*, 2010, **26**, 9082.
- 111 I. Mora-Seró, J. Bisquert, F. Fabregat-Santiago, G. Garcia-Belmonte, G. Zoppi, K. Durose, Y. Y. Proskuryakov, I. Oja, A. Belaidi, T. Dittrich, R. Tena-Zaera, A. Katty, C. Lévy-Clement, V. Barrio and S. J. C. Irvine, *Nano Lett.*, 2006, **6**, 640.
- 112 T. C. Li, M. S. Góes, F. Fabregat-Santiago, J. Bisquert, P. R. Bueno, C. Prasititchaia, J. T. Hupp and T. J. Marks, *J. Phys. Chem. C*, 2009, **113**, 18385.
- 113 J. Bisquert, *Phys. Chem. Chem. Phys.*, 2011, **13**, 4679.
- 114 U. B. Cappel, A. L. Smeigh, S. Plogmaker, E. M. J. Johansson, H. Rensmo, L. Hammarström, A. Hagfeldt and G. Boschloo, *J. Phys. Chem. C*, 2011, **115**, 4345–4358.
- 115 S. Ardo and G. J. Meyer, *Chem. Soc. Rev.*, 2009, **38**, 115.
- 116 W. B. Heuer, H.-L. Xia, M. Abrahamsson, Z. Zhou, S. Ardo, A. N. A. Sarjeant and G. J. Meyer, *Inorg. Chem.*, 2010, **49**, 7726.
- 117 D. Achey, S. Ardo, H.-L. Xia, M. A. Siegler and G. J. Meyer, *J. Phys. Chem. Lett.*, 2010, **2**, 305.
- 118 J. H. Park, B.-W. Kim and J. H. Moon, *Electrochem. Solid-State Lett.*, 2008, **11**(10), B171.
- 119 S. Uchida, T. Inoue, T. Kubo and H. Segawa, *4th International Conference on the Industrialization of Dye Solar Cells (4th DSC-IC)*, Colorado Springs, USA, 2010.
- 120 J. E. Kroze, N. Hirata, L. Schmidt-Mende, C. Orizu, S. Ogier, K. Carr, M. Grätzel and J. R. Durrant, *Adv. Funct. Mater.*, 2006, **16**, 1832.
- 121 G. Kron, T. Egerter, J. H. Werner and W. Rau, *J. Phys. Chem. B*, 2003, **107**, 3556.
- 122 H. J. Snaith, A. J. Moule, C. Klein, K. Meerholz, R. H. Friend and M. Grätzel, *Nano Lett.*, 2007, **7**, 3372.
- 123 M. Spath, P. M. Sommeling, J. A. M. Von Roosmalen, H. J. P. Smit, N. P. G. Burg, D. R. Mahieu, N. J. Bakker and J. M. Kroon, *Progr. Photovolt.: Res. Appl.*, 2003, **11**, 207.
- 124 W. Liu, L. Hu, S. Dai, L. Guo, N. Jiang and D. Kou, *Electrochim. Acta*, 2010, **55**, 2338.
- 125 T. Miyasaka and M. Ikegami, *J. Photopolym. Sci. Technol.*, 2010, **23**, 269.
- 126 F. A. Castro, P. Chabrecek, R. Hany and F. Nuesch, *Phys. Status Solidi RRL*, 2009, **3**, 278.
- 127 S. Ito, N. L. Cevey-Ha, G. Rothenberger, P. Liska, P. Comte, S. M. Zakeeruddin, P. Péchy, M. K. Nazeeruddin and M. Grätzel, *Chem. Commun.*, 2006, 4004.
- 128 K. Miettunen, X. L. Ruan, T. Saukkonen, J. Halme, M. Toivola, G. S. Huang and P. Lund, *J. Electrochem. Soc.*, 2010, **157**, B814.
- 129 T. N. Murakami and M. Grätzel, *Inorg. Chim. Acta*, 2008, **361**, 572.
- 130 P. Joshi, L. Zhang, Q. Chen, D. Galipeau, H. Fong and Q. Qiao, *ACS Appl. Mater. Interfaces*, 2010, **2**, 3572.
- 131 A. Hinsch, S. Behrens, M. Berginc, H. Bönnemann, H. Brandt, A. Drewitz, F. Einsele, D. Faßler, D. Gerhard, H. Gores, R. Haag, T. Herzog, S. Himmler, G. Khelashvili, D. Koch, G. Nazmutdinova, U. Opara-Krasovec, P. Putyra, U. Rau, R. Sastrawan, T. Schauer, C. Schreiner, S. Sensfuss, C. Siegers, K. Skupien, P. Wachter, J. Walter, P. Wasserscheid, U. Würfel and M. Zistler, *Progr. Photovolt.: Res. Appl.*, 2008, **16**, 489.
- 132 Y. Saito, W. Kubo, T. Kitamura, Y. Wada and S. Yanagida, *J. Photochem. Photobiol. A*, 2004, **164**, 153.

- 133 P. D. Angelo and R. R. Farnood, *J. Adhes. Sci. Technol.*, 2010, **24**, 643.
- 134 M. Toivola, J. Halme, K. Miettunen, K. Aitola and P. D. Lund, *Int. J. Energy Res.*, 2009, **33**, 1145.
- 135 M. Ikegami, K. Miyoshi, T. Miyasaka, K. Teshima, T. C. Wei, C. C. Wan and Y. Y. Wang, *Appl. Phys. Lett.*, 2007, **90**, 153122.
- 136 T. Miyasaka, *J. Phys. Chem. Lett.*, 2011, **2**, 262–269.
- 137 H. J. Snaith and L. Schmidt-Mende, *Adv. Mater.*, 2007, **19**, 3187.
- 138 K. Shankar, G. K. Mor, H. E. Prakasam, S. Yoriya, M. Paulose, O. K. Varghese and C. A. Grimes, *Nanotechnology*, 2007, **18**, 065707.
- 139 N. Kopidakis, K. D. Benkstein, J. van de Lagemaat and A. J. Frank, *J. Phys. Chem. B*, 2003, **107**, 11307.
- 140 B. H. Meekins and P. V. Kamat, *ACS Nano*, 2009, **3**, 3437.
- 141 J. Bisquert, G. Garcia-Belmonte and F. Fabregat Santiago, *J. Solid State Electrochem.*, 1999, **3**, 337.
- 142 A. B. F. Martinson, M. S. Góes, F. Fabregat-Santiago, J. Bisquert, M. J. Pellin and J. T. Hupp, *J. Phys. Chem. A*, 2009, **113**, 4015.
- 143 C. He, Z. Zheng, H. Tang, L. Zhao and F. Lu, *J. Phys. Chem. C*, 2009, **113**, 10322.
- 144 T. Dittrich, A. Belaïdi and A. Ennaoui, *Sol. Energy Mater. Sol. Cells*, 2011, DOI: 10.1016/j.solmat.2010.12.034.
- 145 W. Yu, L. H. Qu, W. Z. Guo and X. G. Peng, *Chem. Mater.*, 2003, **15**, 2854.
- 146 J. A. Chang, J. H. Rhee, S. H. Im, Y. H. Lee, H.-J. Kim, S. I. Seok, M. K. Nazeeruddin and M. Grätzel, *Nano Lett.*, 2010, **10**, 2609.
- 147 M. Shalom, S. Dor, S. Rühle, L. Grinis and A. Zaban, *J. Phys. Chem. C*, 2009, **113**, 3895.
- 148 H. J. Lee, P. Chen, S.-J. Moon, F. Sauvage, K. Sivula, T. Bessho, D. R. Gamelin, P. Comte, S. M. Zakeeruddin, S. I. Seok, M. Grätzel and M. K. Nazeeruddin, *Langmuir*, 2009, **25**, 7602.
- 149 S. Giménez, I. Mora-Seró, L. Macor, N. Guijarro, T. Lana-Villarreal, R. Gómez, L. J. Diguna, Q. Shen, T. Toyoda and J. Bisquert, *Nanotechnology*, 2009, **20**, 295204.
- 150 G. Hodes, J. Manassen and D. Cahen, *J. Electrochem. Soc.*, 1980, **127**, 544.
- 151 V. Chakrapani, K. Tvrđy and P. V. Kamat, *J. Am. Chem. Soc.*, 2010, **132**, 1228.
- 152 I. Robel, M. Kuno and P. V. Kamat, *J. Am. Chem. Soc.*, 2007, **129**, 4136.
- 153 G. Boschloo and D. Fitzmaurice, *J. Phys. Chem. B*, 1999, **103**, 2228.
- 154 T. Berger, T. Lana-Villarreal, D. Monllor-Satoca and R. Gómez, *J. Phys. Chem. C*, 2007, **111**, 9936.
- 155 J. Peet, J. Y. Kim, N. E. Coates, W. L. Ma, D. Moses, A. J. Heeger and G. C. Bazan, *Nat. Mater.*, 2007, **6**, 497.
- 156 S. H. Park, A. Roy, S. Beaupré, S. Cho, N. Coates, J. S. Moon, D. Moses, M. Leclerc, K. Lee and A. J. Heeger, *Nat. Photonics*, 2009, **3**, 297.
- 157 H.-Y. Chen, J. Hou, S. Zhang, Y. Liang, G. Yang, Y. Yang, L. Yu, Y. Wu and G. Li, *Nat. Photonics*, 2009, **3**, 649.
- 158 V. D. Mihailescu, L. J. A. Koster, J. C. Hummelen and P. W. M. Blom, *Phys. Rev. Lett.*, 2004, **93**, 216601.
- 159 R. A. Marsh, J. M. Hodgkiss and R. H. Friend, *Adv. Mater.*, 2010, **22**, 3672.
- 160 V. D. Mihailescu, J. Wildeman and P. W. M. Blom, *Phys. Rev. Lett.*, 2005, **94**, 126602.
- 161 M. S. A. Abdou, F. P. Orfino, Y. Son and S. Holdcroft, *J. Am. Chem. Soc.*, 1997, **119**, 4518.
- 162 S. Hoshino, M. Yoshida, S. Uemura, T. Kodzasa, N. Takada, T. Kamata and K. Yase, *J. Appl. Phys.*, 2004, **95**, 5088.
- 163 Z. Liang, A. Nardes, D. Wang, J. J. Berry and B. A. Gregg, *Chem. Mater.*, 2009, **21**, 4914.
- 164 I. Mora-Seró, Y. Luo, G. Garcia-Belmonte, J. Bisquert, D. Muñoz, C. Voz, J. Puigdolers and R. Alcubilla, *Sol. Energy Mater. Sol. Cells*, 2008, **92**, 505.
- 165 J. Bisquert, G. Garcia-Belmonte, A. Munar, M. Sessolo, A. Soriano and H. J. Bolink, *Chem. Phys. Lett.*, 2008, **465**, 57.
- 166 P. P. Boix, G. Garcia-Belmonte, U. Muñecas, M. Neophytou, C. Waldauf and R. Pacios, *Appl. Phys. Lett.*, 2009, **95**, 233302.
- 167 L. C. Kimerling, *J. Appl. Phys.*, 1974, **45**, 1839.
- 168 I. Balberg, *J. Appl. Phys.*, 1985, **58**, 2603.
- 169 S. S. Hegedus and W. N. Shafarman, *Progr. Photovolt.: Res. Appl.*, 2004, **12**, 155.
- 170 T. Walter, R. Herberholz, C. Müller and H. W. Schock, *J. Appl. Phys.*, 1996, **80**, 4411.
- 171 G. Garcia-Belmonte, P. P. Boix, J. Bisquert, M. Sessolo and H. J. Bolink, *Sol. Energy Mater. Sol. Cells*, 2010, **94**, 366.
- 172 G. Garcia-Belmonte and J. Bisquert, *Appl. Phys. Lett.*, 2010, **96**, 113301.
- 173 M. Grätzel, 2009, presented at MRS Fall Meeting in Boston.
- 174 R. Y. Ogura, S. Nakane, M. Morooka, M. Orihashi, Y. Suzuki and K. Noda, *Appl. Phys. Lett.*, 2009, **94**, 073308.
- 175 M. A. Green, K. Emery, Y. Hishikawa and W. Warta, *Progr. Photovolt.: Res. Appl.*, 2003, **17**, 320.
- 176 J. Y. Kim, K. Lee, N. Coates, D. Moses, T.-Q. Nguyen, M. Dante and A. J. Heeger, *Science*, 2007, **317**, 222.
- 177 C. Wang, M. Shim and P. Guyot-Sionnest, *Science*, 2001, **291**, 2390.

## Supporting information

# Characterization of nanostructured hybrid and organic solar cells by impedance spectroscopy

Francisco Fabregat-Santiago, Germà Garcia-Belmonte, Iván Mora-Seró and Juan Bisquert\*

Photovoltaics and Optoelectronic Devices Group, Departament de Física, Universitat Jaume I, 12071 Castelló, Spain

(\*)[bisquert@fca.uji.es](mailto:bisquert@fca.uji.es)

### Impedance data fits:

| Parameter                          | Ionic liquid cell<br>at 0.4V |           | Ionic liquid cell<br>at $V_{OC}$ (=0.65V) |           | Defective cell<br>at 0.45V |           |
|------------------------------------|------------------------------|-----------|---|-----------|----------------------------|-----------|
|                                    | value                        | Error (%) | value                                     | Error (%) | value                      | Error (%) |
| $R_S (\Omega)$                     | 17.6                         | 0.7       | 16.5                                      | 0.4       | 52.3                       | 0.2       |
| $C_{BL} (F)$                       | $3.30 \cdot 10^{-6}$         | 4.7       | --  | --        | --                         | --        |
| $R_{tr} = r_t L (\Omega)$          | 66.3                         | 3.2       | --  | --        | 51.2                       | 4.6       |
| $R_{rec} = r_{rec}/L (\Omega)$     | 561                          | 0.8       | 22.6                                      | 0.1       | 22.8                       | 2.7       |
| $Q_\mu (F s^{n-1})$                | $3.52 \cdot 10^{-5}$         | 2.8       | $2.67 \cdot 10^{-4}$                      | 2.7       | $4.09 \cdot 10^{-5}$       | 5.2       |
| n                                  | 0.93                         | 0.6       | 0.95                                      | 0.5       | 0.98                       | 0.7       |
| $C_\mu (\text{eq.}) = c_\mu L (F)$ | $2.56 \cdot 10^{-5}$         | 0.8       | $2.03 \cdot 10^{-4}$                      | 0.6       | $3.55 \cdot 10^{-5}$       | 1.2       |
| $R_{Pt} (\Omega)$                  | --                           | --        | 3.8                                       | 2.8       | --                         | --        |
| $Q_{Pt} (F s^{n-1})$               | --                           | --        | $3.6 \cdot 10^{-5}$                       | 24.4      | --                         | --        |
| n                                  | --                           | --        | 0.77                                      | 3.0       | --                         | --        |
| $C_{Pt} (\text{eq.}) (F)$          | --                           | --        | $2.5 \cdot 10^{-6}$                       | 11.0      | --                         | --        |
| $R_d (\Omega)$                     | 81.7                         | 9.2       | 5.8                                       | 2.1       | --                         | --        |
| $\omega_d (\text{rad s}^{-1})$     | 0.52                         | 19.8      | 0.59                                      | 5.3       | --                         | --        |

Table S1: Values and errors of the elements used in the fits of illuminated samples shown in Fig. 18. In some cases it is needed the use of constant phase elements instead of ideal capacitances to obtain a good fit of the data. The equivalent capacitances are

calculated according to eq. S1.

To calculate the equivalent capacitance of a CPE we use

$$C(eq) = \frac{(RQ)^{1/n}}{R} \quad (\text{S1})$$

With  $Q$  the CPE prefactor,  $n$  the CPE index and  $R$  the resistor in parallel to the CPE.

### Electron distribution in dark and light at different diffusion lengths

**Fig. SI 1-3:** (a) Carrier distribution by diffusion-recombination of electrons and photogeneration profile in a nanostructured film with  $L = 10 \mu\text{m}$  and diffusion length as indicated, in dark and under incident photon flux  $\phi_0 = 1.45 \times 10^{17} \text{ cm}^{-2} \text{ s}^{-1}$ , at the indicated potentials at the contact. parameters: absorption coefficient  $\alpha_{abs} = 500 \text{ cm}^{-1}$ , diffusion coefficient  $D_0 = 10^{-5} \text{ cm}^2 \text{ s}^{-1}$ ,  $T = 300 \text{ K}$ ,  $E_{F0} = 0 \text{ eV}$ ,  $E_c = 1 \text{ eV}$ ,  $N_c = 10^{20} \text{ cm}^{-3}$ . (b) The Fermi level of electrons and (c) current density-potential for the same model system.

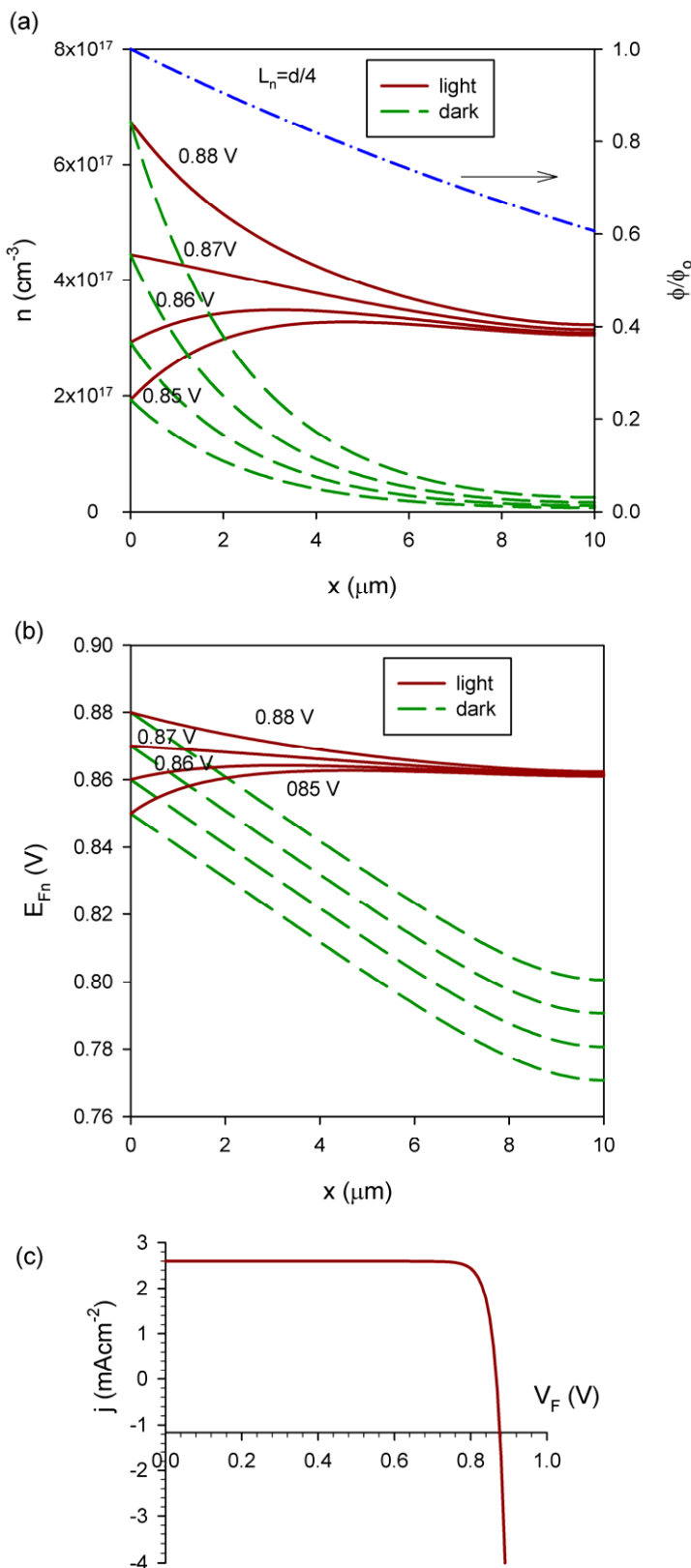


Fig. SI 1

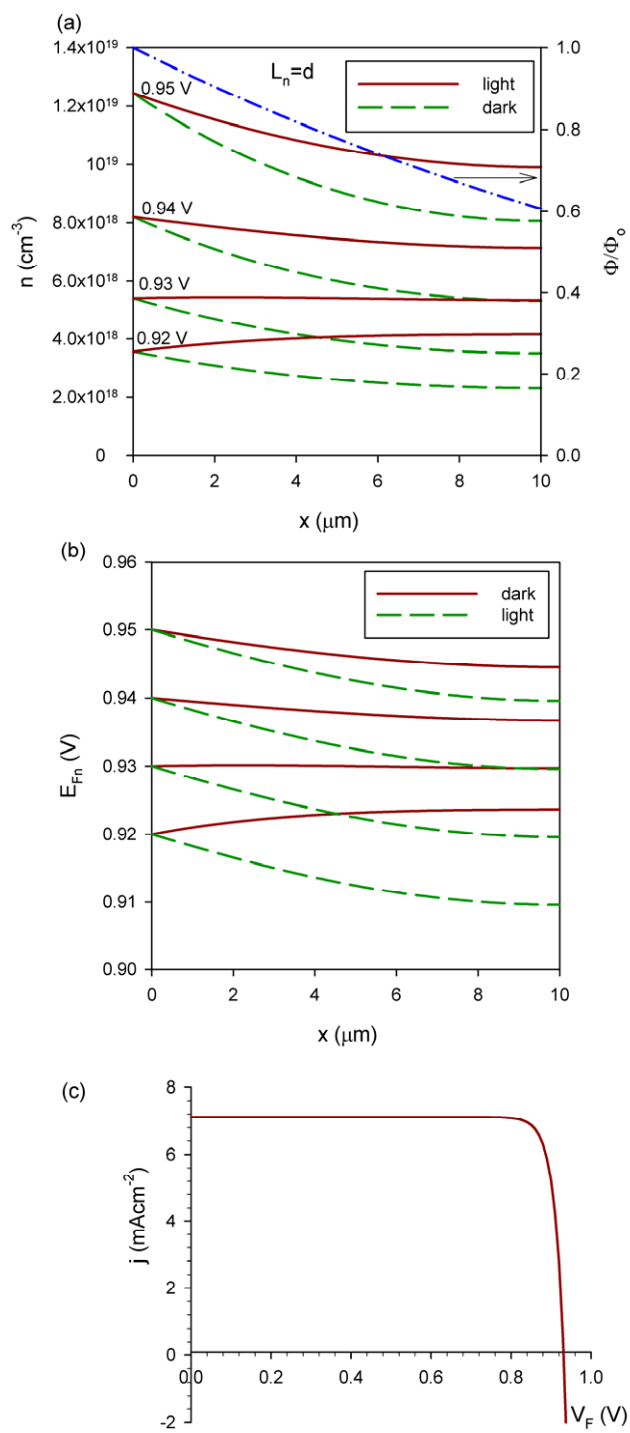
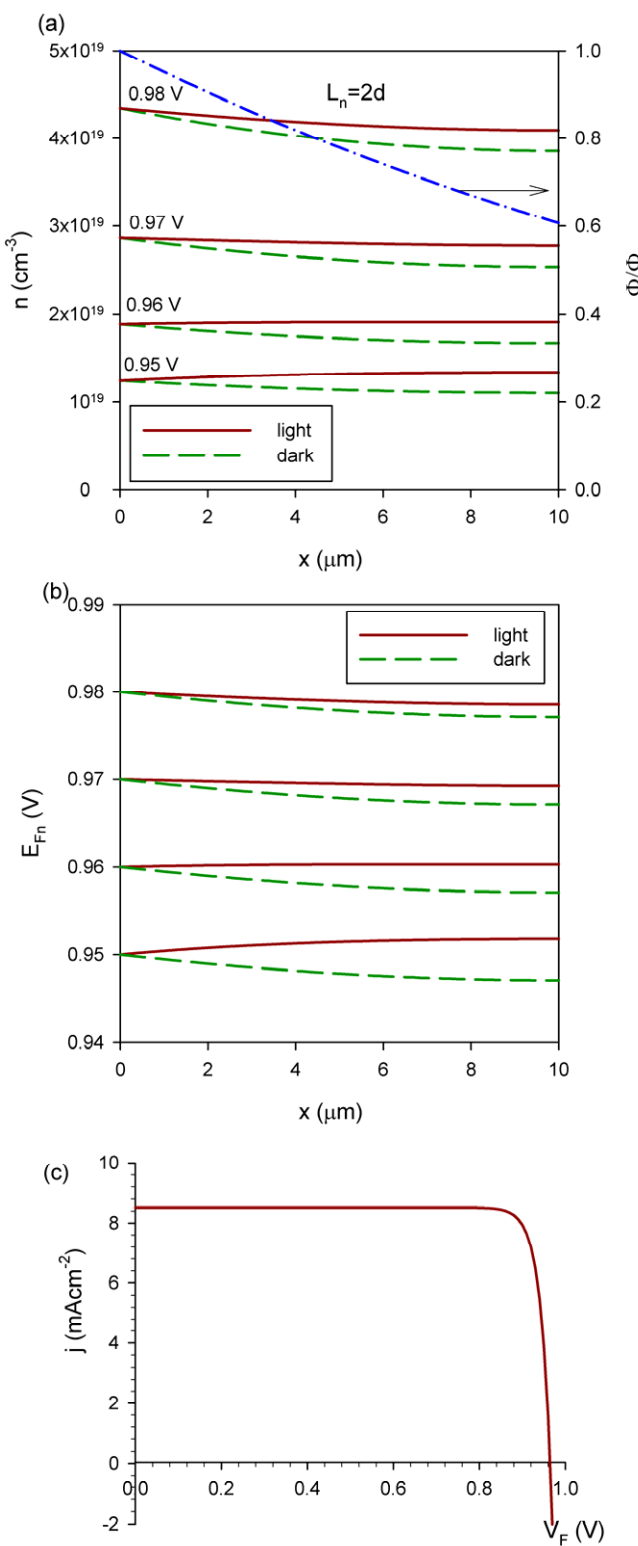


Fig. SI 2



**Fig. SI 3**